

University of Windsor

## Scholarship at UWindor

---

Electronic Theses and Dissertations

Theses, Dissertations, and Major Papers

---

1-1-2010

### An Investigation of Shock Wave Propagation and Attenuation in the Lower Extremity Using Finite Element Analysis.

Alison Schinkel-Ivy  
*University of Windsor*

Follow this and additional works at: <https://scholar.uwindsor.ca/etd>

---

#### Recommended Citation

Schinkel-Ivy, Alison, "An Investigation of Shock Wave Propagation and Attenuation in the Lower Extremity Using Finite Element Analysis." (2010). *Electronic Theses and Dissertations*. 7173.  
<https://scholar.uwindsor.ca/etd/7173>

This online database contains the full-text of PhD dissertations and Masters' theses of University of Windsor students from 1954 forward. These documents are made available for personal study and research purposes only, in accordance with the Canadian Copyright Act and the Creative Commons license—CC BY-NC-ND (Attribution, Non-Commercial, No Derivative Works). Under this license, works must always be attributed to the copyright holder (original author), cannot be used for any commercial purposes, and may not be altered. Any other use would require the permission of the copyright holder. Students may inquire about withdrawing their dissertation and/or thesis from this database. For additional inquiries, please contact the repository administrator via email ([scholarship@uwindsor.ca](mailto:scholarship@uwindsor.ca)) or by telephone at 519-253-3000ext. 3208.

## **NOTE TO USERS**

**This reproduction is the best copy available.**

UMI<sup>®</sup>



An Investigation of Shock Wave Propagation and Attenuation in the Lower Extremity  
Using Finite Element Analysis

by

Alison Schinkel-Ivy

A Thesis  
Submitted to the Faculty of Graduate Studies  
through the Faculty of Human Kinetics  
in Partial Fulfillment of the Requirements for  
the Degree of Master of Human Kinetics at the  
University of Windsor

Windsor, Ontario, Canada  
2010  
© 2010 Alison Schinkel-Ivy



Library and Archives  
Canada

Published Heritage  
Branch

395 Wellington Street  
Ottawa ON K1A 0N4  
Canada

Bibliothèque et  
Archives Canada

Direction du  
Patrimoine de l'édition

395, rue Wellington  
Ottawa ON K1A 0N4  
Canada

*Your file* *Votre référence*  
ISBN: 978-0-494-70588-9  
*Our file* *Notre référence*  
ISBN: 978-0-494-70588-9

#### NOTICE:

The author has granted a non-exclusive license allowing Library and Archives Canada to reproduce, publish, archive, preserve, conserve, communicate to the public by telecommunication or on the Internet, loan, distribute and sell theses worldwide, for commercial or non-commercial purposes, in microform, paper, electronic and/or any other formats.

The author retains copyright ownership and moral rights in this thesis. Neither the thesis nor substantial extracts from it may be printed or otherwise reproduced without the author's permission.

---

In compliance with the Canadian Privacy Act some supporting forms may have been removed from this thesis.

While these forms may be included in the document page count, their removal does not represent any loss of content from the thesis.

#### AVIS:

L'auteur a accordé une licence non exclusive permettant à la Bibliothèque et Archives Canada de reproduire, publier, archiver, sauvegarder, conserver, transmettre au public par télécommunication ou par l'Internet, prêter, distribuer et vendre des thèses partout dans le monde, à des fins commerciales ou autres, sur support microforme, papier, électronique et/ou autres formats.

L'auteur conserve la propriété du droit d'auteur et des droits moraux qui protègent cette thèse. Ni la thèse ni des extraits substantiels de celle-ci ne doivent être imprimés ou autrement reproduits sans son autorisation.

---

Conformément à la loi canadienne sur la protection de la vie privée, quelques formulaires secondaires ont été enlevés de cette thèse.

Bien que ces formulaires aient inclus dans la pagination, il n'y aura aucun contenu manquant.

  
**Canada**

### *Author's Declaration of Originality*

I hereby certify that I am the sole author of this thesis and that no part of this thesis has been published or submitted for publication.

I certify that, to the best of my knowledge, my thesis does not infringe upon anyone's copyright nor violate any proprietary rights and that any ideas, techniques, quotations, or any other material from the work of other people included in my thesis, published or otherwise, are fully acknowledged in accordance with the standard referencing practices. Furthermore, to the extent that I have included copyrighted material that surpasses the bounds of fair dealing within the meaning of the Canada Copyright Act, I certify that I have obtained a written permission from the copyright owner(s) to include such material(s) in my thesis and have included copies of such copyright clearances to my appendix.

I declare that this is a true copy of my thesis, including any final revisions, as approved by my thesis committee and the Graduate Studies office, and that this thesis has not been submitted for a higher degree to any other University or Institution.

### *Abstract*

Although shock wave propagation through the body following impact in humans has been researched extensively, shock attenuation along the length of the lower extremity has not been investigated. The purposes of this study were to: validate a human finite element model (THUMS) for simulated running-type impacts; and evaluate shock wave propagation along the lower extremity. Force and acceleration data from experimental human pendulum impacts and simulated impacts using THUMS agreed relatively well (22% and 54% relative error for force and acceleration, respectively). Accelerations along the tibia indicated that the model exhibited shock wave propagation along the lower extremity, and that the wave was attenuated as it moved proximally along the tibia and across the knee. Although further work may be necessary to improve the timing of forces and accelerations, the model represented, to a certain extent, the shock wave propagation and attenuation patterns that occur in live humans.

## *Acknowledgements*

There are a number of individuals who deserve acknowledgement for the various ways in which they have contributed to this project. Thanks to NSERC for funding this project, and to Don Clarke for his technical expertise and his help with data processing. To the members of my thesis committee, Dr. William Altenhof and Dr. Nadia Azar, thank you for your valuable contributions to this project, as well as the time, guidance, and support that you have provided throughout this process. To my advisor, Dr. David Andrews, thanks for your guidance over the last three years, and for the many opportunities that you have provided me with to hone my skills and prepare for my future academic endeavours.

To Mike, Mike (a.k.a. Mangelidis), and Tim (a.k.a. Mom) ... coming in to school every day was much easier knowing that I was going to be working with 'the three best friends that anybody could have' (Galifianakis, 2009). Thanks for all of the fun, hilarity, and adventures over the last two years.

To my parents, John and Vicky, for your never-ending love and support, and willingness to lend an ear whenever I needed it. And finally, to my husband, Ryan ... you have helped me to become the person I am today. None of this would have been possible without you. Thank you for your constant encouragement and for always helping me strive to do my best.

## *Table of Contents*

Author's Declaration of Originality .....	iii
Abstract .....	iv
Acknowledgements .....	v
List of Tables .....	vii
List of Figures .....	viii
Glossary .....	xi
1. Introduction.....	1
1.1 Research Questions.....	4
1.2 Hypotheses.....	4
2. Literature Review.....	6
2.1 Anatomy of the Lower Extremity.....	6
2.2 Tissue Properties.....	9
2.3 Impact Forces .....	17
2.4 Shock Transmission and Attenuation .....	24
2.5 Biomechanical Modelling.....	38
2.6 Finite Element Analysis.....	40
2.7 Literature Review Summary.....	52
3. Methods.....	53
3.1 Objective #1 .....	53
3.2 Objective #2.....	81
4. Results.....	85
4.1 Objective #1 .....	85
4.2 Objective #2.....	99
5. Discussion .....	104
5.1 Objective #1 .....	104
5.2 Objective #2.....	123
5.3 Hypotheses Revisited .....	128
6. Limitations and Future Directions .....	130
7. Conclusion .....	137
Appendix A.....	138
Appendix B .....	142
Appendix C .....	145
Appendix D.....	147
References.....	148
Vita Auctoris.....	161

*List of Tables*

Table 1. Characteristics of the heel pad during walking and running.....15

Table 2. Comparison of in vivo and in vitro heel pad properties.....16

Table 3. Examples of studies using simplified and complex material properties .....45

Table 4. Structural details of the AM-50 pedestrian THUMS model .....49

Table 5. Modifications for each version of the full body impact model.....70

Table 6. Means and standard deviations for all experimentally measured variables .....89

Table 7. Peak global kinetic, internal, and total energy for each version of the model.....90

Table 8. Major sources of hourglass energy for each version of the model .....92

Table 9. Major sources of sliding interface energy for each version of the model .....93

Table 10. Changes in joint angles following impact for each version of the model .....94

Table 11. Impact force and tibial acceleration variables for each version of the model.....95

Table 12. Relative error comparisons between the experimental and model data for impact force and tibial acceleration variables .....98

Table 13. Validation metric values and relative errors for force- and acceleration-time histories .....99

Table 14. Peak accelerations and times to peak acceleration for all ankle, tibial, and femoral nodes for each version of the model .....100

Table 15. Shock attenuation between nodes along the lower extremity .....103

Table 16. Previous findings for dependent force and acceleration variables.....107

Table 17. Reported values of shock attenuation between the tibia and the head.....128

**List of Figures**

Figure 1. The bones of the right lower extremity. ....7

Figure 2. Musculature of the right lower extremity, a) anterior view; b) lateral view; c) posterior view.....8

Figure 3. Typical non-linear stress-strain curve for biological tissues.....9

Figure 4. a) Creep in response to constant load.  
b) Stress relaxation in response to constant deformation.  
c) Hysteresis during a loading-unloading cycle .....11

Figure 5. Mean ground reaction force profile resulting from 5 participants running at 4.5 m/s across a force plate .....20

Figure 6. Acceleration profiles for the head and distal tibia, during running at 3.8 m/s.....25

Figure 7. a) Displacement of a forearm marker following impact.  
b) Acceleration at the proximal tibia following impact .....26

Figure 8. The accelerations occurring in rigid and soft tissues following impact.....27

Figure 9. Average power spectral densities for 14 subjects at four times throughout a 30 minute run .....28

Figure 10. Wobbling mass model.....29

Figure 11. A comparison of vertical ground reaction forces for an experimental trial and wobbling mass and rigid mass model simulations.....30

Figure 12. a) The AM-50 occupant THUMS model.  
b) The AM-50 pedestrian THUMS model .....47

Figure 13. The lower extremity of the THUMS model.....48

Figure 14. Flow chart diagramming the methodology that was followed to address Objectives #1 and #2.....55

Figure 15. The left shoe used in the shoe crush simulations, with the infinite rigid wall and rigid body defined just superior and inferior, respectively, to the shoe.....57

Figure 16. Movement of the rigid body inferior to the shoe, as prescribed by the displacement loading curve.....58

Figure 17. Modifications to the THUMS model .....60

Figure 18. The human pendulum, impact apparatus, and participant positioning.....	62
Figure 19. Schematic diagram of a force waveform from a human pendulum impact.....	63
Figure 20. Participant’s leg instrumented with electrodes, an accelerometer, and an electrogoniometer.....	64
Figure 21. Schematic diagram of a typical acceleration waveform from a human pendulum impact.....	65
Figure 22. Schematic showing the set up of the heel pad friction protocol .....	68
Figure 23. Sample graph of vertical and A-P forces from a friction trial.....	68
Figure 24. Change in ankle angle in the sagittal plane over the course of a simulation, indicating how the maximum and net changes in angle were determined.....	74
Figure 25. Location at which acceleration data were collected on the model.....	75
Figure 26. Local coordinate system defined for the tibia .....	76
Figure 27. A comparison of the force profiles from a simulation and 10 experimental trials.....	77
Figure 28. Example of the superimposed experimental and model impact force profiles with a phase shift in the model profile.....	79
Figure 29. The validation metric (V) as a function of the relative error .....	81
Figure 30. Local coordinate system defined for the femur.....	81
Figure 31. Selected nodes for acceleration measurements along the tibia and femur.....	83
Figure 32. Stress-strain curve assigned to the original THUMS shoe .....	85
Figure 33. a) Force-displacement curve obtained from the crushing of the original THUMS shoe. b) Force-displacement curve obtained from in vivo human heel pad testing.....	86
Figure 34. Extrapolated stress-strain curve based on Aerts and De Clercq’s (1993) data .....	87
Figure 35. Final shoe crush simulation force-deformation curve, compared to in vivo heel pad data.....	87
Figure 36. Extrapolated stress-strain curve based on Wearing et al.’s (2009) data .....	88

Figure 37. Mean force-time profile for 10 experimental trials.....	89
Figure 38. Mean acceleration-time profile for 10 experimental trials.....	90
Figure 39. Time histories for the global a) kinetic energy; b) internal energy; c) total energy for each version of the model.....	91
Figure 40. Global hourglass energies for each version of the model.....	92
Figure 41. Global sliding interface energies for each version of the model.....	93
Figure 42. Model versus experimental force-time histories for each version of the model.....	96
Figure 43. Model versus experimental acceleration-time histories for each version of the model.....	97
Figure 44. Acceleration-time histories for a) tibial nodes and b) femoral nodes for version 1.....	101
Figure 45. Acceleration-time histories for a) tibial nodes and b) femoral nodes for version 3.....	102
Figure 46. Effects of hysteretic unloading and shape factors on the MAT_057 unloading curve.....	106
Figure 47. Posterior view of the shoe, foot, and ankle at 80 ms for a) version 2; b) version 3.....	110
Figure 48. Schematic representing the ‘heel strike transient’ at the beginning of a typical gait profile.....	116

## *Glossary*

AM-50 (50<sup>th</sup> percentile American male): the original version of the THUMS model, designed to represent a 50<sup>th</sup> percentile American male.

AS (acceleration slope): slope of the acceleration curve between 30% and 70% of the peak acceleration (measured in g/s).

BW (body weight): the measure of the force of gravity acting on the body (measured in N). Impact force measurements are often normalized to an individual's body weight.

Cubic spline: a spline constructed of piecewise third-order polynomials, often used for data interpolation.

FEA (finite element analysis): a computational technique used to obtain an approximate solution to the equation,  $\{F\} = [m] \cdot \{\ddot{x}\} + [c] \cdot \{\dot{x}\} + [k] \cdot \{x\}$ , where  $F$  = force;  $m$  = mass;  $\ddot{x}$  = acceleration;  $c$  = damping constant;  $\dot{x}$  = velocity;  $k$  = stiffness constant;  $x$  = displacement.

FEM (finite element model): a discretized representation of a system to which FEA may be applied.

GRF (ground reaction force): a force equal in magnitude and opposite in direction to the force that the body exerts on the ground (measured in N).

LR (loading rate): slope of the force curve between 20% and 80% of the peak force (measured in N/s).

LS-DYNA: an advanced general purpose non-linear finite element program.

LS-PREPOST: an advanced pre- and post-processor for LS-DYNA.

PA (peak acceleration): peak acceleration magnitude as measured at the tibial tuberosity following impact (measured in  $m/s^2$ ). PA is typically expressed as a multiple of acceleration due to gravity, or g units.

PF (peak impact force): peak force during the impact phase (measured in N).

RM (rigid mass): the rigid tissues of the body (bone).

SA (shock attenuation): a reduction in shock wave amplitude as it moves proximally through the body's tissues.

Shock: the transient condition that occurs following a sudden change in force application, causing the disruption of a system's equilibrium.

Shock wave: the propagation of a stress or pressure wave through a medium.

**THUMS (Total HUMAN Model for Safety):** a finite element model developed by the Toyota Motor Corporation and the Toyota Central Research and Development Laboratories in conjunction with Wayne State University.

**TPA (time to peak acceleration):** time between impact and the peak acceleration (measured in ms or s).

**TPF (time to peak impact force):** time between impact and the peak force (measured in ms or s).

**WM (wobbling mass):** the non-rigid tissues of the body (lean and fat masses) that are attached to underlying bony structures. Movement of these tissues relative to the bony structures acts to attenuate the shock wave that moves through the body following impact.

## *Chapter 1*

### *Introduction*

In any type of human locomotion, impact forces are experienced at the foot as a result of the collision between the foot and the ground. These collisions occur approximately 1500 times per mile during running (McKeag & Dolan, 1989), or 930 times per kilometre. Each impact subjects the individual to forces of up to 2.8 times their body weight (Cavanagh & Lafortune, 1980); these forces are subsequently transmitted proximally through the tissues of the body as a stress wave, commonly referred to as a 'shock wave' (Derrick et al., 1998; Dufek et al., 2009; Flynn et al., 2004; Hamill et al., 1995; Holmes & Andrews, 2006; Lafortune, 1991; Lafortune et al., 1995, 1996a, b; McMahon et al., 1987; Mercer et al., 2002, 2003a, b; Milner et al., 2006; Verbitsky et al., 1998; Voloshin et al., 1998; Voloshin & Wosk, 1982; Whittle, 1999; Wosk & Voloshin, 1981). As the shock wave propagates through the body, the rigid and soft tissues act to attenuate the signal (Dufek et al., 2009; Hamill et al., 1995). Previous studies using animals have indicated that repetitive loading may lead to cartilage and joint degeneration (Radin et al., 1973; Serink et al., 1977) and bone microdamage (Burr et al., 1985). The results of studies using human participants also imply a relationship between injury and impact forces and the associated shock wave, in that runners with a stress fracture history experience greater impact forces (Grimston et al., 1991), loading rates, and tibial shock (Milner et al., 2006).

Rigid tissues (bone) have been shown to affect the response of the body to impact (Liu & Nigg, 2000; Pain & Challis, 2004). Similarly, it has also been established that soft tissues affect shock attenuation through their capacity to 'wobble', or move relative to the underlying bone (Chu et al., 1986; Hamill et al., 1995; Lafortune et al., 1996a). For

example, in comparisons of rigid body models (representing only bone) and wobbling mass models (representing both rigid and soft tissues), the latter substantially reduced both external and internal loading (Gittoes et al., 2006; Gruber et al., 1998; Liu & Nigg, 2000; Pain & Challis, 2001, 2004, 2006). The roles of individual soft tissues, such as muscle (Derrick et al., 1998; Holmes & Andrews, 2006; Mercer et al., 2003b) and the heel pad (Pain & Challis, 2001) have also been examined. Further, Schinkel-Ivy et al. (2010) investigated the effects of varying tissue masses on the response of the shank to impact. The authors found that the greater masses of lean and bone tissues in males contributed to an increased capacity for shock attenuation compared to that of females.

Although both experimental and numerical modelling techniques have provided evidence that the various tissues of the body contribute to shock attenuation, an attempt has not yet been made to evaluate the propagation of the shock wave along the length of the lower extremity. This will contribute to the current understanding of the behaviours of the tissues in response to impact, aid in the elucidation of the mechanisms of chronic overuse injuries, and ultimately enhance the ability to design interventions to prevent such injuries. However, due to ethical considerations and difficulties in obtaining these types of measurements, in vivo experimentation is not conducive to examining shock wave propagation internal to the human body. As an alternative, wobbling mass models have been used to examine the contributions of rigid and soft tissues following impact. While these types of models provide control over parameters such as segment tissue masses and the stiffness and damping of various structures (Pain & Challis, 2004), and are able to predict whole body kinematics and kinetics resulting from impact loading, this technique does not allow for the estimation of point loading measurements, such as stresses or strains (Mukherjee et al., 2007).

Finite element analysis (FEA) is a computational technique that may provide a means to overcome the aforementioned limitations so that shock propagation and attenuation within the lower extremity can be examined in detail. FEA enables a structure with complex material properties, geometries, and/or loading conditions (Brown, 2004) to be discretized into smaller elements, at which point a solution is obtained for each element, and ultimately for the entire structure (Dawson et al., 1999; Zhang et al., 1998). Variables such as deformations, strains, and stresses may then be examined at any location within the modelled structure (Goh et al., 2005; Limbert et al., 2004; Shen et al., 2008).

The Total Human Model for Safety (THUMS) is a finite element model (Iwamoto et al., 2003, 2007; Maeno & Hasegawa, 2001) that possesses a high degree of biofidelity (Maeno & Hasegawa, 2001), and contains both rigid (bone) and soft (ligaments, tendons, muscles, adipose tissue, and skin) tissues. By incorporating these structures, as well as geometries and material properties similar to those of humans (Yasuki, 2007), the THUMS model enables a realistic simulation of a human's response to an impact. The THUMS model has been validated for a variety of frontal and lateral impacts, simulating those conditions that may be experienced by occupants and pedestrians during automobile impacts (Iwamoto et al., 2003; Maeno & Hasegawa, 2001; Nagasaka et al., 2003; Oshita et al., 2002). However, it has not yet been validated for impacts to the heel and foot, mimicking those experienced during human locomotion. Successful validation of the model is necessary to ensure that the results from an impact simulation may be considered representative of the human response to a running-type impact.

Therefore, the first objective of the study was to validate the THUMS model for running-type impacts administered at the heel, by comparing the force and acceleration outputs from the model to the experimental data from a human pendulum impact. Following validation, the second objective was to assess the propagation and attenuation of the shock wave along the lower extremity, by comparing the magnitude and timing of peak accelerations along the length of the lower extremity.

## **1.1 Research Questions**

### ***1.1.1 Objective #1***

1. Does the THUMS shoe structure, located inferior to the foot bones of the full body model, behave in a similar manner to that of a human heel pad?
2. Are the force (collected from the contact point between the foot of the THUMS model and the rigid wall) and acceleration (collected from a node medial to the tibial tuberosity of the THUMS model) profiles comparable to the data collected experimentally from a human pendulum impact?

### ***1.1.2 Objective #2***

3. How does the shock wave propagate along the tibia and femur?

## **1.2 Hypotheses**

### ***1.2.1 Objective #1***

1. As the pedestrian THUMS model was originally developed to simulate vehicle-pedestrian impacts (Iwamoto et al., 2003, 2007; Maeno & Hasegawa, 2001), it was hypothesized that the shoe structure of the THUMS model will be more representative of a shoe with respect to its material properties and behaviour in response to loading, as opposed to an in vivo human heel pad. Therefore, it is

probable that the material properties of the shoe structure will require modifications to better represent the loading and unloading behaviour of a human heel pad.

2. Due to the high level of biofidelity of the THUMS model, it was hypothesized that the model will represent the response of the lower extremity to a running-type impact to a certain extent. However, some modifications to the model at the interface between the foot and impact surface may be necessary in order to more accurately represent the human tibial response.

### *1.2.2 Objective #2*

3. It was hypothesized that the amplitude of the acceleration will decrease in magnitude with proximal movement along the lower extremity. As the knee joint has been found responsible for shock wave attenuation of approximately 30% in vivo (Wosk & Voloshin, 1981), it was hypothesized that the knee joint of the model will act to attenuate a substantial proportion of the acceleration during the transfer of the shock wave across the knee joint. Additionally, with respect to temporal characteristics, the times at which the peak accelerations occur at each node will be slightly delayed from that of the node immediately before.

## *Chapter 2* *Review of Literature*

### *2.1 Anatomy of the Lower Extremity*

Each body segment consists of various components, including soft tissues (skin, adipose, muscle, and connective tissue such as ligaments and tendons), and rigid tissues (bone). The relative proportions of the rigid and soft tissues vary based on the body segment (Challis & Pain, 2008). Clarys and Marfell-Jones (1986) found that soft tissues (skin, fat, and muscle) constituted 90.3%, 77.65%, and 68.9% of the mass of the thigh, leg, and foot, respectively, while rigid tissue accounted for 9.7%, 22.35%, and 31.1%.

#### *2.1.1 Skeleton*

The skeleton of the lower extremity consists of 30 bones in the thigh, shank, and foot (Figure 1). The femur is the long bone of the thigh, and articulates with the acetabulum of the pelvic girdle proximally, and tibia and patella distally. The patella develops within the quadriceps tendon, and lies anterior to the knee joint. The bones of the shank are the tibia, which is the weight-bearing bone, and the fibula, which is smaller and sits laterally to the tibia. The proximal region of the foot is referred to as the tarsus, and consists of seven tarsal bones. The metatarsus is the intermediate foot region, with five metatarsal bones, while fourteen phalanges comprise the distal region. The bones of the foot are arranged in two non-rigid arches which assist in shock absorption (Tortora, 2005). In normal gait, approximately 60% of the body weight is supported by the heel, while the remaining 40% is supported by the ball of the foot (Tortora, 2005).

#### *2.1.2 Joints*

The hip joint is a ball-and-socket synovial joint between the acetabulum and the head of the femur. A strong articular capsule, associated ligaments and muscles, and the

fit of the femoral head and the acetabulum enable a high level of stability at the hip (Tortora, 2005). The knee consists of three joints at its lateral, medial, and intermediate aspects (lateral and medial tibiofemoral joints and patellofemoral joint, respectively) (Tortora, 2005). Ligaments, menisci, and bursae are contained within the knee to maintain stability and reduce friction. Finally, the ankle is a hinge joint formed by the articulations of the talus with the distal tibia and the medial and lateral malleoli of the tibia and fibula, respectively. The shapes of the articulating bones and the strength of the ligaments and tendons within the ankle contribute to the mobility and stability of the joint. The structure of the ankle joint enables a change from the vertical orientation of the leg bones and soft tissues to the horizontal orientation of the foot structures (Tortora, 2005).

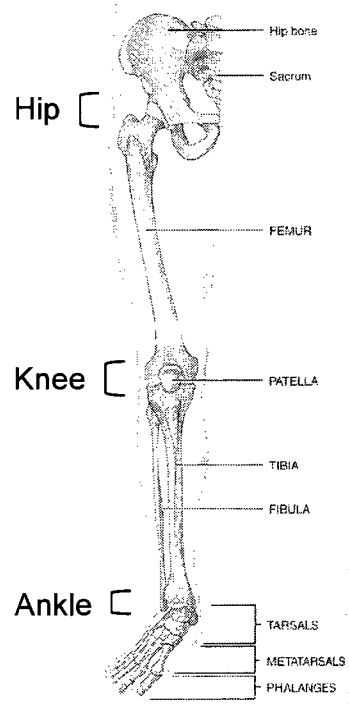


**Figure 1:** The bones of the right lower extremity (anterior view) (Adapted from Tortora, 2005).

### 2.1.3 *Soft Tissues*

The muscles of the thigh and shank can be grouped into three main compartments (Figure 2). The muscles of the thigh can be grouped into the medial compartment, which acts to adduct the hip; the anterior compartment, which acts to flex the hip and extend the knee; and the posterior compartment, which acts to extend the hip and flex the knee. The musculature of the shank can be grouped into the lateral compartment, which plantar flexes and everts the foot; anterior compartment, which dorsiflexes the foot; and posterior compartment, which plantarflexes the foot. Two major tendons within the lower extremity are the patellar tendon, connecting the quadriceps and patella, and the Achilles tendon, connecting the gastrocnemius, soleus, and plantaris muscles to the calcaneus. Major ligaments of the lower extremity include the cruciate (anterior and posterior) and collateral (lateral and medial) ligaments of the knee, and the medial and lateral ligament groups of the ankle.

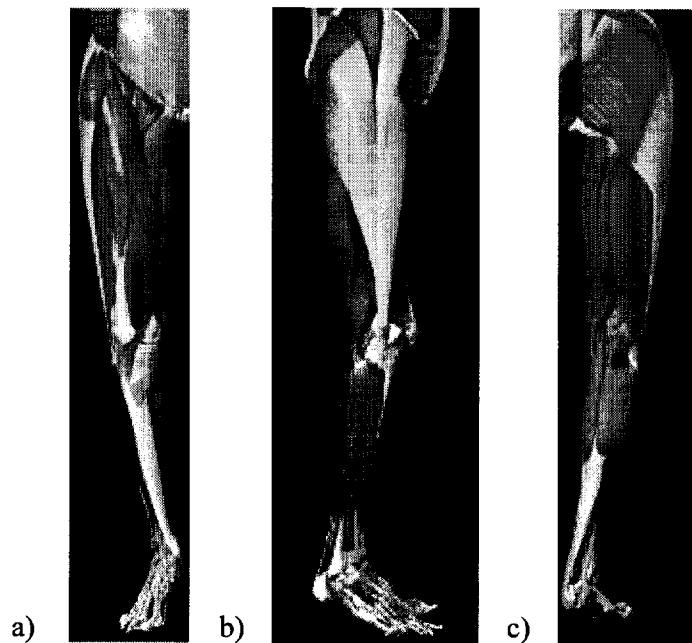


**Figure 2:** Musculature of the right lower extremity, a) anterior view; b) lateral view; c) posterior view (Interactive Functional Anatomy, version 3.21).

## 2.2 Tissue Properties

Each of the tissues within the body, both rigid and soft, may be characterized by a specific set of material properties. These properties may be related to such characteristics as the composition of the tissue, or its response to imposed loading, which may be characterized by variables such as stress and strain. Stress ( $\sigma$ ) is defined as the force per unit area in a structure, while strain ( $\epsilon$ ) represents the deformation of a solid expressed relative to its original length. The relationship between stress and strain for a specific material is represented by its constitutive relation (Lu & Mow, 2008), which describes its response to an applied load (Humphrey, 2002). Most human tissues exhibit a non-linear stress-strain relationship, as these tissues generally contain a large proportion of water (Lu & Mow, 2008). A non-linear response indicates that the stress response of the tissue changes as the imposed strain increases (Figure 3).

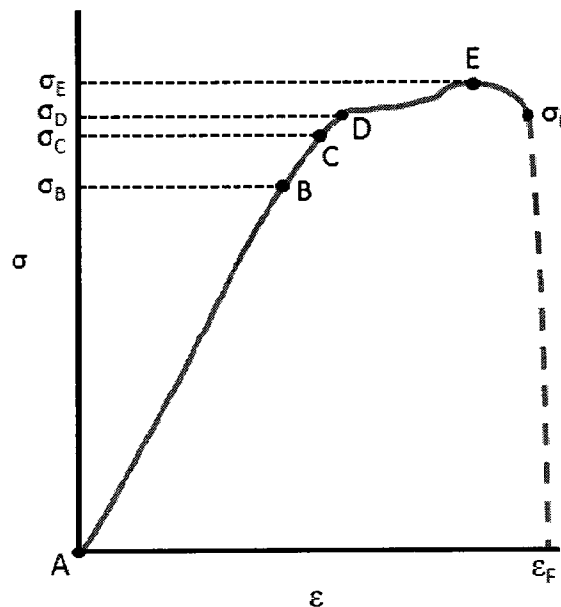


**Figure 3:** Typical non-linear stress ( $\sigma$ )-strain ( $\epsilon$ ) curve for biological tissues. A = initial condition; B = linear limit; C = elastic limit; D = yield point; E = ultimate stress/material strength; F = rupture point (Adapted from Whiting & Zernicke, 2008).

Other properties common to biological tissues include heterogeneity, anisotropy, and viscoelasticity. Heterogeneity indicates that the tissue consists of more than one component, resulting in a varying structure throughout the tissue (Whiting & Zernicke, 2008); an example of a heterogeneous biological tissue would be hyaline cartilage, which is found at the ends of long bones (among other locations), and consists of ground substance, collagen fibres, and chondrocytes (Tortora, 2005). Anisotropy refers to a tissue in which the response to loading varies depending on the direction in which it is loaded (Whiting & Zernicke, 2008). Viscoelasticity refers to those materials that exhibit both elastic and viscous components; because of the latter, the stress response of the tissue is dependent on the strain imposed on the tissue, as well as the rate at which that strain is imposed. Viscoelastic tissues exhibit characteristic behaviours, such as creep, stress relaxation, and hysteresis (Figure 4). Creep describes the response of a viscoelastic tissue subjected to constant load, in which the tissue deforms rapidly under initial loading, then continues to deform slowly while the load is maintained (Whiting & Zernicke, 2008). Stress relaxation occurs as a tissue is subjected to constant deformation; when deformed, the material develops a high initial stress, which decreases as the deformation is maintained (Whiting & Zernicke, 2008). Finally, hysteresis is the property of viscoelastic tissues by which energy is lost as heat during deformation, resulting in a delayed unloading pattern (Whiting & Zernicke, 2008).

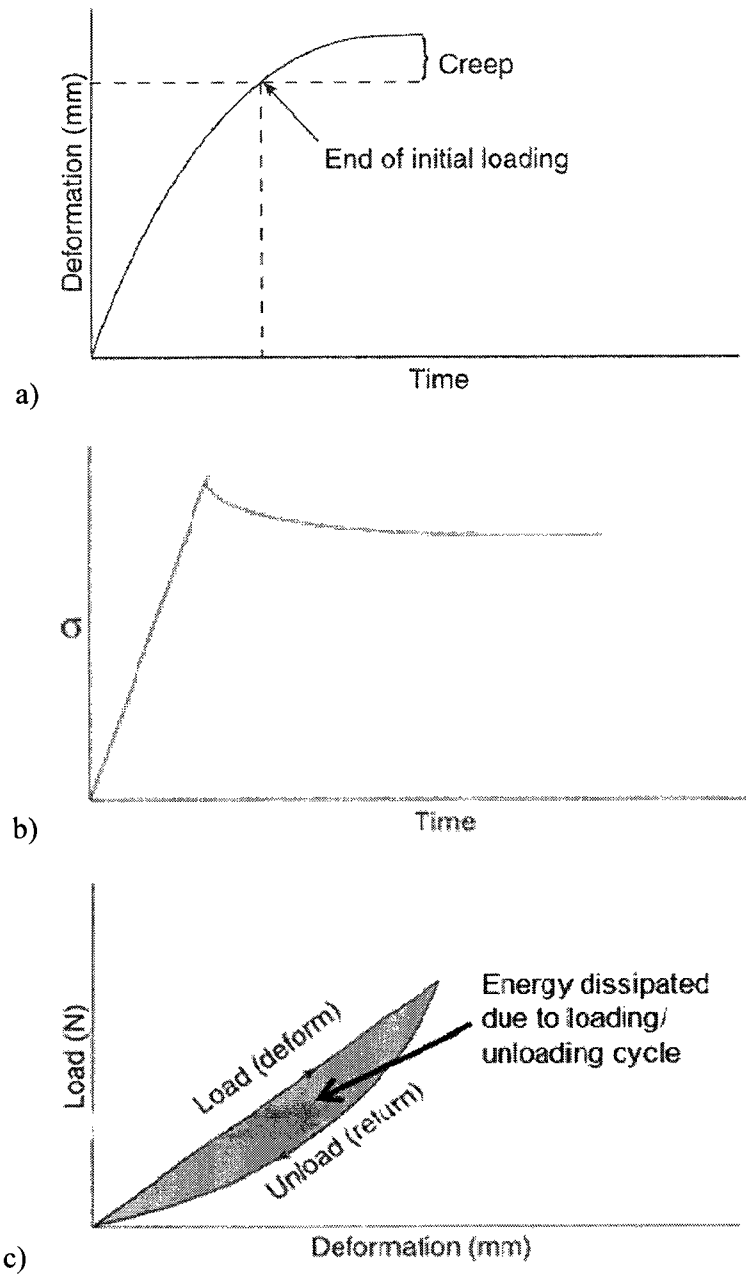


**Figure 4:** a) Creep in response to constant load; b) Stress relaxation in response to constant deformation; c) Hysteresis during a loading-unloading cycle (Adapted from Whiting & Zernicke, 2008).

### 2.2.1 Bone

The long bones of the lower extremity are composed of two major types of bone tissue: cortical and trabecular. Cortical bone constitutes the external layer of all bones,

and it is the main component of the diaphysis in long bones. The osteons in cortical bone align parallel to the bone's principle loading pathway, to resist bending or fracture in compressive loading (Tortora, 2005). Trabecular bone is spongy and porous, constitutes the majority of bone tissue of short, flat, and irregular bones and the epiphyses of long bones, and encircles the medullary cavity of the diaphyses of long bones (Tortora, 2005). Trabecular bone forms a complex network of bone tissue that resembles a sponge-like lattice; the plates and rods forming the network are referred to as trabeculae (Dagan et al., 2004). The skeletal mass of the body consists of approximately 80% cortical and 20% trabecular bone. However, given the structure of the latter, trabecular bone accounts for 80% of bone surface area (Teoh & Chui, 2008). The porosity ranges from 5-30% for cortical and from 30-90% for trabecular bone (Teoh & Chui, 2008). The trabeculae are the dominant load-bearing component of trabecular bone, in that the lattices are aligned parallel to the principle stress pathway when the bone is loaded under normal physiological conditions (Dagan et al., 2004). This enables distribution of load by the epiphysis from the joint surface to the diaphysis (Dagan et al., 2004). Trabecular bone exhibits time dependent behaviour, which results in an increased risk of damage during cyclic loading (Keaveny et al., 2001).

The mechanical properties of bone depend on the individual, anatomical location, bone orientation, biological processes, and time (Helgason et al., 2008), as well as trabecular orientation and microstructure, which may vary based on the location of the applied load (Teoh & Chui, 2008). Bone exhibits anisotropy (Teoh & Chui, 2008), heterogeneity (Keaveny et al., 2001), and viscoelasticity (Dawson et al., 1999). There exists a strong correlation between the distribution of these mechanical properties throughout the bone and the distribution of stress within the bone tissue following impact

(Merz et al., 1996). The overall strength of bone is dependent upon a combination of factors, such as the size, shape, and material properties of the bone (Hernandez & Keaveny, 2006), and bone density (Teoh & Chui, 2008).

### **2.2.2 *Soft Tissues***

‘Soft tissue’ is a relatively general term, encompassing many of the tissues within the body, including skin, adipose tissue, muscles, ligaments, tendons, and articular cartilage. These soft tissues behave according to such basic mechanical concepts as stress and strain (Humphrey, 2002), and are often characterized by irregular geometry and highly complex composition (Zhang et al., 1998). Further, soft tissues are generally associated with complex material properties, such as heterogeneity, anisotropy, viscoelasticity, and non-linearity (Humphrey, 2002; Zhang et al., 1998), and are capable of large deformations (Chawla et al., 2009). Additionally, these mechanical properties can vary across anatomical locations, times, and individuals (Humphrey, 2002).

### **2.2.3 *Muscles***

Skeletal muscle is unique among the biological soft tissues in its ability to actively generate strains independent of externally applied forces or velocities up to a certain level of activation (Tsui et al., 2004). The active component of the muscle is regulated by muscle length, contraction velocity, and activation function (Johansson et al., 2000), and is involved in the production of movement and the stabilization of body positions (Tortora, 2005). Activation of a muscle increases its stiffness, which alters the extent to which shock can be attenuated by that muscle (Holmes & Andrews, 2006). Additionally, the activation of muscles crossing a joint increases the stiffness of that joint, which is critical for joint stability, posture maintenance, and locomotion (Tortora, 2005). Conversely, passive muscle force is associated with the muscle’s connective tissues and

fibres, and undergoes an exponential increase with an increase in muscle length (Van Eijden et al., 2002). The passive component is thought to be involved in the storage of elastic energy, thereby enabling a reduction in the energetic cost of movement, and also contributes to postural support and the maintenance of joint resting positions (Van Eijden et al., 2002).

#### **2.2.4 Heel Pad**

The heel pad is a thick layer of fat and connective tissue located inferior to the calcaneus (Bennett & Ker, 1990). The heel pad consists of septa that form a matrix of elastic fibrous connective tissue, which encloses sealed spiral microchambers of unsaturated fat (Gefen et al., 2001; Spears et al., 2005). This compartmentalization of the heel pad restricts movement of the adipose tissue during compressive loading (Bennett & Ker, 1990). The heel pad functions to absorb shock and reduce excessive local stresses and plantar pressures (Miller-Young et al., 2002). The mechanical behaviour of the heel pad depends upon its material properties, shape, and thickness, as well as applied forces and shoe characteristics (Miller-Young et al., 2002).

During gait, the heel pad compresses in order to dissipate the energy resulting from each heel strike. Gefen et al. (2001) observed that a period of rapid compression was characteristic of the heel pad during the initial 150 ms of the contact and heel strike phases of gait, with a deformation of up to 40% during walking (Table 1). Further, De Clercq et al. (1994) found that the heel pad deformed by approximately 60% during running (Table 1). The majority of energy that acts to deform the heel pad at impact dissipates, with very little recovery of energy during elastic recoil (Bennett & Ker, 1990).

Similar to the other soft tissues in the body, highly non-linear stress-strain relationships have been found to be characteristic of heel pad tissue (Bennett & Ker,

1990; Gefen et al., 2001; Miller-Young et al., 2002). Various authors have concluded that heel pad tissue demonstrates low initial stiffness, while increases in applied load (Bennett & Ker, 1990; Miller-Young et al., 2002), impact velocity (Miller-Young et al., 2002), and deformation (Gefen et al., 2001) result in elevated stiffness. For example, De Clercq et al. (1994) found that during running, the average initial heel pad stiffness was  $135 \times 10^3$  N/m, while the average final heel pad stiffness increased to  $634 \times 10^3$  N/m. Stiffness is also affected by the thickness of the pad, with thinner heels generally exhibiting greater stiffness values (Spears & Miller-Young, 2006).

**Table 1:** Mean (SD) characteristics of the heel pad during walking and running.

Activity		Participant 1	Participant 2
Barefoot walking (Gefen et al., 2001)	Unloaded thickness (mm)	11.2 (0.2)	13.1 (0.2)
	Maximal deformation (mm)	3.8 (0.5)	4.8 (0.5)
Barefoot running (De Clercq et al., 1994)	Unloaded thickness (mm)	15.3 (0.2)	14.5 (0.2)
	Maximal deformation (mm)	9.0 (0.5)	9.0 (0.5)

Average heel pad thicknesses have been cited by Gefen et al. (2001) as 18 mm, although the thickness of the heel pad has been recognized as highly variable even across normal populations (Spears & Miller-Young, 2006). Further, Rome et al. (1998) observed that heel pad thickness varied based on whether the participant was bearing weight at the time of measurement. When ultrasound measurements were taken with participants in weight-bearing and non-weight-bearing positions, the mean measured heel pad thicknesses were 4.1 mm and 12.5 mm, respectively (Rome et al., 1998).

#### 2.2.4.1 Heel Pad Paradox

Prior to 1995, confusion arose within the literature regarding heel pad properties, which varied depending on whether tissues were tested in vivo or in vitro (Table 2) using impact pendulum and material testing protocols, respectively. Previous testing had established that in vivo heel pad tissues were characterized by stiffnesses six times lower

in magnitude than those of in vitro tissues, and dissipated three times more energy during impact (Aerts et al., 1995). Aerts et al. (1995) sought to resolve this paradox, and determined that isolated heel pads yielded the same mechanical properties regardless of the testing method, assuming that the protocols were performed properly. The authors concluded that the measurements taken during in vivo pendulum testing were influenced by the presence of the rest of the lower extremity (Aerts et al., 1995). Pain and Challis (2001) further resolved the heel pad paradox using modelling techniques to simulate the heel pad deformation and impact pendulum techniques, which paralleled in vitro and in vivo testing, respectively. The simulations mimicking in vivo conditions indicated that as relative motion of the bone and soft tissues was allowed during pendulum impacts, the properties of the heel pad changed from those observed during in vitro simulation (Pain & Challis, 2001). These findings agreed with those of Aerts et al. (1995), that the presence of the lower extremity during in vivo testing affects measured heel pad properties.

**Table 2:** Comparison of in vivo and in vitro heel pad properties (Pain & Challis, 2001).

	In Vivo	In Vitro
Stiffness at 1BW loading (kN/m)	150	900-1445
Energy loss (%)	95	30
Peak force (N)	800	1800
Frequency dependency	Frequency dependent	Not frequency dependent

### 2.3 Impact Forces

In the study of gait and locomotion, various terms are used to describe the impact of the foot with the ground, and the subsequent events. Impact forces are defined as the forces that occur due to the collision between the foot and the ground, while the impact peak is the maximum amplitude of the force during the impact phase (Nigg et al., 1995). Ground reaction forces (GRFs) are the forces that occur due to the ground acting on the foot following impact (Challis & Pain, 2008). Additionally, GRFs are equal in magnitude and opposite in direction to the forces that the body exerts on the ground, and reach their peak value within approximately 50 ms following the touchdown of the foot (Nigg et al., 1995). Although GRFs are an external measure of loading, it is often assumed that these forces are also representative of internal measures, such as bone loading and injury, as direct measures of bone loading are extremely difficult to obtain in vivo (Miller & Hamill, 2009).

Following impact, the ground reaction force from the foot-ground contact is transmitted through the ankle joint, along the tibia, across the knee, and through the femur (Whittle, 1999). This results in the transmission of a wave of force through the skeleton, which is associated with an acceleration (Whittle, 1999). The term ‘shock wave’ refers to the propagation of this stress wave through the body’s tissues. This term has been used throughout the literature by various authors to describe the response of the lower extremity to impact (Derrick et al., 1998; Dufek et al., 2009; Flynn et al., 2004; Hamill et al., 1995; Holmes & Andrews, 2006; Lafortune, 1991; Lafortune et al., 1995, 1996a, b; McMahan et al., 1987; Mercer et al., 2002, 2003a, b; Milner et al., 2006; Verbitsky et al., 1998; Voloshin et al., 1998; Voloshin & Wosk, 1982; Whittle, 1999; Wosk & Voloshin, 1981). Previous authors have quantified the shock waves resulting from running impacts

by using skin-mounted accelerometers to externally measure accelerations occurring at the distal (Chavet et al., 1997; Mercer et al., 2002, 2003a, b) or proximal (Flynn et al., 2004; Holmes & Andrews, 2006; Schinkel-Ivy et al., 2010) tibia, femoral condyles (Wosk & Voloshin, 1981), or head (Hamill et al., 1995; Mercer et al., 2003b; Wosk & Voloshin, 1981). Additionally, according to Nigg et al. (1995), ‘shock’ refers to the transient condition that occurs following a sudden change in force application, causing the disruption of a system’s equilibrium; this disruption occurs due to a discontinuity between stressed and unstressed regions. Finally, ‘shock attenuation’ is used to describe a reduction in impact force amplitude (Nigg et al., 1995).

### ***2.3.1 Relation Between Injury and Impact Forces***

As numerous factors affect both the magnitude of impact forces experienced by an individual and the risk of lower extremity injury for that individual, associations have been found between impact forces and injury risk, but the relationship has yet to be clearly elucidated. The body’s tissues experience an increase in stresses when subjected to greater impact forces and torques; these stresses must then, in turn, be accommodated or attenuated (Dufek & Bates, 1991). Failure to do so when the body is exposed to excessive stresses may increase the risk of anatomical injury (Dufek & Bates, 1991). Specifically, greater peak forces and loading rates may result in an increased risk of bony injuries such as osteoarthritis and stress fractures (Butler et al., 2003). Animal studies using rabbits have shown that repetitive loading applied at the foot may lead to cartilage degeneration at the knee joint, and changes in the properties of the subchondral bone deep to the cartilage (Radin et al., 1973; Serink et al., 1977). The changes in the rabbits’ knee joints were similar to those observed in degenerative joint conditions in humans (Radin et al., 1973). Further, when canine legs were loaded in three-point bending conditions in

vivo, the loaded limbs displayed greater microdamage than the control limbs (Burr et al., 1985).

Research using human participants has also shown relationships between impact forces and bony injuries such as stress fractures. Grimston et al. (1991) measured forces experienced by runners with and without a history of stress fractures, and concluded that runners with a stress fracture history experienced greater normalized vertical impact forces and maximal medial, lateral, and posterior forces. Similarly, Milner et al. (2006) found greater tibial shock and instantaneous and average vertical loading rates in runners with tibial stress fractures, compared to those without stress fractures.

### **2.3.2 *Running Mechanics***

During running, the feet collide with the ground in a repetitive fashion. At a horizontal running speed of 3 m/s, the vertical component of landing velocity reaches 0.8 m/s; the vertical component increases to 1.9 m/s at a horizontal running speed of 6 m/s (Nigg et al., 1987). When a human pendulum approach is used to administer impacts similar to those seen during running, impact velocities of 1.0-1.15 m/s are often selected (Duquette & Andrews, 2010a, b; Flynn et al., 2004; Holmes & Andrews, 2006; Lafortune et al., 1996a), which fall within the range of the vertical component of landing velocity observed during running (Nigg et al., 1987).

With respect to the forces imposed on the body, the vertical GRF pattern characteristic of running consists of an impact force peak and an active force peak (Nigg & Liu, 1999) (Figure 5). The former results from the collision of the foot with the ground (Derrick et al., 2000), occurs within the first 50 ms following impact (Nigg et al., 1995), and reaches magnitudes of up to 2.2 times body weight (BW) (Cavanagh & Lafortune, 1980). The impact peak occurs during the passive phase, before the muscles have time to

respond to the impact (Nigg & Liu, 1999). Conversely, the active force peak results from muscular activity, which functions to arrest and reverse the downward motion of the body's centre of mass (Derrick et al., 2000). Cavanagh and LaFortune (1980) observed that the active peak reached magnitudes of 2.8 BW in heel-toe runners; these authors also found that the mean peak-to-peak vertical, antero-posterior, and medio-lateral force components were 3.0, 1.0, and 0.3 BW, respectively. The increased muscular forces during the active phase result in an increase in peak joint contact force magnitudes, compared to those experienced during the impact phase (Nigg et al., 1995).

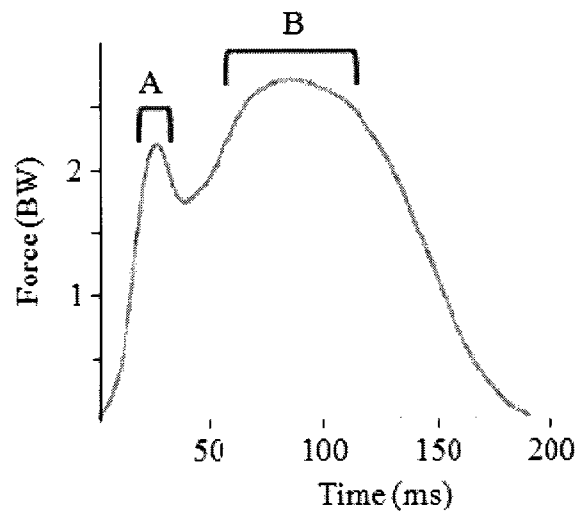


**Figure 5:** Mean ground reaction force profile resulting from 5 participants running at 4.5 m/s across a force plate. A = impact peak; B = active peak (Adapted from Cavanagh & LaFortune, 1980).

### 2.3.3 Factors Affecting Impact Forces

#### 2.3.3.1 Running Kinematics

Variations in impact forces may be attributable to changes in kinematic factors. At a constant velocity, stride length is positively related to the magnitude of impact loading (Derrick et al., 1998). Vertical heel velocity at impact exerts a positive effect on impact peak force and loading rate (Gerritsen et al., 1995). Conversely, the angular

velocities of the segments of the lower extremity do not substantially influence impact peak force or loading rate (Gerritsen et al., 1995).

#### *2.3.3.2 Body Positions and Movements at Impact*

The position of the body at impact, and more specifically that of the segments of the lower extremity, affects the impact forces experienced at the foot (Nigg & Liu, 1999). A greater degree of extension at the knee results in greater peak impact forces (Gerritsen et al., 1995; Nigg et al., 1995). Similarly, a lesser degree of dorsiflexion at the ankle (resulting in a flatter landing) has been found to be correlated with an increase in impact forces and loading rates (Gerritsen et al., 1995).

#### *2.3.3.3 Surface Stiffness*

Using a direct dynamics simulation approach, Gerritsen et al. (1995) investigated the effects of the stiffness properties of a landing surface during an impact. It was found that higher impact peak forces were associated with increased landing surface stiffness (Gerritsen et al., 1995). Further, Ferris and Farley (1997) asked participants to hop on compliant and very stiff surfaces, and concluded that participants increased lower extremity stiffness when hopping on the compliant surface, thereby maintaining a relatively constant total stiffness, calculated as the sum of the leg and surface stiffness.

#### *2.3.3.4 Passive Structures*

Total bone mass, or the mass of the rigid tissues, has been shown to affect peak vertical GRFs. Liu and Nigg (2000) found that as the proportion of rigid mass within the lower extremity of a model increased, so too did the impact force peak. Similarly, Pain and Challis (2004) used a three-link wobbling mass model to simulate drop landings, and concluded that peak vertical GRFs increased with increases in bone mass. Specifically, a 20% increase in bone mass produced a 13% increase in peak vertical GRF (Pain &

Challis, 2004). Additionally, using the same model, Pain and Challis (2004) established that the stiffness of the heel pad also positively affected impact forces, in that a 20% increase in heel pad stiffness resulted in a 5% increase in peak vertical GRF.

The locations of the segments with respect to the point of impact also affect impact forces. By altering the masses of the shank, thigh, and trunk segments in a computer model, Pain and Challis (2004) found that peak vertical GRFs changed by 340 N/kg, 157 N/kg, and 24 N/kg, respectively, thereby establishing that the segments closer to the point of impact exerted a greater influence over the peak vertical GRFs than more proximal segments. It is for this reason that the foot, shank, and thigh (the body segments closest to the point of impact) are being examined in the present study, as opposed to larger, more proximal segments.

#### *2.3.3.5 Muscles*

Both the passive and active components of muscle tissue influence impact loading within the lower extremity. The presence of muscles within a lower extremity model was found to reduce peak impact forces and maximal loading rates in comparison to a model in which muscles were not present (Gerritsen et al., 1995). Wright et al. (1998) utilized a lower extremity model to investigate the effects of changing shoe hardness, and found no significant differences in peak impact forces for hard and soft shoe conditions. As the initial kinematics and muscle activation levels at impact were held constant, it was concluded that a passive mechanical response was employed within the lower extremity to regulate impact forces (Wright et al., 1998). Further, the inertial properties of the tested system (i.e. lower extremity segments) and the masses of the segments involved in deceleration upon impact affect the impact forces acting at the foot (Nigg & Liu, 1999).

Impact forces are also influenced by the activation of lower extremity musculature (Cole et al., 1996). The activation of extrafusal muscle fibres results in increased stiffness of the muscle (Latash & Zatsiorsky, 1993), thereby contributing to an increase in impact forces (Butler et al., 2003; Nigg et al., 1995) and loading rates (Butler et al., 2003). Pain and Challis (2002) found that increased muscle stiffness during forearm impacts contributed to a greater peak impact force and decreased time to peak force. In addition to increasing the stiffness of the muscle itself, activation also acts to increase the stiffness of the joint(s) that the muscle crosses. Joint stiffness is determined from the slope of the moment-angle relationship at a joint (Stefanyshyn & Nigg, 1998), although this should technically be termed 'quasi-stiffness', as measurements are not performed at equilibrium, and the time course of the displacement is not accounted for (Latash & Zatsiorsky, 1993). Elevated joint stiffness is also associated with increased impact forces; Milner et al. (2007) found that compared to runners without a history of stress fractures, those with such a history exhibited both increased joint stiffness at the knee and increased vertical GRFs during the impact phase.

## 2.4 Shock Transmission and Attenuation

It has been shown that as the shock wave generated by the foot contact with the ground passes through the body, the body's tissues act to attenuate the signal (Dufek et al., 2009; Hamill et al., 1995). While the properties of specific tissues with respect to shock transmission have been determined, the response of the body as a system remains unclear (Lafortune et al., 1996b). However, evidence existing within the literature suggests that the body's ability to transmit shock is characterized by non-linear properties (Lafortune et al., 1996b).

In order to examine the shock absorbing capacity of the body, Wosk and Voloshin (1981) used accelerometers to measure participants' peak accelerations (PA) at the tibial tuberosity, medial femoral condyle (proximal to the knee), and forehead during walking, from which they were able to calculate the extent to which PA was attenuated as the shock wave passed through each region. They determined that 30% of the PA was attenuated across the knee joint, with further attenuation of 40% by more proximal body segments, demonstrating that up to 70% of the PA was attenuated by the time the shock wave reached the head (Wosk & Voloshin, 1981).

The degree of shock attenuation by the body is dependent on the magnitude of shock input into the system (Hamill et al., 1995). For example, Derrick et al. (1998) and Mercer et al. (2003b) observed that with increases in impact forces, the shock wave was attenuated to a greater extent by the tissues of the body. The body's capacity to alter its shock attenuation properties, as a function of impact loading, ensures that the accelerations reaching the head following impact are maintained at a consistent magnitude (Hamill et al., 1995) (Figure 6), thereby allowing stability of the head during repetitive impact loading (Derrick et al., 1998).

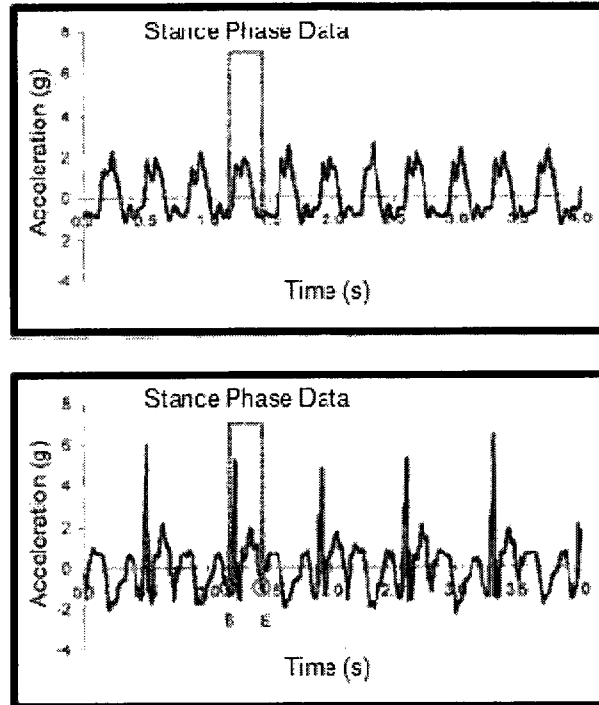


**Figure 6:** Acceleration profiles for the head (top) and distal tibia (bottom) during running at 3.8 m/s (Adapted from Mercer et al., 2003b).

#### **2.4.1 Shock Propagation Through the Lower Extremity and Effects of Soft Tissue**

During locomotion, the impact of the foot with the ground generates a shock wave, which ascends through the body (Dufek et al., 2009). The speed of shock wave propagation along the longitudinal axis of long bones is approximately 3200 m/s (Chu et al., 1986; Pelker & Saha, 1983). However, the speed of propagation in vivo is mitigated by movement of the soft tissues of the leg relative to the underlying bone (Dufek et al., 2009), which occurs in response to any impulsive loading applied to the skeletal system (Challis & Pain, 2008). Through this motion of the soft tissues, the acceleration and loading of the musculoskeletal system may be decreased (Challis & Pain, 2008).

Upon impact of the heel with the ground, the heel pad undergoes a deformation (Challis & Pain, 2008), enabling energy dissipation of approximately 18% (Gefen et al.,

2001). The impact force is transferred proximally, causing a transient deformation of soft tissue in a wave-like motion along the leg (Challis & Pain, 2008). This effect occurs due to the unbalanced forces acting on the distal end of the limb (Nigg et al., 1995), and the viscoelastic properties of soft tissues, which act to return the system to equilibrium upon removal of the force (Challis & Pain, 2008). Following a forearm impact, Pain and Challis (2002) found that the system returned to equilibrium in 200-250 ms (Figure 7a). Similar results have been found for human pendulum impacts (Lafortune et al., 1996a) and drop landings (Andrews & Dowling, 2000) (Figure 7b). Viscoelastic properties enable the tissues to passively absorb and dissipate the energy of a shock wave, which attenuates the amplitude of the wave as it passes through the tissues (Nigg et al., 1995).

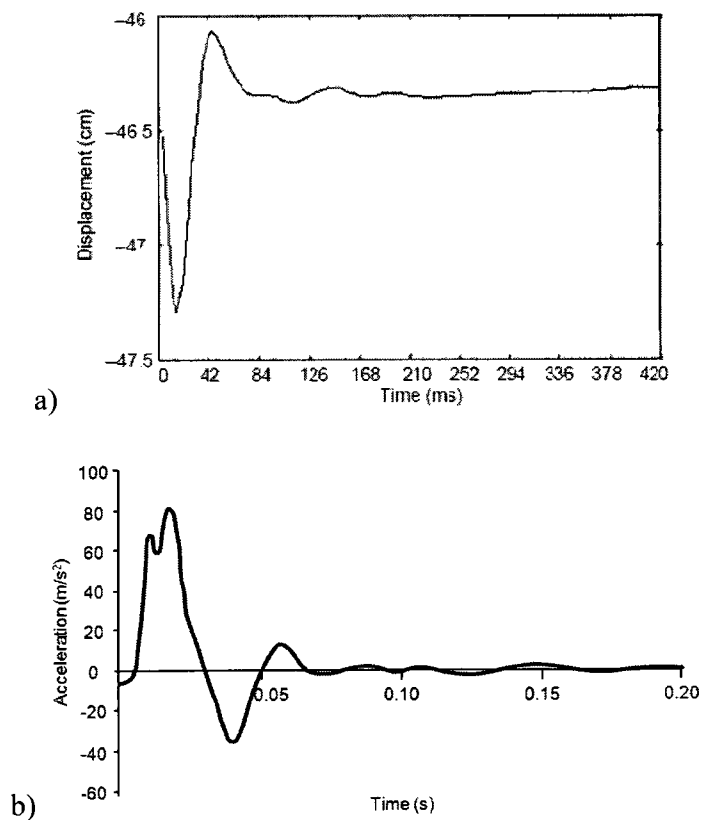


**Figure 7:** a) Displacement of a forearm marker following impact (Pain & Challis, 2002);  
b) Acceleration at the proximal tibia following impact (Adapted from Andrews & Dowling, 2000).

The rate of propagation of the shock wave through and between the structures and tissues of the lower extremity depends on the stiffness of the components of the lower extremity structures, as well as the stiffness of the coupling between those components (Challis & Pain, 2008). By measuring marker motion at proximal and distal points on the soft tissue of the upper extremity, Pain and Challis (2002) determined that the shock wave propagated through the soft tissue at approximately 37 m/s (compared to the rate of 3200 m/s for bone, found by Chu et al. (1986) and Pelker and Saha (1983)). Due to the differing speeds of shock wave propagation in rigid and soft tissues, acceleration data collected during gait impacts reveals two separate frequency components for the shank: a high component resulting from the collision of the skeleton with the ground, and a low component resulting from soft tissue motion (Challis & Pain, 2008) (Figures 8 & 9).

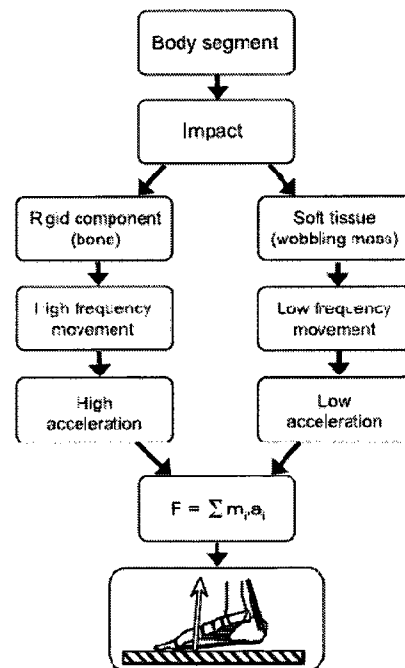


**Figure 8:** The accelerations occurring in rigid and soft tissues following impact. Low and high frequency movements both contribute to ground reaction forces (represented by the arrow in the bottom panel) (Challis & Pain, 2008).

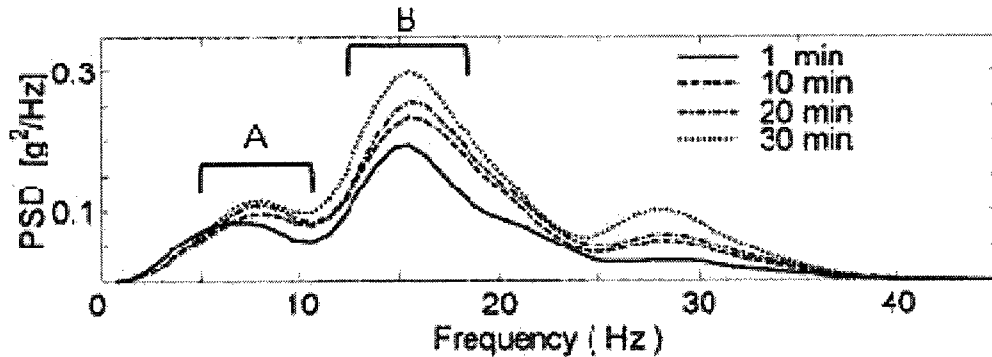


**Figure 9:** Average power spectral densities for 14 participants at four times throughout a 30 minute run. A = low frequency movements due to soft tissue motion following impact; B = high frequency accelerations due to the collision of the skeleton with the ground (Adapted from Mizrahi et al., 2000).

The impact forces resulting from the foot-ground collision result in a non-uniform distribution of stresses and strains within the lower extremity (Nigg et al., 1995; Shen et al., 2008), due to the geometry and material properties of the various structures (Shen et al., 2008). Further, once the shock wave has propagated along the length of a segment, it is not only transmitted to the more proximal segment through the joint; it is also reflected back towards the location at which the load was originally imposed (Nigg et al., 1995). This results in wave propagation in both directions along the segment (from the source and the reflected wave), which, when combined with the finite speed at which the waves can propagate, results in the non-uniformity of stresses within the lower extremity (Nigg et al., 1995). When stresses or strains exceed the strength of the tissue, damage may be sustained within those tissues (Shen et al., 2008).

Numerous studies have employed modelling techniques in order to establish the effects of soft tissues on shock attenuation. Rigid body models allow for simplification of the human body, by using only rigid bodies to represent each of the segments selected for modelling. However, models incorporating soft tissues, referred to as wobbling mass

models, account for the movements of muscle and other soft tissues in response to impact. The soft tissues, or wobbling masses, are also generally modelled as rigid bodies (Gittoes & Kerwin, 2009; Gruber et al., 1998), and are coupled to the segments representing the rigid masses using spring-damper systems (Gittoes et al., 2006; Gittoes & Kerwin, 2009; Pain & Challis, 2004) (Figure 10). This technique enables the movement of the wobbling mass relative to the rigid mass, allowing for rotation about the transverse axis, and translational movement both parallel and perpendicular to the bone's longitudinal axis (Gittoes et al., 2006; Gittoes & Kerwin, 2009).

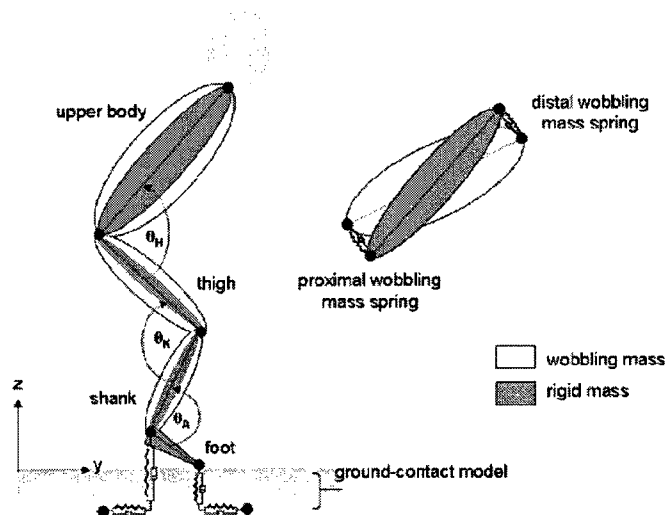


**Figure 10:** Wobbling mass model. Spring-damper systems are located at both ends of each segment, connecting the rigid and wobbling masses (Gittoes & Kerwin, 2009).

Various authors have compared the outputs of rigid mass (RM) models to those of wobbling mass (WM) models. The outputs of the two types of models have been found to be dramatically different for both heel (Gruber et al., 1998; Pain & Challis, 2001, 2006) and forefoot (Gittoes et al., 2006) landings (Figure 11). Specifically, the WM aids in the dissipation of energy during impact (Pain & Challis, 2001), as well as the reduction of external impact loading, joint forces, and joint torques (Gittoes et al., 2006; Gruber et

al., 1998; Liu & Nigg, 2000; Pain & Challis, 2004, 2006). Further, Cole et al. (1996) and Gittoes et al. (2006) found that a WM model was a better predictor of experimental kinematic measurements than an RM model. It was concluded by Liu and Nigg (2000) that RM models may be appropriate for the investigation of slow, quasi-static movements, but generally not for impact scenarios.

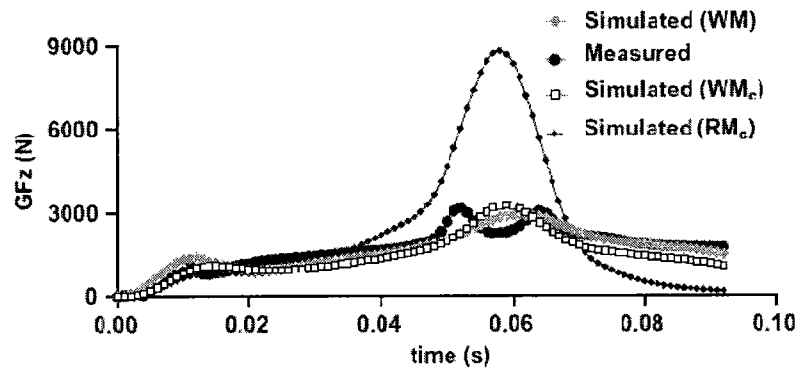


**Figure 11:** A comparison of vertical ground reaction forces for an experimental trial and wobbling mass (WM) and rigid mass (RM) model simulations. The inputs for WM were movement-specific optimized values, and those of WM<sub>c</sub> and RM<sub>c</sub> were independent optimized parameters (Gittoes et al., 2006).

## 2.4.2 Factors Affecting Shock Attenuation

### 2.4.2.1 Kinematics and Lower Extremity Positions

Factors such as impact velocity, stride length, and stride frequency affect shock attenuation in the lower extremity. Increases in impact velocity are associated with an increase in peak shock and decrease in time to peak shock (Lafortune et al., 1996b).

Similarly, as the forward velocity of progression increases, so too does the magnitude of the tibial impact shock (Derrick et al., 1998); the amount of shock attenuation increases as well (Mercer et al., 2002), in order to counteract the increase in shock. Further, both Derrick et al. (1998) and Mercer et al. (2003b) have shown that increases in stride length result in an elevated degree of shock attenuation. However, the effects of stride

#### *2.4.2.2.1 Passive Shock Attenuating Mechanisms*

The body has several mechanisms by which shock may be passively attenuated. Modification of the running surface is a strategy often employed by runners (Dufek et al., 2009); changes in running shoes are another possible modification. When examining biological structures within the lower extremity, both soft (heel pad, cartilage, muscles, etc.) and rigid tissues contribute to passive shock attenuation. The heel pad provides a substantial amount of shock absorption, by deforming upon contact with the ground (Bennett & Ker, 1990). The energy associated with this deformation dissipates, with very little recovery of energy during the elastic recoil (Bennett & Ker, 1990). Both the heel pad and soft tissues of the shank contribute to energy dissipation following impact (Pain & Challis, 2001).

The role of articular cartilage and menisci within the knee joint was clarified by Fukuda et al. (2000), using cadaveric specimens. These authors concluded that both structures contributed to shock attenuation, with a greater contribution from the menisci. In comparison to rigid tissues, cartilage is a more effective structure for the attenuation of shock than bone. However, the small volume of articular cartilage in the lower extremity requires that the long bones of the lower extremity be responsible for a greater proportion of shock attenuation relative to articular cartilage (Nigg et al., 1995).

The masses of both rigid and soft tissues have also been shown to contribute to the attenuation of shock through the shank (Schinkel-Ivy et al., 2010). A human pendulum apparatus was employed to administer impacts to the heel, and the peak acceleration (PA), time to peak acceleration (TPA), and acceleration slope (AS) medial to the tibial tuberosity were measured. In general, PA and AS tended to decrease, while TPA tended to increase, as the masses of the tissues in the shank (bone, lean, and fat masses)

increased. Additionally, relative to the lean mass and bone mineral content of the shank, males experienced significantly lower peak accelerations and acceleration slopes. These results implied that the greater absolute lean mass and bone mineral content found in males led to decreased relative acceleration responses following impact, compared to females (Schinkel-Ivy et al., 2010).

#### 2.4.2.2.2 *Active Shock Attenuating Mechanisms*

The active attenuation of shock is primarily attributable to the activity of the musculature within the lower extremity, due to both its capacity for deformation in response to imposed loading, and its capability to adjust the amount of shock attenuation by varying activation level (Derrick et al., 1998). As the level of activation within a muscle increases, so too does the stiffness of the muscle; in turn, these changes in lower extremity stiffness influence shock attenuation (Mercer et al., 2003b). Similarly, increased activation of the muscles crossing a joint, or an increase in the number of recruited muscles around that joint, result in an elevation of the effective stiffness of that joint (Mukherjee et al., 2007). It is generally accepted that the stiffness of the body is determined by the individual stiffness values for the various tissues within the body (Latash & Zatsiorsky, 1993), and is activity dependent (Butler et al., 2003).

While increased stiffness may generally be considered to improve performance, the body may optimize the amount of stiffness in order to minimize the risk of injury (Butler et al., 2003). Inadequate or excessive stiffness may act to increase the risk of injury to bone and to soft tissues, respectively. In a series of studies by Williams et al., the authors observed that runners with high arches (typically associated with more rigid feet) exhibited increased leg and knee stiffness (Williams et al., 2004), and experienced a higher incidence of bony injuries, compared to runners with low arches (Williams et al.,

2001a). The latter was attributed to the increased vertical loading rate observed in that group, compared to the low-arch runners (Williams et al., 2001b). Further, low-arch runners (typically associated with more compliant feet) experienced a higher incidence of injury to the soft tissues, such as tendons, ligaments, muscles, the iliotibial band, and the plantar fascia (Williams et al., 2001a). The authors suggested that this may be due to an overload of the force-attenuating structures, thereby causing eccentric muscle activity (Williams et al., 2004). Additionally, Granata et al. (2002) proposed that the reduced leg stiffness during hopping that they observed in females (compared to males) may contribute to the well-documented increased risk of lower extremity soft tissue injuries in females (for example, Jones et al., 1993; Messina et al., 1999), such as knee sprains, anterior cruciate ligament injuries, and meniscal and cartilaginous tears.

Holmes and Andrews (2006) examined the effects of increased muscle activation on the transmission of shock through the shank, using a human pendulum to administer controlled impacts. The authors measured the acceleration waveform medial to the tibial tuberosity, and found that increases in the level of activation of the tibialis anterior muscle were associated with increases in peak acceleration and acceleration slope, along with decreases in time to peak acceleration. It was therefore concluded that increased activation and stiffness within the shank musculature resulted in a decreased capacity of the soft tissues of the shank to attenuate shock (Holmes & Andrews, 2006).

In addition to increased stiffness, muscle activation during ambulatory impacts may also serve to minimize vibrations of the soft tissues. Vibration is an oscillatory motion (Cardinale & Pope, 2003), and in this context refers to the damped oscillation of the soft tissues of the lower extremity in response to impact, which is subsequently transferred to adjacent soft tissues (Wakeling & Nigg, 2001). During running, a leg

acceleration profile is characterized by low-, mid-, and high-frequency components (Hamill et al., 1995). The low-frequency component ranges from 4-8 Hz and results from the active phase of contact, in which the musculature of the leg is activated; the mid-frequency component ranges from 12-20 Hz and results from the impact phase, when the foot first contacts the ground; and the high-frequency component ranges from 60-90 Hz and is associated with the resonant frequency of the accelerometer (Hamill et al., 1995; Mizrahi et al., 2000). However, the range corresponding to the mid frequency component coincides with the natural frequency of the lower extremity soft tissue packages, which is thought to lie within the range of approximately 5-60 Hz (Nigg et al., 2003; Wakeling et al., 2002, 2003). This may result in the potential for soft tissues to vibrate at their resonant frequency in response to impact (Wakeling et al., 2003). A resonant response within the soft tissues may cause discomfort and elevated stresses within the tissues, ultimately leading to an increased risk of injury during repetitive activities (Boyer & Nigg, 2006). Although it may seem that the soft tissue packages of the lower extremities could potentially reach their resonant frequency following exposure to the impact forces experienced during running, observations indicate that there is minimal vibration of the soft tissue following impact (Wakeling & Nigg, 2001). It has been proposed that upon heel strike, muscle activation assists in the damping of soft tissue resonance, thereby minimizing the amount of oscillation by the soft tissues (Wakeling et al., 2003).

Therefore, it has been proposed that the muscles may be 'tuned' in order to minimize potential soft tissue vibration resulting from impacts (Wakeling & Nigg, 2001; Wakeling et al., 2002). This can be done in several ways, such as decreasing the magnitude of force transmitted to the soft tissues, altering the resonant frequency of the soft tissues, or improving the damping properties of the tissues (Wakeling et al., 2001,

2003). The activation of the lower extremity musculature, and subsequent muscle force production and increases in muscle shortening velocity, act to increase the damping and natural vibration frequency of the soft tissues in order to avoid resonance (Wakeling & Nigg, 2001; Wakeling et al., 2001). The effect of muscle activation during heel-toe running was shown by Boyer and Nigg (2004), in that the response of the muscles to the impacts increased as the resonant frequency of the soft tissues and the frequency of the input signal approached similar values.

Finally, activation of the musculature leads to fatigue, which, depending on the type of fatigue, may contribute to shock attenuation. The literature provides two differing conclusions regarding the effects of fatigue on shock attenuation, contingent upon whether the fatigue was induced at the level of the whole body, or locally, at the level of the muscle. Whole body fatigue is generally induced by means of cardiovascular activity, such as running, for a specified period of time (Mercer et al., 2003a; Mizrahi et al., 1997, 2000; Verbitsky et al., 1998; Voloshin et al., 1998). The results of whole body fatigue studies reach a general consensus that accelerations resulting from impact, as measured at either the distal tibia or tibial tuberosity, tend to increase as fatigue progresses, indicating that the body's capacity to attenuate shock decreases in the fatigue state. Conversely, Duquette and Andrews (2010b), Flynn et al. (2004), and Holmes and Andrews (2006) examined the effects of local muscle fatigue, by inducing fatigue in either the tibialis anterior or gastrocnemius muscles and measuring accelerations medial to the tibial tuberosity in response to impact. All studies identified decreased peak accelerations and acceleration slopes in females following fatigue, and Duquette and Andrews (2010b) and Holmes and Andrews (2006) also observed an increase in time to peak acceleration.

These results indicate that localized muscle fatigue causes the muscle to become less stiff,

thereby contributing to an increase in shock attenuation following impact (Duquette & Andrews, 2010b; Flynn et al., 2004; Holmes & Andrews, 2006). This phenomenon may provide a protective effect to the bony structures of the lower extremity in the fatigue state, as decreased lower extremity stiffness has been associated with a lower incidence of bony injuries, such as stress fractures (Williams et al., 2001a, 2004).

## 2.5 Biomechanical Modelling

Two of the major limitations that exist when researching humans are natural human variability and inaccessibility of desired measurements. With respect to the former, there is so much variability inherent in humans, not only between-, but also within individuals, that it is exceedingly difficult to control for all known and unknown confounding variables. With respect to the latter, serious ethical concerns are involved. For example, the use of a bone-mounted accelerometer is more invasive than a surface-mounted accelerometer, and involves more discomfort and risk of infection. Further, it is not currently possible to take measurements internal to the human body without altering the measurements themselves. At best, a measure such as stress can be calculated from in vivo measurements, but there may be so many assumptions inherent in the solution that the final answer is rendered useless (Bobbert et al., 1992).

In order to overcome these limitations, computer simulation and modelling studies have been employed. Although not without their own set of limitations, these studies have enabled researchers to achieve insights into the biomechanical response of the body and injury mechanisms (Mukherjee et al., 2007). Moreover, the mechanical contributions of the various components of the body, such as soft tissues, to impact loading (Gittoes & Kerwin, 2009) have been examined. Simulation models may also be used to investigate the kinematics and kinetics of a particular system and the influence of controlled changes in input variables on the measured outputs (Nigg et al., 1995). For example, Liu and Nigg (2000) employed simulations to determine the effects of varying body masses on the output variable of a system, with unchanged springs and dampers within the system. Further, computer simulation techniques may also be used to model musculoskeletal joints and limbs, in order to investigate joint interactions and kinematics, spatial

orientation of bones or appendages, lengths of muscles or ligaments, forces and moments of muscles, contact pressures within joints, and ranges of motion at particular joints (Liacouras & Wayne, 2007). However, it is necessary to consider that the validity of the results output from a model is dependent on the assumptions inherent in the model, as well as the mechanical and conceptual construction of the model (Nigg et al., 1995).

Two of the approaches most commonly used in the development of these types of biomechanical models are the multi-body system approach and the finite element analysis (FEA)-based approach (Liacouras & Wayne, 2007; Mukherjee et al., 2007). The methodology of the present study will focus on the latter approach, using a human finite element model subjected to gait-type impact conditions to predict forces at the point of contact between the foot and the wall, and accelerations at specified locations along the lower extremity of the model.

## 2.6 Finite Element Analysis

Finite element analysis (FEA) is a computational technique that was originally developed in engineering mechanics (Zhang et al., 1998). This method was first applied in the field of biomechanics by several research groups in the 1970s (Brown, 2004), and as computing abilities have improved in recent years, it has been widely accepted for use in the analysis of the mechanical behaviour of biological tissues and structures (Taddei et al., 2004). This increase in popularity is understandable, as FEA enables the computation of stresses and strains in structures involving complicated shapes, material properties and distributions, and/or loading distributions and patterns (Brown, 2004; Dar et al., 2002). When any of these characteristics are too complex, as often occurs when examining humans in vivo, analytical and experimental methods are not sufficient (Dar et al., 2002; Lotz et al., 1991). FEA allows for representation of the complex geometric and material property distributions seen in live humans (Lotz et al., 1991). Further, FEA enables variations in the geometric, material, or loading parameters of the model, to explore the effects of those variations on the model outputs (Dar et al., 2002; Lotz et al., 1991).

FEA is used to numerically obtain an approximate solution to Equation 1:

$$\{F\} = [m] \cdot \{\ddot{x}\} \quad [1]$$

where 'F' represents force, 'm' represents mass, and 'x' represents acceleration. This equation embodies Newton's second law of motion, which states that the acceleration of an object is proportional to the force acting upon it, and inversely proportional to its mass. This equation represents an ideal state, and is limited by its assumptions, primarily that the mass is constant and non-deformable. When the focus of an analysis is a biological tissue or structure, the latter assumption does not necessarily hold true. Due to the

capacity of human tissues and structures for deformation, modifications to the equation result in Equation 2:

$$\{F\} = [m] \cdot \{\ddot{x}\} + [c] \cdot \{\dot{x}\} + [k] \cdot \{x\} \quad [2]$$

where ‘c’ represents the damping constant, ‘ $\dot{x}$ ’ represents velocity, ‘k’ represents the stiffness constant, and ‘x’ represents displacement. As can be seen from Equation 2, mass is associated with the inertia of the structure, the damping constant is associated with its viscosity, and stiffness is associated with its displacement.

### ***2.6.1 Advantages and Disadvantages of Finite Element Analysis***

The advantages of FEA make it beneficial for use in the field of biomechanics. Internal stress and strain measurements are difficult to obtain experimentally in vivo. Further, in vitro specimens may be compromised, with loading conditions that may differ from in vivo conditions (Chen et al., 2001). FEA, however, provides predictions of these measurements at any location within the modelled structure (Goh et al., 2005; Limbert et al., 2004; Shen et al., 2008). FEA also enables the analysis of the behaviour of structures of complex geometry, composition, and material properties (Chen et al., 2001; Merz et al., 1996; Voo et al., 1996), and the incorporation of complex boundary and loading conditions for static and dynamic analyses (Chen et al., 2001; Voo et al., 1996).

However, there are also disadvantages to the finite element (FE) method. FEA is generally used to solve a problem because it is challenging to obtain measurements experimentally. Validation of the outputs of the FE simulation is equally difficult; therefore, a major limitation of the method is that adequate experimental validation is lacking in the literature (Limbert et al., 2004). Further, the accuracy of the model outputs is directly related to the accuracy of the model’s material properties, and reliable data of this type are not always available for all materials represented in the model (Nambu &

Lewis, 2004). Often, assumptions are made in order to simplify some of the complex material properties exhibited by biological tissues, such as geometry, non-homogeneity, anisotropy, and viscoelasticity; assumptions may also be made regarding the imposed boundary and loading conditions (Goh et al., 2005; Zhang et al., 1998).

### ***2.6.2 Development of a Finite Element Model***

It is important to ensure that the finite element model (FEM) accurately portrays its in vivo counterpart. This is often accomplished by basing the FEM on scanned images of the structure; computed tomography (CT) (Chen et al., 2001), micro-CT (Bevill et al., 2006), quantitative CT (Lotz et al., 1991), and magnetic resonance imaging (Cheung et al., 2005) are commonly used in the literature. Surface scans (Yosibash et al., 2007) and anatomical sections (Clavert et al., 2006) have also been used for FEM development.

Once the in vivo structure is accurately represented, FEA enables this complex problem domain to be divided into a finite number of smaller domains, each yielding a more manageable solution (Dawson et al., 1999; Zhang et al., 1998). This is referred to as the discretization of the structure. The system is divided into a mesh of simple polyhedral shapes which are connected together at nodes (Dumont et al., 2009). The ability of a FEM to approximate the desired output variables may be enhanced through the use of gradation. This process enables areas of high field gradients, which require increased resolution, to be meshed using a greater number of elements (Cook et al., 2002). This allows for the geometry of the structure to be modelled with greater ease, and also enables more complex deformations and stress and strain distributions to be represented (Dawson et al., 1999). A greater number of elements are critical at locations within the model where there are transitions in geometry or material properties (Dawson et al., 1999).

Each element is then assigned material properties, and boundary conditions are specified. Displacement boundary conditions can be used to either constrain motion or specify non-zero displacements in one or more degrees of freedom (Brown, 2004). Loading conditions are then applied and the software computes the deformation, strain, and stress responses of the structure at any location within the model (Dumont et al., 2009). Model accuracy can be shown through a comparison of the model results with those obtained experimentally and through convergence tests to demonstrate sufficient refinement of the mesh (Gray et al., 2008; Kumaresan et al., 1999).

### ***2.6.3 Stages of Finite Element Analysis***

#### ***2.6.3.1 Pre-Processing Stage***

The pre-processing stage enables the preparation of a model for the analysis (Kim & Sankar, 2009), and includes such issues as discretization. Further, material and geometric representation, distribution of material properties, and specification of loading and boundary conditions must all be considered (Becker, 2004; Brown, 2004; Cook et al., 2002; Voo et al., 1996).

#### ***2.6.3.2 Processing Stage***

In the processing stage, the computational program is executed to produce numerical results (Voo et al., 1996). With user input from the pre-processing stage, the software generates stiffness matrices for each element, which are assembled into a global stiffness matrix for the structure (Becker, 2004) and solved for the unknown degrees of freedom (Kim & Sankar, 2009). Nodal displacements are computed first, followed by deformations, strains, and stresses (Dawson et al., 1999; Johansson et al., 2000).

### *2.6.3.3 Post-Processing Stage*

The final stage of FEA is to present and interpret the computed results (Voo et al., 1996). In this stage, the variables of interest are presented, often graphically (Brown, 2004), and the computed variables may be examined at specific locations within the structure (Becker, 2004). The results of the processing stage may be presented using a variety of displays, such as deformed shape displays, stress contour displays, stress averaging, X-Y charts, or vector plots (Becker, 2004; Kim & Sankar, 2009).

### *2.6.4 Previous Uses of Finite Element Analysis*

The uses of FEA in biomechanics are diverse. FEMs have been employed extensively in the determination of tissue properties (Chawla et al., 2009; Clavert et al., 2006; Miller-Young et al., 2002), and in impact biomechanics for scenarios such as automotive impacts (Kitagawa et al., 2008; Yasuki, 2007) and falls (Lotz et al., 1991). FEA has also been used in the analysis of joint and limb reconstruction and replacement (Gray et al., 2008; Portnoy et al., 2006), and of the stresses in the foot during standing (Cheung et al., 2005) and walking (Gefen et al., 2000).

### *2.6.5 Modelling of In Vivo Tissues*

It is essential that the model parameters accurately represent the structure of interest with respect to anatomy, geometry, material properties, and loading and boundary conditions, to ensure that the outputs are applicable to that structure (Gray et al., 2008; Kumaresan et al., 1999; Miller-Young et al., 2002). However, assumptions are often made initially regarding the material properties of biological tissues, in order to simplify the parameters of the model (Goh et al., 2005; Zhang et al., 1998). As models advance, it is then possible to introduce more complex material properties, in order to more accurately represent the in vivo structures (Brown, 2004). As the availability of tissue

properties in the literature increases, and computational resources improve, the ability of FEMs to determine mechanisms and patterns of injury is advanced (Chawla et al., 2009). Examples of the simplified and complex material properties that have been used in the literature to represent various tissues are presented in Table 3.

**Table 3:** Examples of studies using simplified and complex material properties.

Simplified Material Properties		Complex Material Properties	
Linear	Lotz et al. (1991); Papaioannou et al. (2008)	Non-Linear	Gerritsen et al. (1995); Nigg & Liu (1999)
Isotropic	Zachariah & Sanders (2000)	Anisotropic	Limbert et al. (2004); Puso & Weiss (1998)
Elastic	Cheung et al. (2005)	Visco- elastic	Bandak et al. (2001); Gerritsen et al. (1995); Iwamoto et al. (2003)
Homo- geneous	Song et al. (2004); Zachariah & Sanders (2000)	Hetero- geneous	Yosibash et al. (2007)
Compres- sible	–	Incompres- sible	Song et al. (2004)

### 2.6.6 Validation of a Finite Element Model

The validation of the results of FE simulations is critical, in order to ensure the accuracy of the outputs (Gray et al., 2008; Kumaresan et al., 1999). Validation is also a means of quantifying the performance of the model, and the error between the model and experimental results. This can be accomplished through various means, with the specific method depending on the research questions being answered. Often, the stresses and strains can be compared to the experimental results previously published in the literature (Gray et al., 2008). Conversely, in order to more closely replicate the conditions of a specific FEM, experimental data may be collected using cadavers (Lotz et al., 1991; Song et al., 2004). Other methods, such as the comparison of model results with Contact Pressure Display measurements (Gefen et al., 2000), kinematics (Beillas et al., 2004),

migration and survivorship data (Taylor et al., 1998), and force data collected using a synthetic residual limb within a prosthesis (Portnoy et al., 2006), have also been employed for specific research questions.

#### **2.6.7 *LS-DYNA***

LS-DYNA is a highly advanced general purpose non-linear finite element program. LS-DYNA and its pre- and post-processing software, LS-PREPOST, are developed by Livermore Software Technology Corporation (Livermore, California, USA). LS-DYNA enables the dynamic simulation of complex, real world problems, such as wave propagation (Grimal et al., 2004), as well as those involving large deformations resulting from impacts. LS-DYNA has previously been employed for such applications as investigating the responses of the body during crash testing (Teng et al., 2007), and the mechanisms of injury within the bones of the foot following impact (Bandak et al., 2001). LS-DYNA is also used for the implementation of the Total Human Model for Safety.

#### **2.6.8 *Total Human Model for Safety***

The Total Human Model for Safety (THUMS) was developed by the Toyota Motor Corporation and the Toyota Central Research and Development Laboratories (Iwamoto et al., 2003, 2007; Maeno & Hasegawa, 2001) in conjunction with Wayne State University, to simulate gross motions and stress and strain distributions that occur in humans during automobile impacts. The original THUMS model represented a 50<sup>th</sup> percentile American male (AM-50) occupant, which was modified to represent an AM-50 pedestrian (Maeno & Hasegawa, 2001) (Figure 12). Fifth percentile American female (AF-05) occupant and pedestrian, 95<sup>th</sup> percentile American male (AM-95) occupant, and child pedestrian models have also been developed (Iwamoto et al., 2007). Traditionally, crash test dummies have been used for automobile safety testing and research purposes

(Maeno & Hasegawa, 2001). However, since dummies must withstand repeated impact tests, the strength and endurance may vary from that of humans (Maeno & Hasegawa, 2001). Therefore, a human body FEM, such as the THUMS model, is a substitute for crash test dummies, providing an alternative for automobile safety testing and enabling the investigation of the mechanisms of injury resulting from automobile impacts (Maeno & Hasegawa, 2001; Nagasaka et al., 2003). THUMS also allows for the study of the response of the human body following impact loading (Iwamoto et al., 2003) and the prediction of injury following impact (Iwamoto et al., 2007). THUMS has been used to investigate the response of an occupant to various impact conditions (Oshita et al., 2002), injury mechanisms occurring in a pedestrian in response to a lateral impact (Maeno & Hasegawa, 2001; Nagasaka et al., 2003), and the behaviour of the head and neck of an occupant following an impact (Kang et al., 2005; Kitagawa et al., 2008).

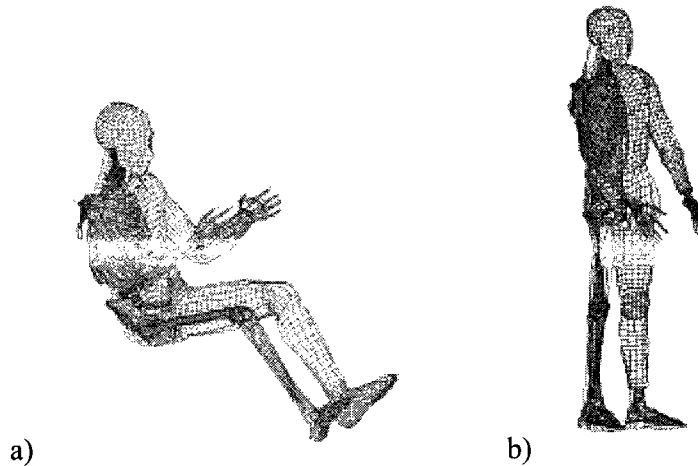


**Figure 12:** a) The AM-50 occupant THUMS model; b) The AM-50 pedestrian THUMS model (Iwamoto et al., 2007).

#### 2.6.8.1 Components of the Total Human Model for Safety

The AM-50 pedestrian THUMS model is based on a 50<sup>th</sup> percentile American male, with a height of 178 cm and a body mass of 78.2 kg (Iwamoto et al., 2003; Maeno

& Hasegawa, 2001). The THUMS model incorporates structures, shapes, and material properties similar to those of a human, in order to achieve a high degree of biofidelity (Maeno & Hasegawa, 2001). Body segment geometry was gathered from human body databases (Kitagawa et al., 2008). All bony components and major ligaments are modelled to enable the accurate representation of a human (Kitagawa et al., 2008). The lower extremity of the model (Figure 13) consists of the pelvis, femur, tibia, fibula, patella, and foot bones, and is capable of large articulating movements at the joints, through the inclusion of ligaments and tendons (Maeno & Hasegawa, 2001) and the definition of contact surfaces between the bones (Kitagawa et al., 2008). This technique allows for realistic joint motions and force transfer across the joint (Kitagawa et al., 2008). Skin, adipose tissue, muscle, and cartilage are also included in the model (Maeno & Hasegawa, 2001). Structural details regarding the THUMS model are located in Table 4, while further information regarding lower extremity material models and contact algorithms can be found in Appendices A and B, respectively.

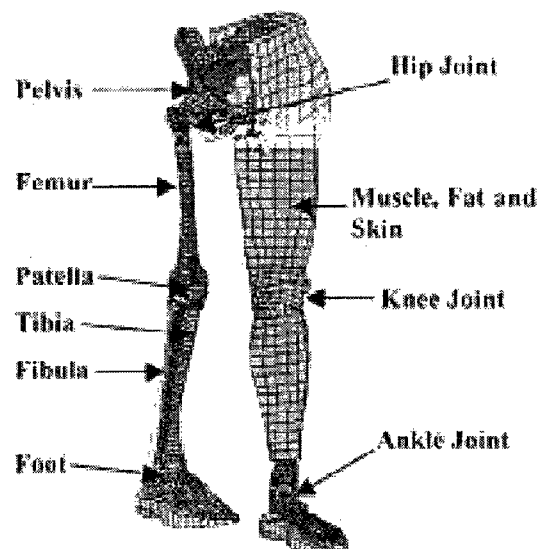


**Figure 13:** The lower extremity of the THUMS model (Maeno & Hasegawa, 2001).

The material properties assigned to the various tissues enable the body segments of the FE model to imitate the mechanical response of human tissue to external loading (Kitagawa et al., 2008). The material properties of the tissues in the model were assigned based on the experimental data published by Yamada (1970). The bones of the model consist of both trabecular and cortical components (Nagasaka et al., 2003), and are similar in shape and strength to real bone (Maeno & Hasegawa, 2001). Bone fracture will occur if the cortical bone of the model experiences plastic strains exceeding 3%; similarly, the knee ligaments of the model will rupture at plastic strains exceeding 11% (Yasuki, 2007).

**Table 4:** Structural details of the AM-50 pedestrian THUMS model.

Number of nodes	60000 <sup>1,3,4</sup>
Number of elements	83500 <sup>1,2,3,4</sup>
Number of material groups	1000 <sup>4</sup>
Number of solid elements	37800 <sup>7</sup>
Number of shell elements	41100 <sup>7</sup>
Number of beam elements	2600 <sup>7</sup>
Number of elements in the lower extremity	9900 per side <sup>7</sup>
Cortical bone	Shell elements <sup>1,4,5,6</sup>
Cancellous bone	Solid elements <sup>1,4,5,6</sup>
Ligaments/tendons	Membrane <sup>4</sup> , shell or beam elements <sup>1,5,6</sup>
Joint surface	Sliding interfaces <sup>1,6</sup>
Achilles tendon	Bar element <sup>4</sup>
Muscles/fat	Solid elements <sup>4,6</sup>
Skin	Shell elements <sup>4</sup> , solid elements <sup>1,6</sup>

<sup>1</sup> Iwamoto et al., 2003; <sup>2</sup> Kang et al., 2005; <sup>3</sup> Kitagawa et al., 2008; <sup>4</sup> Maeno & Hasegawa, 2001; <sup>5</sup> Nagasaka et al., 2003; <sup>6</sup> Oshita et al., 2002; <sup>7</sup> Toyota Central R & D Labs, Inc.

#### 2.6.8.2 Validation of the Total HUMAN Model for Safety

The body segments of THUMS have been validated individually to demonstrate the biofidelity of the model (Kang et al., 2005). Maeno and Hasegawa (2001) and Nagasaka et al. (2003) used isolated lower extremity cadaver specimens to validate the response of the knee joint to lateral impacts, by comparing kinematic measurements from the specimens and the model. Maeno and Hasegawa (2001) further verified the response of a pedestrian to an automobile impact by comparing the kinematics and injury locations

of the model outputs to cadaver tests using full specimens. Previously published results from cadaver tests have also been employed for the validation of THUMS. Oshita et al. (2002) compared force-deflection curves obtained from THUMS to those found in the literature for various impacts experienced by vehicle occupants, while Iwamoto et al. (2003) examined the sites of bone fracture in their model outputs and compared these findings with published results from cadaver tests. In general, the outputs from THUMS have shown an acceptable level of agreement with the results of the various cadaver tests.

#### *2.6.8.3 Limitations of the Total HUMAN Model for Safety*

Although there are many benefits of the THUMS model, including high biofidelity (Maeno & Hasegawa, 2001) and realistic material properties (Yasuki, 2007) and geometries (Kitagawa et al., 2008), some limitations also exist with the model for its application to running-type impacts. For example, the specific height and weight parameters of the AM-50 model are not applicable to the majority of the population. Additionally, the fixed posture of the model, specifically the joint angle at the shoulders, does not replicate the arm postures typically seen during running.

Two of the primary limitations with the THUMS model for this particular application are the minimal soft tissue present around the ankle joint, and the modelling of the muscle tissues with purely passive properties. With respect to the former, the structure that sits inferior to the foot bones of the model has been defined to represent a shoe, as opposed to a heel pad. However, the heel pad has been cited to be responsible for energy dissipation of up to 95% (Pain & Challis, 2001), and has been found to be a more effective shock absorber than a shoe (Kinoshita et al., 1993). Therefore, it would appear that further investigation into the shoe structure of the THUMS model is necessary when considering unshod, running-type impacts.

With respect to the latter limitation, the muscle tissues in the THUMS model are defined using purely passive properties, and active muscle properties have not been incorporated. In automobile impact scenarios, which the THUMS model was developed to simulate, it is assumed that the muscles of the body cannot react quickly enough to generate the force required to protect the joints (Kang et al., 2005; Pope et al., 1979). The passive modelling of muscle tissues allows for altered impact between bones and external surfaces, but does not account for the actions of muscle forces, which primarily function to maintain posture and modify joint and ligament loads (Mukherjee et al., 2007). The incorporation of active muscle properties into a full body model has been shown to substantially affect the predicted stresses in the knee joint, tibia, fibula, and knee ligaments during vehicle-pedestrian impact scenarios (Soni et al., 2009). This effect may be even more pronounced during the simulation of running-type impacts, as some level of muscle activation is necessary prior to the impact, in order to maintain stability and prevent buckling of the joints during the impact.

## 2.7 Literature Review Summary

It is evident from the above review of literature that an extensive body of work has been developed with regards to the examination of the effects of the rigid and soft tissues of the body on its response to impact. The effects of the latter have been further clarified by studies focusing specifically on the active and passive components of the soft tissues. However, to date, no known attempt has been made to use a computational technique such as finite element analysis to evaluate shock propagation through the leg, and to quantify the attenuation of the shock wave along the length of the lower extremity. The use of the THUMS model to examine accelerations at multiple locations along the lower extremity may further advance the body of literature regarding the mechanisms of shock attenuation following impact, and may also contribute to the understanding of mechanisms of injury, especially chronic overuse injuries, in repetitive loading activities such as running.

## *Chapter 3*

### *Methods*

#### 3.1 Objective #1

The first objective of this study was to validate the THUMS model for impact characteristics mimicking those experienced during human locomotion. The validation of the THUMS model consisted of three major components. The first component was an evaluation of the material properties of the THUMS shoe structure (Figure 14, section 3.1.1.1). As minimal soft tissue is incorporated around the ankle and foot of the full body THUMS model, it was necessary to investigate whether the existing soft tissue (developed in the original full body model to imitate a shoe sole) sufficiently represented in vivo human heel pads, with respect to material properties and behaviour. This was accomplished by essentially crushing the shoe of the model between two rigid bodies. The characteristics of the shoe were then altered to better represent those of in vivo human heel pads.

The second component of the validation consisted of an experimental protocol designed to administer running-type impacts to the unshod heel of a human participant using a human pendulum approach (Figure 14, section 3.1.2). The participant was impacted into a vertically mounted force plate at forces of 1.8-2.8 BW and velocities of 1.0-1.15 m/s, which are similar to the impact parameters experienced during running (Cavanagh & Lafortune, 1980). The impact force data collected from the force plate, as well as tibial acceleration data collected from an accelerometer located medial to the tibial tuberosity, were later compared to the equivalent data output of a finite element simulation using the full body THUMS model (see below).

The final component of the validation involved the simulation of a human pendulum impact using the full body THUMS model (Figure 14, section 3.1.3). Modifications were made to the full body model so that its foot impacted a rigid wall at a specified velocity, and impact force and tibial acceleration data were collected from the same locations as in the experimental protocol. These data were then compared to those collected during the experimental human pendulum protocol, in order to determine whether the full body THUMS model was valid for running-type impacts. LS-PREPOST was used for all pre- and post-processing for both the shoe crush and full body impact simulations, and LS-DYNA was used for the processing stage of the analyses.

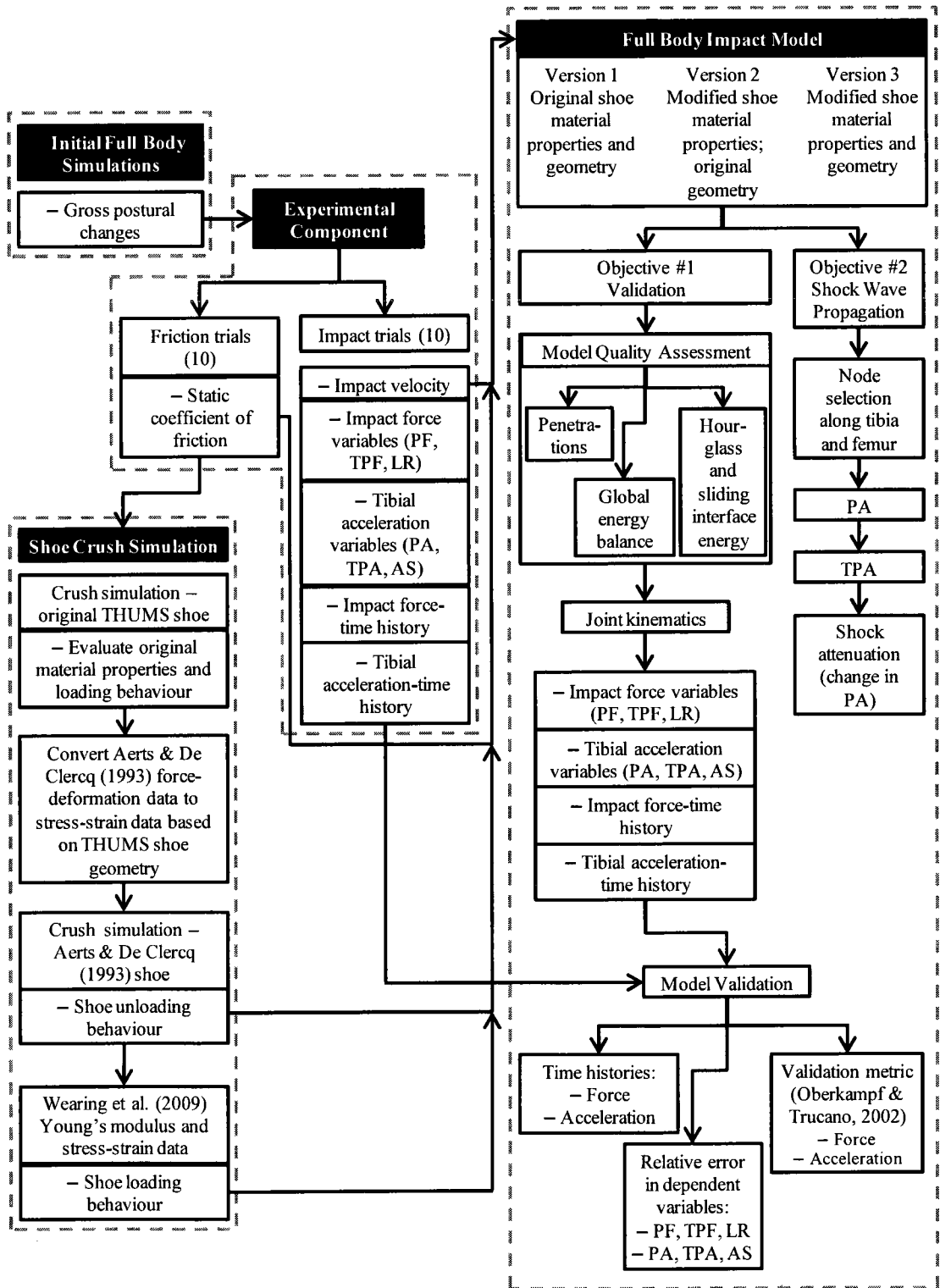


**Figure 14:** Flow chart diagramming the methodology that was followed to address Objectives #1 and #2. The major components of the methodology are grouped by the gray dashed lines.

### ***3.1.1 Initial Model Simulations***

#### ***3.1.1.1 Shoe Crush Simulations***

Before any data were collected experimentally, an examination of the model's shoe structure was completed, in order to ensure that the shoe of the model accurately represented the behaviour of a human heel pad. One limitation of the THUMS model is the sparsity with which the soft tissues around the ankle joint are modelled. As it has previously been determined that the heel pad provides a significant contribution to energy dissipation (Pain & Challis, 2001), it was necessary to evaluate the properties and behaviour of the shoe of the model for comparison to those of the heel pad in vivo. In order to examine the validity of the shoe, compression tests were performed on the shoe structure connected to the inferior aspect of the foot. Every part of the model, with the exception of the left shoe, was deactivated so that only the left shoe remained, and the element formulation of the shoe was modified from its original value of 1 (constant stress solid element) to 2 (fully integrated, selectively reduced solid). An infinite rigid wall was defined just superior to the shoe, and a rigid body was defined just inferior (Figure 15). While it was not necessary to assign geometrical or material properties to the infinite rigid wall, the rigid body was defined as 33 cm long by 15 cm wide, in order to sufficiently cover the inferior surface area of the shoe. The material properties of the rigid body were assigned as follows: mass density of  $2.7E+06 \text{ kg/m}^3$ , Young's modulus of  $8.9E+06 \text{ Pa}$ , and Poisson's ratio of 0.35. As the rigid body should respond rigidly during the crushing of the shoe, these properties were not necessary to define its behaviour during the crush simulation; however, the values assigned to the material properties are required by LS-DYNA to calculate other properties of the rigid body, such as the mass and spring

stiffnesses. In addition, the contact between the shoe and the rigid body was defined through a \*CONTACT\_SURFACE\_TO\_SURFACE algorithm (see Appendix C).

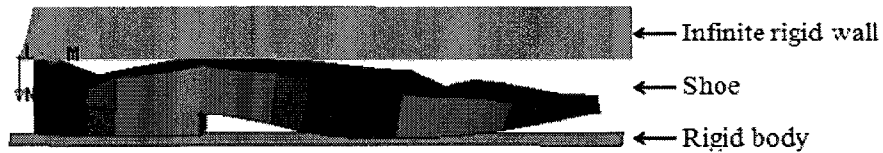


**Figure 15:** The left shoe used in the shoe crush simulations, with the infinite rigid wall and rigid body defined just superior and inferior to the shoe, respectively.

Several techniques were then used to prescribe a biologically accurate stress-strain curve to the shoe structure, by modifying the properties of the original shoe material model, MAT\_LOW\_DENSITY\_FOAM or MAT\_057 (see Appendix C). The force-deformation data from in vivo heel pads (Aerts & De Clercq, 1993) were converted to stress and strain data, based on the cross-sectional area and original thickness of the THUMS shoe. The calculated stress-strain curve was then extrapolated to 80% strain using a cubic spline. This was done because the available in vivo data only represented approximately 21% strain based on the original thickness of the shoe; as the shoe deformed to a greater extent during the full body impact simulation, numerical instabilities would have arisen had the stress-strain curve not been sufficiently defined beyond 21% strain. The modified stress-strain properties and corresponding modulus value were then input into the shoe model in place of the original properties.

Additionally, the thickness of the shoe was altered to create a uniform thickness throughout the shoe (Figure 16). This was done because the original THUMS shoe was developed to mimic the geometry of the inferior aspect of the foot bones, so that the shoe could sit flush against those bones. However, this non-uniform geometry resulted in some wobble during crushing, which was evident in the force-deformation data that were

output from the shoe crush simulation. Therefore, although the uniform shoe thickness could not be replicated in the full body model, this approach was used for the shoe crush simulation. The z-coordinates of the top and bottom layers of nodes of the shoe were altered so that a uniform thickness (approximately 42 mm, corresponding to the widest distance of the original shoe) existed throughout the shoe.

A displacement loading curve was then prescribed to the rigid body inferior to the shoe (Figure 16). The load curve was defined such that the maximum deformation of the shoe was approximately 10 mm, in order to imitate the in vivo heel pad data from Aerts and De Clercq (1993). The maximum displacement of the rigid body occurred at 125 ms, following which it moved back to its original position at 250 ms. Additionally, the hysteretic unloading factor, damping coefficient, and shape factor, which defined the energy absorption behaviour of the shoe during unloading (Turchi et al., 2004), were adjusted from the original values of 0.00, 0.05, and 0.00, respectively, in order to match the in vivo unloading curve (Aerts & De Clercq, 1993).

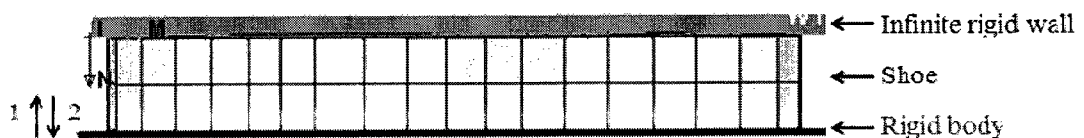


**Figure 16:** Movement of the rigid body inferior to the shoe, as prescribed by the displacement loading curve. 1 = loading phase; 2 = unloading phase.

The above approach was used because it enabled the conversion of force-deformation data (Aerts & De Clercq, 1993) to stress-strain data, and the subsequent comparison of model force-deformation outputs to the original experimental data of Aerts and De Clercq (1993), in order to determine the appropriate coefficients for the unloading behaviour of the shoe, which can only be identified through a trial-and-error approach

(Turchi et al., 2004). This ability to convert between force-deformation and stress-strain data was beneficial, as the experimental studies available in the literature generally have not included both sets of parameters. However, when the calculated stress-strain curve was ultimately transferred into the full body model in the place of the original THUMS stress-strain properties, it was found that the deformation of the modified shoe in response to the imposed impact was too great. It was determined that the stress-strain curve and corresponding modulus value derived from the data of Aerts and De Clercq (1993) represented a stiffness that was far too low to be representative of an in vivo heel pad. To resolve this issue, a search was conducted to find previous literature that had directly presented in vivo heel pad loading data as stress-strain properties, as opposed to force-deformation data. Such a stress-strain curve for in vivo heel pads was presented by Wearing et al. (2009). Although these data were only available up to approximately 40% strain, the curve was extrapolated to 90% strain, so that the loading behaviour of the shoe would be fully defined for the full body impact model. The corresponding Young's modulus value was calculated based on the original curve up to 40% strain, as this region was relatively linear. This stress-strain curve and Young's modulus value, determined from Wearing et al.'s (2009) data, were input into the full body impact model to define the loading behaviour of the shoe, along with the coefficients determined from Aerts and De Clercq's (1993) data to define the unloading behaviour.

### *3.1.1.2 Initial Full Body Impact Simulations*

Initial simulations were conducted with the full body THUMS model to investigate the gross postural behaviour of the model in response to a human pendulum-type impact, in order to mimic the model's postures during the experimental component. The orientation of the model was altered from an upright standing to a supine position, to

replicate the orientation of the participant during the experimental trials on the pendulum (Figure 17). A rigid wall was defined adjacent to the right heel of the model, in order to simulate the impact surface in the laboratory. The rigid wall was oriented vertically, such that it was perpendicular to the longitudinal axis of the left lower extremity. During the simulation, the wall acted as the force plate used in the experimental procedure (see section 3.1.2), and responded rigidly when it was impacted by the left foot. However, the right foot was able to pass through the wall, which mimicked the experimental conditions in that the right foot did not impact the force plate. The initial velocity and friction coefficient between the foot and the rigid wall were specified as 1.0 m/s in the global z-axis (Figure 17) and 0.3, respectively. A velocity of 1.0 m/s is typical for a running-type impact (Lafortune et al., 1996a), while 0.3 has been specified as a friction coefficient between the foot and an impact surface in previous modelling studies (Chang et al., 2008; Pain & Challis, 2001). Finally, the termination time for the simulation was defined as 100 ms, as the two main peaks in both the force and acceleration waveforms occurred within this time frame for both the experimental and model data. Additionally, by 100 ms, both the force- and acceleration-time profiles produced by the model had either returned to, or were close to returning to, a steady state condition.

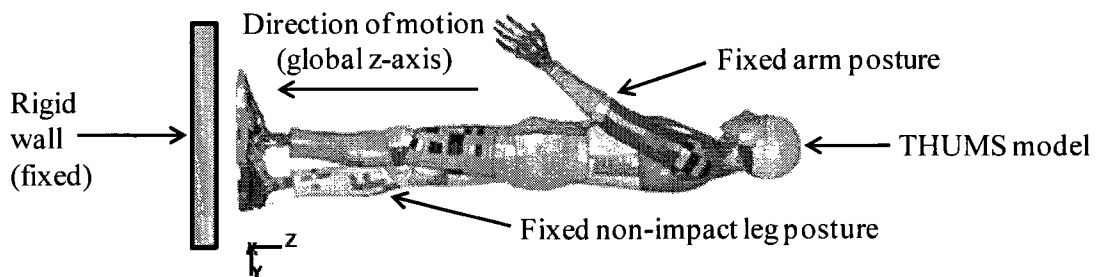


**Figure 17:** Modifications to the THUMS model: horizontal orientation and rigid wall. The initial velocity input was assigned, and the impact force output measured, with respect to the global z-axis.

The initial simulations indicated that the ankle joint of the full body model maintained a relatively constant angle of approximately 90° of flexion, and the knee joint maintained an extended position throughout the impact. These parameters were taken into consideration when positioning the participant during the experimental impact trials.

### ***3.1.2 Experimental Component***

#### ***3.1.2.1 Participants***

One participant was recruited for the validation of the THUMS model, who was similar in height (1.72 m) and body mass (76.4 kg) to that of the 50<sup>th</sup> percentile American male model (1.78 m, 78.2 kg). The participant was recruited from the University of Windsor student population, and had not experienced any injuries to the back or lower extremities within the last 12 months. All experimental procedures were approved by the University of Windsor Research Ethics Board.

#### ***3.1.2.2 Pendulum and Impact Apparatus***

A human pendulum constructed using a rectangular steel frame (190.5 cm x 52.5 cm) and canvas bed was suspended from the ceiling using four steel cables (Duquette & Andrews, 2010a, b; Flynn et al., 2004; Holmes & Andrews, 2006; Schinkel-Ivy et al., 2010). The total mass of the pendulum and suspension system was 13 kg. The participant was positioned supine on the pendulum with the left leg in full extension, with the left foot just touching the impact apparatus and the joint line of the left knee situated at the leading edge of the pendulum (Figure 18). The right leg was also extended, but abducted enough so that the right foot did not contact the force plate. The impact apparatus was composed of a steel grid rigidly anchored to the laboratory wall and floor. This experimental methodology has been used previously by various authors (Duquette & Andrews, 2010a, b; Flynn et al., 2004; Holmes & Andrews, 2006; Lafortune & Lake,

1995; Lafortune et al., 1996a, b; Schinkel-Ivy et al., 2010) in order to administer impacts to the foot that are similar in magnitude and timing to those experienced during running (Cavanagh & Lafortune, 1980). The human pendulum approach is also advantageous in that it enables a maximal level of control with respect to initial impact conditions (for example, force and velocity) (Lafortune & Lake, 1995).

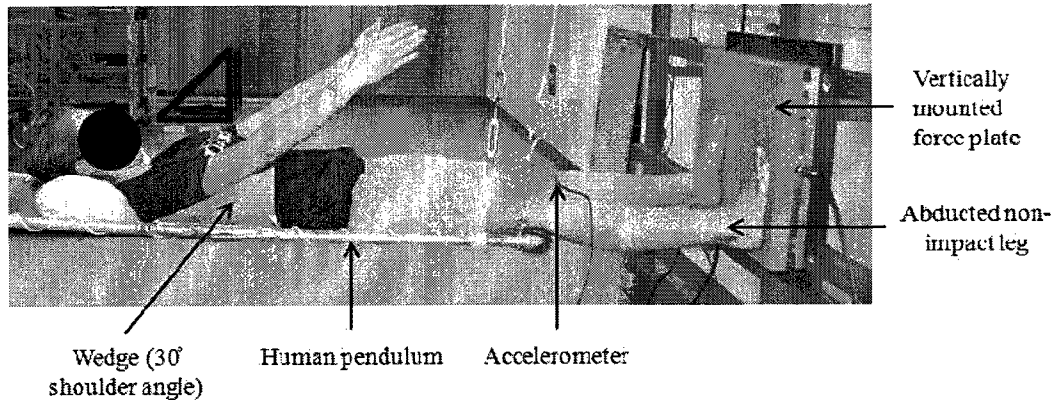


**Figure 18:** The human pendulum, impact apparatus, and participant positioning.

### 3.1.2.3 Instrumentation

A force plate (AMTI-OR6-6-1000, A-Tech Instruments Ltd., Scarborough, ON, Canada, natural frequency of 1000 Hz) was rigidly anchored to a 1.8 cm thick steel plate which was bolted to the impact apparatus, while a velocity transducer (Celesco DV301, Don Mills, ON, Canada) was attached to the trailing end of the pendulum, enabling the simultaneous measurement of force and velocity parameters, respectively, throughout the duration of the impact. These instruments were used to ensure that the force and velocity at impact fell within the desirable range that has been used previously in the literature; specifically, a range of 1.8-2.8 BW and 1.0-1.15 m/s for force and velocity, respectively (Cavanagh & Lafortune, 1980; Duquette & Andrews, 2010a, b; Flynn et al., 2004; Holmes & Andrews, 2006; Schinkel-Ivy et al., 2010). Additionally, the force plate

allowed for the determination of three dependent impact force variables (Figure 19): peak force (PF), time to peak force (TPF), and loading rate (LR), which was measured as the slope of the curve between 20% and 80% of the peak impact force (Boyer & Nigg, 2006; Milner et al., 2006; Williams et al., 2001b, 2004). Force plate data were filtered using a dual-pass Butterworth low pass filter with a cutoff frequency of 70 Hz, as determined by residual analysis (Winter, 2005).

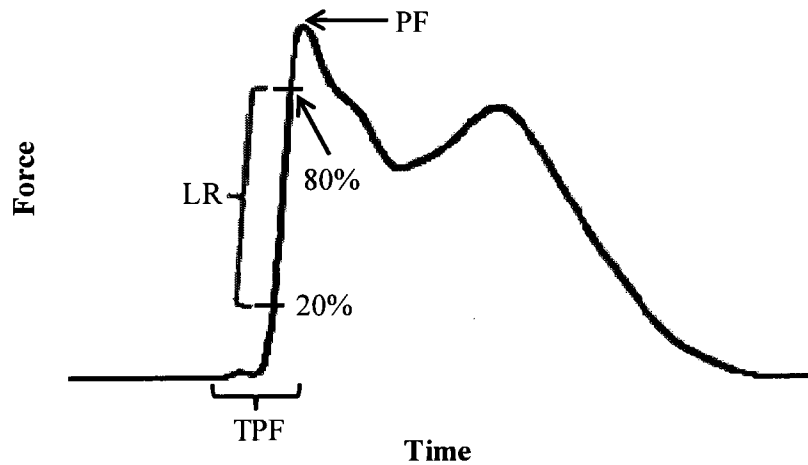


**Figure 19:** Schematic diagram of a force waveform from a human pendulum impact, showing how the dependent impact force variables were determined. PF = peak force; TPF = time to peak force; LR = loading rate.

An accelerometer (MMA3201D, Freescale Semiconductor, Inc., Ottawa, ON, Canada; range of +/- 50 g) was mounted to the surface of the skin of the participant's shank, 3.5 cm medial to the tibial tuberosity (Figure 20). The sensitive axis of the accelerometer was aligned with the longitudinal axis of the tibia and secured to the skin using double-sided tape. The accelerometer was preloaded with approximately 45 N, using an elastic Velcro™ strap. This technique has been used by authors such as Andrews and Dowling (2000), Hamill et al. (1995), and Mizrahi et al. (2000) for the quantification of shock wave propagation in vivo, as it reduces the influence of soft tissue

motion on the acceleration signal, thereby providing a more accurate representation of bone accelerations without being invasive. The accelerometer was used to monitor the acceleration response of the proximal tibia, in order to track the acceleration waveform and determine three dependent tibial acceleration variables (Figure 21): peak acceleration (PA), time to peak acceleration (TPA), and acceleration slope (AS), which was measured as the slope of the curve between 30% and 70% of the peak acceleration (Duquette & Andrews, 2010a; Flynn et al., 2004; Holmes & Andrews, 2006). Accelerometer signals were filtered close to the source with a fourth order Bessel switched capacitor low pass filter with a cut-off frequency of 1.5 Hz, inherent in the design of the accelerometer.

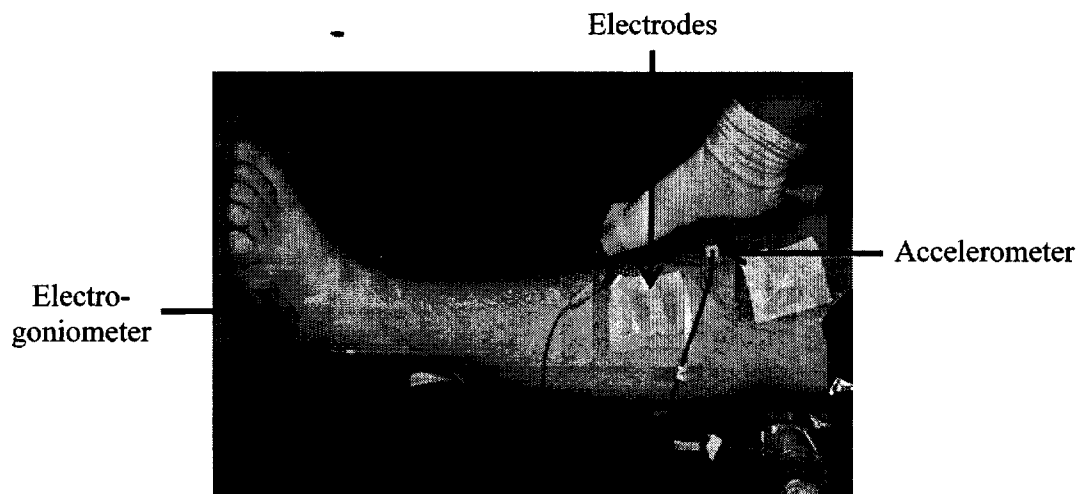


**Figure 20:** Participant's leg instrumented with electrodes, accelerometer, and electrogoniometer.

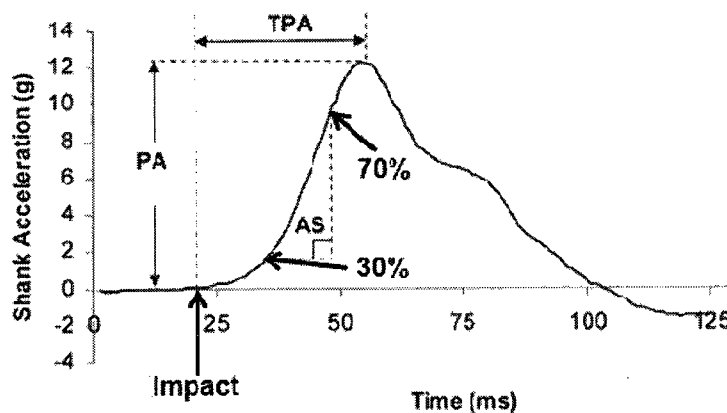


**Figure 21:** Schematic diagram of a typical acceleration waveform from a human pendulum impact, showing how the dependent tibial acceleration variables were determined. PA = peak acceleration; TPA = time to peak acceleration; AS = acceleration slope (Adapted from Holmes & Andrews, 2006).

Bipolar disposable Ag/Ag-Cl surface electrodes (ES40076 Kendall, Mansfield, MA) were used to monitor the activation levels of the tibialis anterior (TA) and lateral gastrocnemius (LG). Following shaving and cleaning of the skin with rubbing alcohol, two electrodes were placed over the belly of each muscle, with an inter-electrode spacing of 2 cm (Figure 20). Electromyographic data for both muscles were full-wave rectified and filtered using a second order dual pass Butterworth filter with a cut-off frequency of 1.5 Hz. Data were then normalized to the maximum voluntary exertion (MVE) that the participant was able to produce for each muscle (see section 3.1.2.4). During the experimental impact trials, the participant was provided with real-time visual feedback regarding the activation of the TA and LG on a computer monitor positioned in their line of sight, and was asked to maintain a constant activation level throughout the duration of the impact (see section 3.1.2.4).

Finally, an electrogoniometer (Biometrics SG110, Biometrics Ltd., Gwent, U.K.) was secured to the skin on either side of the ankle joint, on the lateral aspect of the foot and the distal fibula superior to the lateral malleolus, to monitor the angle of the ankle

joint at impact (Figure 20). The participant was provided with real-time visual feedback regarding their ankle angle on a computer monitor positioned in their line of sight, and was asked to maintain an angle of approximately 90° of ankle flexion throughout the impact, to remain consistent with that of the THUMS model.

#### *3.1.2.4 Procedures*

Following the instrumentation of the participant with EMG electrodes, a maximum voluntary exertion (MVE) protocol was performed for the TA and LG. To elicit the LG MVE, the participant stood with their arms crossed over the chest on a wooden platform, with 5 cm wide nylon straps secured over the shoulders. The participant then performed calf raises against the resistance provided by the straps. The TA MVE was elicited by asking the participant to dorsiflex through a range of motion at the ankle against manual resistance provided by an investigator, while lying supine on the pendulum. The participant performed three trials for each protocol, with each trial lasting 5 seconds, and adequate rest between trials to minimize fatigue. The maximum EMG amplitude from the three trials was used as the MVE for each muscle.

The participant was then instrumented with the accelerometer and electrogoniometer, and secured to the pendulum using two 5 cm wide nylon straps placed across the pelvis and the distal thigh of the left leg. The participant then performed three 5-second trials during which he was asked to maintain an ankle angle of approximately 90° of flexion using the visual feedback provided. The level of activation required for the participant to maintain 90° of flexion was set as the target activation level for the TA, which the participant was asked to maintain during the subsequent impact trials. Additionally, wedges were constructed out of a double layer of corrugated cardboard and secured to the pendulum frame at the level of the shoulder using duct tape (Figure 18).

This provided a guide for the participant to maintain a shoulder angle of 30° relative to the horizontal, in order to match the position of the upper extremities of the full body THUMS model.

Several practice trials were then performed, to familiarize the participant with the procedure and to determine the appropriate distance from which the pendulum should be released. The pendulum was pulled back approximately 70 cm, in order to administer an impact force of 1.8-2.8 BW and an impact velocity of 1.0-1.15 m/s; these parameters are similar to those experienced during running (Cavanagh & LaFortune, 1980). Once the appropriate pull-back distance was determined, the participant performed ten experimental trials with consistent force, velocity, muscle activation, and ankle angle parameters.

Additionally, a protocol was developed to determine the coefficient of friction between the force plate and the heel of the participant, as this value was required as an input for the contact definition between the rigid wall and shoe in the full body THUMS model. The participant sat in a chair positioned adjacent to the edge of a force plate that sat flush with the floor (AMTI-OR6-6-1000, A-Tech Instruments Ltd., Scarborough, ON, Canada, natural frequency of 1000 Hz) with the left knee and ankle joints positioned at 90° of flexion so that the left foot rested on the force plate (Figure 22). The right leg was positioned off to the side so that it did not impose any additional load on the force plate. The left thigh, which was positioned parallel to the floor, was weighted with an 11 kg bag of lead shot, which was strapped securely in place. A 3-cm wide strap was looped around the left calcaneus, which was pulled forward by an investigator using a constant force so that the foot slid anteriorly across the force plate. Vertical and anterior-posterior (A-P) forces were collected from the force plate. The peak of the A-P forces was assumed to be

the instant at which the foot moved; therefore, the static coefficient of friction was calculated using the A-P and vertical forces at that instant (Figure 23).

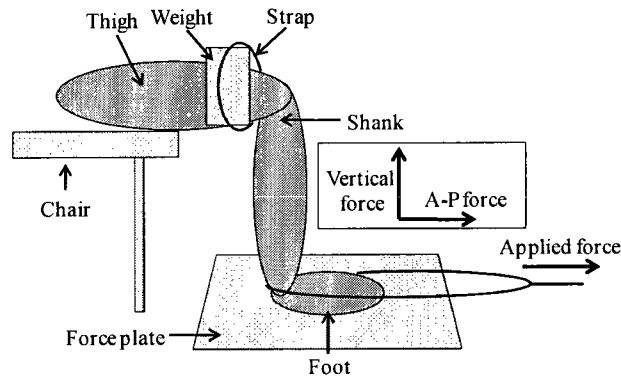


**Figure 22:** Schematic showing the set up of the heel pad friction protocol.

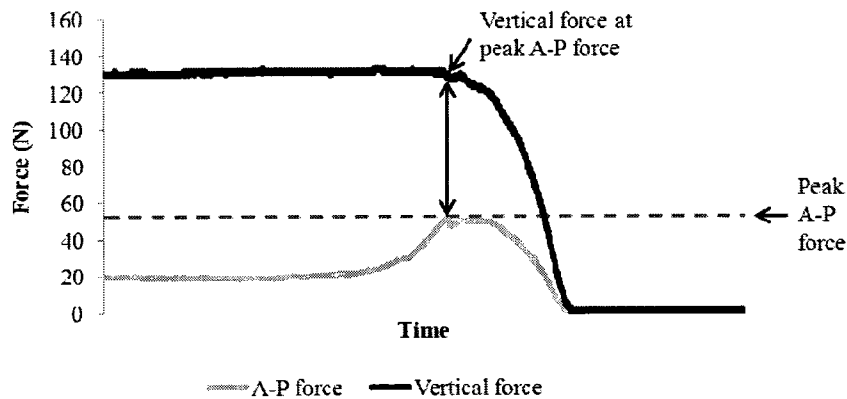


**Figure 23:** Sample graph of vertical and A-P forces from a friction trial, showing how the static coefficient of friction was determined.

The mean impact velocity from the experimental impact trials, as well as the experimentally determined coefficient of friction between the force plate and heel from the friction trials, were used as the inputs for the full body THUMS model. The experimental force and acceleration profiles, as measured at the force plate and medial to the tibial tuberosity, respectively, were compared to the equivalent outputs from the THUMS model for validation purposes.

### *3.1.2.5 Data Acquisition*

For the impact trials, data collection from the force plate, velocity transducer, accelerometer, electrodes, and electrogoniometer was initiated manually by the investigator, following an auditory queue which signalled that the pendulum could be released. All data were collected simultaneously using a custom LabVIEW software program (National Instruments, Austin, TX, USA, version 9) for 2 seconds. For the friction trials, data collection from the force plate was manually initiated by an investigator, and data were collected for 5 seconds using another custom LabVIEW software program. All data were A/D converted using a 12-bit card (ADI-32, A-Tech Instruments Ltd., Scarborough, ON, Canada) and sampled at a rate of 4096 Hz.

### *3.1.3 Full Body Impact Simulations*

As previously described, the characteristics of the full body THUMS model were initially modified in order to mimic the impact conditions experienced using the human pendulum (Figure 17). Following the experimental data collection, additional modifications were also made to the model to better replicate the experimental conditions. The nodes of the left foot and shank were fully constrained to the rigid wall using a node set assigned to the wall. This was done to ensure that the nodes of the left foot would not penetrate the rigid wall. The initial velocity in the global z-axis (1.0622 m/s) and friction coefficient (0.401355) for the foot-wall contact were modified from 1.0 m/s and 0.3, respectively, to replicate the mean parameters found during the experimental phase of the study. In addition, the element formulation of the left shoe was modified from 1 to 2.

Further, an iterative procedure was used to determine a combination of modifications to the full body model which would enable the simulation to run to its full completion time (see Appendix D). The \*HOURGLASS command, with an hourglass

coefficient of 0.1, was employed to minimize hourglassing of all elements within the full body model (see section 3.1.3.3). Upon viewing the initial full body simulation, it was evident that there were issues in the contact algorithms of certain parts of the upper body (i.e. penetrations and unrealistic wobbling in the shoulders). These issues caused the simulation to terminate due to numerical instabilities (negative element volumes) before it had reached its full completion time. Therefore, modifications were made to the soft constraint option and its scale factor, as well as the scale factors for default penalty stiffnesses, for relevant contact algorithms in the upper body. Additionally, the penalty scale factor, activation factor, and formulation for interior contact under the \*CONTACT\_INTERIOR algorithm were modified for specific soft tissue parts in the upper body. All altered coefficients were associated with algorithms for contacts in the upper arms, shoulders, and thorax; all coefficients within the left lower extremity contact algorithms were left as the original values. Once a series of contact modifications were made that allowed for a relatively stable model for this type of impact, three versions of the model were solved using LS-DYNA (Table 5).

**Table 5: Modifications to each version of the full body impact model.**

Modifications	Version #
Initial velocity = 1.0622 m/s (determined experimentally)	1, 2, 3
Friction coefficient = 0.401355 (determined experimentally)	1, 2, 3
Increased density for parts 8400210 and 8400220 (torso)	2, 3
Material properties of left (impacting) shoe modified to those of a biological heel pad	2, 3
Bottom layer of nodes removed from the heel of the shoe	3
Thickness of shoe reduced from 28 mm to 18 mm at its centre	3

Version 1 was relatively unaltered from the original Toyota full body THUMS model, with the exceptions listed in Appendix D. The original material properties and geometries for the left (impacting) shoe were left intact, as was the density of the torso.

In version 2, the densities of parts 8400210 and 8400220 (parts located bilaterally in the torso) were increased to alter the total mass of the full body THUMS model from 78 kg to 90 kg, to account for the mass of the pendulum (13 kg) in the experimental setup. Additionally, the material properties of the left (impacting) shoe were modified to better represent those of an in vivo human heel pad (see section 3.1.1.1). A stress-strain curve was assigned to the left shoe, which defined the behaviour of the shoe in response to compression. The heel pad stress-strain curve presented by Wearing et al. (2009) was used to define the shoe's behaviour up to 40% strain; the curve was then extrapolated to 90% strain, in order to provide adequate input for the model. The modulus value for the heel pad was also determined from the data presented by Wearing et al. (2009). Further, the coefficients defining the shoe's unloading behaviour, determined in section 3.1.1.1, were also input into the material model for the shoe.

Once the material properties of the shoe more closely resembled those from human experimental data, version 3 was used to alter the geometry and thickness of the shoe. The bottom layer of nodes that were defined at the heel of the shoe was removed as an initial attempt to alter the geometry to make the structure more similar to a heel pad, as opposed to a shoe. Additionally, the z-coordinates of the bottom layer of nodes were altered to give a shoe thickness of approximately 18 mm at the centre of the heel, which is similar to the thickness of a human heel pad (Gefen et al., 2001).

#### *3.1.3.1 Penetrations*

Before comparing the full body model impact force and tibial acceleration outputs to the experimental data, a preliminary analysis was required for each version of the model, to ensure that there were no major inconsistencies between the behaviour of the model and that of the experimental participant. The joints of the left lower extremity

were visually monitored through the time history of the simulation, to ensure that no penetrations were occurring at any of the joints.

### *3.1.3.2 Global Energy Balance*

The energy balance of the model was also examined, specifically the global kinetic, internal, and total energies. The kinetic energy of an object represents the energy that the object possesses as a result of its motion, while internal energy constitutes the strain energy associated with beam, shell, and solid elements, as well as the deformation energy associated with spring or damper element types. Total energy is calculated globally as the sum of the internal, kinetic, sliding, hourglass (see section 3.1.3.3), system damping, and rigid wall energies. Ideally, the total energy should be equal to the sum of the kinetic and internal energies. Due to the overall complexity and nonlinearity of the full body impact model (for example, non-linear material properties, complex geometries (Maeno & Hasegawa, 2001; Yasuki, 2007), and numerous contact algorithms), it was necessary to evaluate the energy balance of the full body model in order to determine whether there were any major inconsistencies in energy, and to ensure the overall quality of the full body model. To this end, the global kinetic, internal, and total energies were plotted in LS-PREPOST to evaluate the energy balance of the full body model.

### *3.1.3.3 Hourglass Energy and Sliding Interface Energy*

When a finite element mesh is disturbed (for example, through impact with another body), hourglass-shaped deformations may occur within the elements of the model without any formation of strain energy. The term ‘hourglassing’ is used to describe these hourglass-shaped element deformations, and is also referred to as a non-physical, zero energy mode of deformation. This is generally considered undesirable when examining the energy balance of a finite element model, as deformations resulting

in zero strain and no stress are not physically possible. Therefore, the \*HOURGLASS command was implemented to minimize hourglassing of the elements in the full body model. Hourglassing is controlled in LS-DYNA by adding loads to nodes within the model, which prevents these types of deformations, and also increases the stiffness of the system. For each version of the full body model, the global hourglass energy (HGE) and material HGE (HGE associated with each part in the model) were plotted in LS-PREPOST to identify the parts that contributed substantially to the global HGE (any part with an HGE of greater than 25.0 J was used as an initial criterion). As the specific focus of the present study was the left lower extremity, this process was used to determine whether there was any significant hourglassing of elements within the region of interest (left foot, ankle, shank, knee, and thigh).

In addition, the sliding interface energy (SLE), which represents the energy associated with friction in contact, was also investigated for all contact algorithms within each version of the model. Negative sliding interface energy values are undesirable, as they are indicative of penetrations occurring between the parts represented by a contact algorithm. For each version of the full body model, LS-PREPOST was used to plot the global SLE, as well as the SLE associated with each individual contact algorithm, in order to identify the contact algorithms with the greatest contributions to the global SLE. Similar to the analysis of the model hourglass energies, this process was used to determine whether there were any issues with contact algorithms in the region of interest (left foot, ankle, shank, knee, and thigh).

#### *3.1.3.4 Joint Kinematics*

The preliminary analysis also included a quantification of changes in joint angles for the left lower extremity. Changes in ankle and knee angles in the frontal and sagittal

planes were tracked using LS-PREPOST, to determine both the maximum and net changes that occurred (Figure 24). Additionally, as elevation of the left side of the pelvis was observed visually during the initial simulations, the heights of the iliac crests were tracked and compared bilaterally.

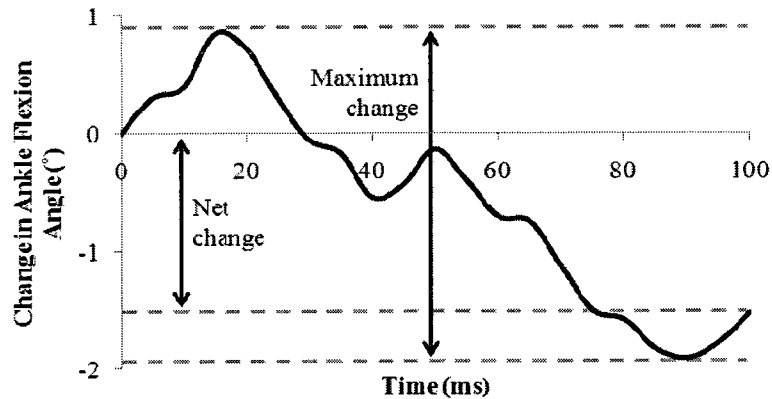


**Figure 24:** Change in ankle angle in the sagittal plane over the course of a simulation, indicating how the maximum and net changes in angle were determined.

### 3.1.3.5 Model Dependent Variables

Force and acceleration profiles were collected from the same relative locations on the model as were used in the experimental trials. The force data were collected from the rigid wall output with respect to the global z-axis (Figure 17). One node on the outer surface of the soft tissue of the shank was included in the nodal data output file to track the tibial accelerations. The specific node (node ID #8282183) was selected based on the location of the accelerometer in the experimental protocol. To determine the location at which the acceleration data were collected on the model, the length of the participant's shank from the inferior aspect of the medial malleolus to the medial aspect of the tibial plateau (Burkhart et al., 2008) was measured. Subsequently, the distance between the participant's medial malleolus and the level of the accelerometer was measured and expressed as a percentage of shank length. Finally, the medio-lateral distance between

the medial shank line and the accelerometer was also measured. These measurements were then used to determine the appropriate location of the accelerometer node on the full body THUMS model (Figure 25).

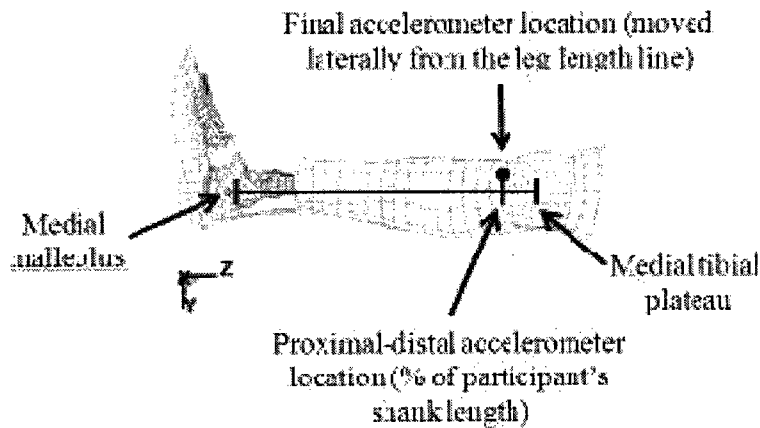


**Figure 25:** Location at which acceleration data were collected on the full body model.

For the validation phase, the model force output was sampled at 4096 Hz and filtered with a dual-pass Butterworth low pass filter with a channel frequency class of 600 Hz as recommended for femur, knee, tibial, and ankle forces during impact testing by the SAE J211 standards (SAE, 2003). Acceleration data were obtained from the model at the accelerometer location. As the default in LS-DYNA is to output the accelerations in the global x-y-z coordinate system, a local coordinate system was defined along the length of the tibia (Figure 26). This local coordinate system was then assigned to the accelerometer node at the proximal tibia (node ID #8282183), so that the acceleration at that node would be calculated with respect to the local, as opposed to the global, coordinate system. Specifically, the acceleration that occurred relative to the x-axis of the local coordinate system (parallel to the longitudinal axis of the tibia) at the accelerometer node was employed for comparison to the experimental acceleration data, as the acceleration was measured along the same axis during the experimental protocol. The accelerations were

sampled at 4096 Hz and filtered with a dual-pass Butterworth low pass filter with a channel frequency class of 108 Hz. Because accelerations are determined in LS-DYNA by the differentiation of velocity data through a central difference scheme, the raw acceleration data contained a substantial amount of high frequency noise; thus a channel frequency class of 108 Hz was necessary to obtain relatively smooth curves for comparison to the experimental data. The force- and acceleration-time histories were used to determine the impact force variables (peak force, time to peak force, and loading rate) and tibial acceleration variables (peak acceleration, time to peak acceleration, and acceleration slope).

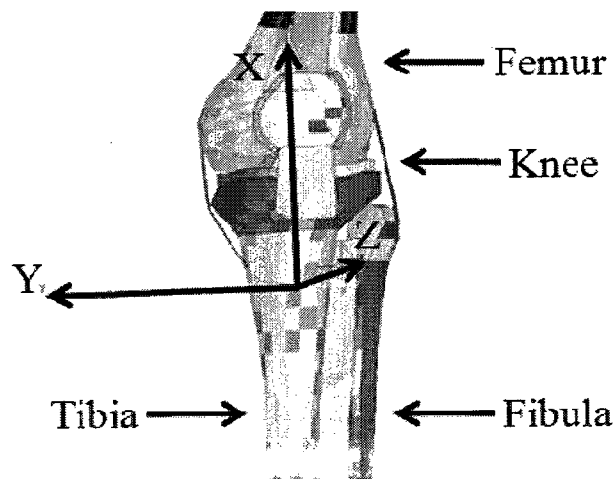


**Figure 26:** Local coordinate system defined for the tibia. The x-axis was defined parallel to the longitudinal axis of the tibia, and the y- and z- axes were subsequently defined in the plane perpendicular to the x-axis.

### 3.1.4 Model Validation

#### 3.1.4.1 Force- and Acceleration-Time Histories

Several steps were employed for the comparison of the experimental and model force and acceleration outputs. To qualitatively evaluate the fit of the model force and acceleration profiles with those of the experimental data, the force and acceleration data

from the experimental trials were averaged to obtain a mean 200- and 220 ms event for the force and acceleration profiles, respectively. The difference in the lengths of the force and acceleration events is due to the effects of soft tissues on the acceleration profile. The acceleration profile required a relatively longer time to return to the baseline condition due to wobble in the soft tissues, thereby necessitating a longer duration to encompass the event. The regions bounded by one and two standard deviations on either side of the curve were also calculated. The model force and acceleration profiles were then superimposed onto the mean experimental curves. A similar procedure was used by Wright et al. (1998) to compare experimental and model force profiles (Figure 27).

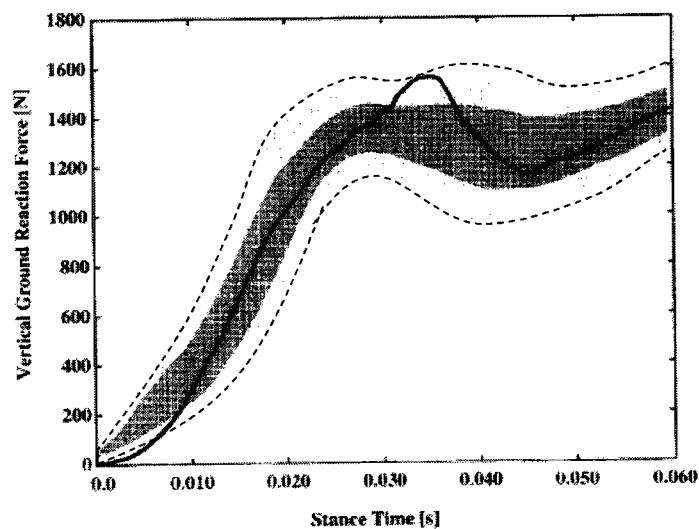


**Figure 27:** A comparison of the force profiles from a simulation (solid line) and 10 experimental trials (dark shaded region bounds one standard deviation, dashed line bounds approximately two standard deviations) (Adapted from Wright et al., 1998).

From an initial qualitative examination of the experimental and full body model impact force and tibial acceleration profiles, it was observed that a toe region existed at the beginning of the experimental profiles, of approximately 25.0 ms for the impact force and 24.2 ms for the tibial acceleration. This toe region did not exist in the profiles from

the full body model, resulting in a delay in time between the model and experimental profiles; however, qualitative observation indicated that when a phase shift was performed on the model waveforms, the shapes of the model impact force and tibial acceleration waveforms approximated those of the experimental counterparts.

Therefore, for the comparison of the impact force waveforms, the model impact force data were lined up at both  $t=0$  ms and at the end of the toe region, approximately  $t=25$  ms (Figure 28). Similarly, the model tibial acceleration waveforms were compared to the experimental data when lined up at  $t=0$  ms, and with the experimental and model peak accelerations lined up (approximately  $t=30$  ms). The best possible attempt was made to ensure that the model time histories were synchronized to the appropriate location in the experimental time histories. This approach of assessing the force and acceleration curves lined up at two different times in the experimental data was also employed for the other two metrics employed during the validation phase of the current study (see sections 3.1.4.2 and 3.1.4.3). This approach was employed simply to demonstrate that although the impact force and tibial acceleration waveforms produced by the full body model may not account for the toe region measured experimentally, the model was able to replicate other features of the experimental data relatively well. However, it was acknowledged that these artificial alterations of the model waveforms did not account for the fact that the model does not replicate the toe region, and that further work may be necessary to improve the agreement between the experimental and model waveforms in terms of the timing of both impact forces and tibial accelerations.

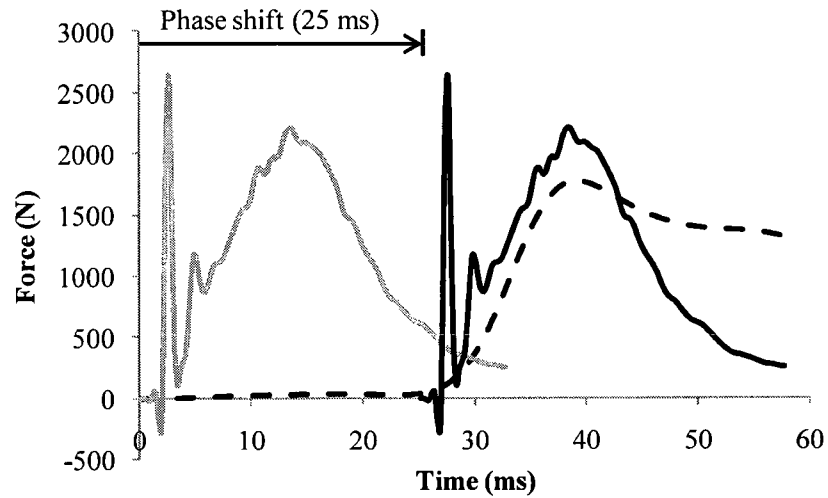


**Figure 28:** Example of the superimposed experimental and model impact force profiles with a phase shift in the model profile (dashed black line = mean experimental profile; solid gray and black lines = model data lined up at  $t=0$  ms and  $t=25$  ms, respectively).

#### 3.1.4.2 Relative Error in Dependent Variables

The impact force variables and tibial acceleration variables were then compared between the experimental and model data. The mean and standard deviation for the ten experimental trials were computed for each of the variables, which were then used to determine the relative (percent) error between the experimental and model data using Equation 3:

$$\% \text{ error} = \left( \frac{X(\text{model}) - X(\text{experimental})}{X(\text{experimental})} \right) \times 100 \quad [3]$$

where 'X' represents an impact force or tibial acceleration variable. Additionally, PF, TPF, PA, and TPA were also evaluated for the second peak that was observed in both the force and acceleration profiles in the experimental and model data.

#### 3.1.4.3 Validation Metric

Finally, the agreement between the experimental and model force and acceleration profiles were assessed over the entire 100 ms time interval using a technique proposed by

Oberkampff and Trucano (2002). Their validation metric for discrete data is calculated using Equation 4:

$$V = 1 - \frac{1}{n} \sum_{i=1}^{i=n} \tanh \left| \frac{y(x_i) - Y(x_i)}{Y(x_i)} \right| \quad [4]$$

where ‘V’ represents the validation metric, ‘n’ represents the number of samples, ‘tanh’ represents the hyperbolic tangent trigonometric function, ‘y’ represents the model data, and ‘Y’ represents the experimental data. The absolute value of the relative error between the model and experimental data was calculated and summed across the entire time interval, then normalized to the number of samples and subtracted from one. In addition to the calculation of a relative error measure, this validation metric has several other advantages: as the absolute value of the relative error is taken, the difference between the experimental and model data can only increase; when no difference exists at any location between the two sets of data, the validation metric is equal to one; and when large differences exist between experimental and model data, the validation metric approaches zero (Jin et al., 2010) (Figure 29).

The validation metric was calculated between the mean experimental and model results across the entire time interval for the force and acceleration data for each version of the model. As the experimental data points acted as the denominator for the relative error equation, when the data approached 0, the relative error approached infinity. Therefore, a region of 5% of the absolute maximum value of the experimental data was set as a boundary around 0, and these data points were discounted during the calculation of the validation metric.

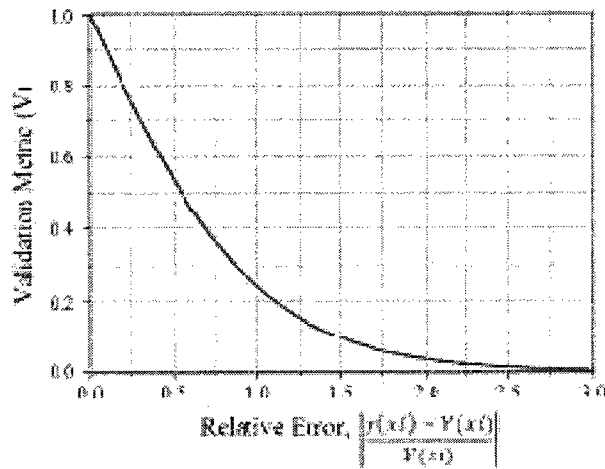


**Figure 29:** The validation metric (V) as a function of the relative error (Adapted from Jin et al., 2010).

### 3.2 Objective #2

Once the validation of the THUMS model for running-type impacts was addressed, the accelerations were examined at eleven locations along the lower extremity for each version of the model. The local coordinate system for the tibia described in Objective #1 was also employed for Objective #2 (Figure 26); an additional coordinate system was defined in the same manner for the femur (Figure 30).

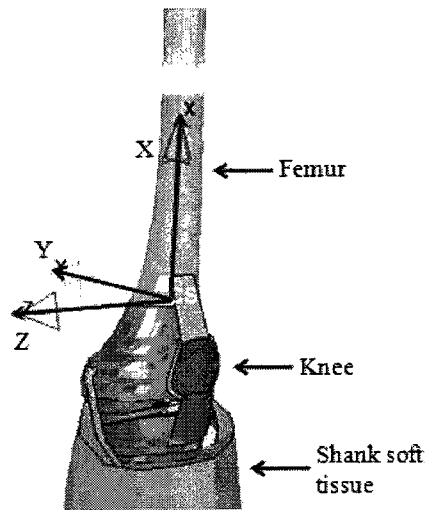


**Figure 30:** Local coordinate system defined for the femur. The x-axis was defined parallel to the longitudinal axis of the femur.

Accelerations occurring on the bony surfaces of the lower extremity were examined along the antero-medial aspect of talus, tibia, and femur, in order to remain in line with the original accelerometer node selected in Objective #1. Accelerations were tracked in the x-axis of the local tibial coordinate system for one node on the talus and six nodes along the length of the tibia. In addition, accelerations were tracked in the x-axis of the local femoral coordinate system for four nodes along the length of the femur (Figure 31). Although the femur of the full body model was longer than the tibia by approximately 7 cm, fewer nodes were tracked along the femur due to the positioning of the pelvic soft tissue, which would have interfered with any nodes more proximal than node ID #8250753. The talar node and most distal tibial node were separated by 3.3 cm. The tibial nodes spanned a distance of approximately 29 cm and were spaced 7-8 cm apart, with the exception of the two most distal nodes, which were separated by 2.6 cm. The talar node and most distal tibial node were selected in order to examine attenuation across the ankle joint, while the remaining tibial nodes were spaced evenly in order to provide a representation of shock attenuation between regions of similar length. Similarly, the femoral nodes spanned a distance of 21 cm, and were spaced approximately 7 cm apart. Approximately 13 cm separated the most proximal tibial and most distal femoral nodes (i.e. those spanning the knee joint).

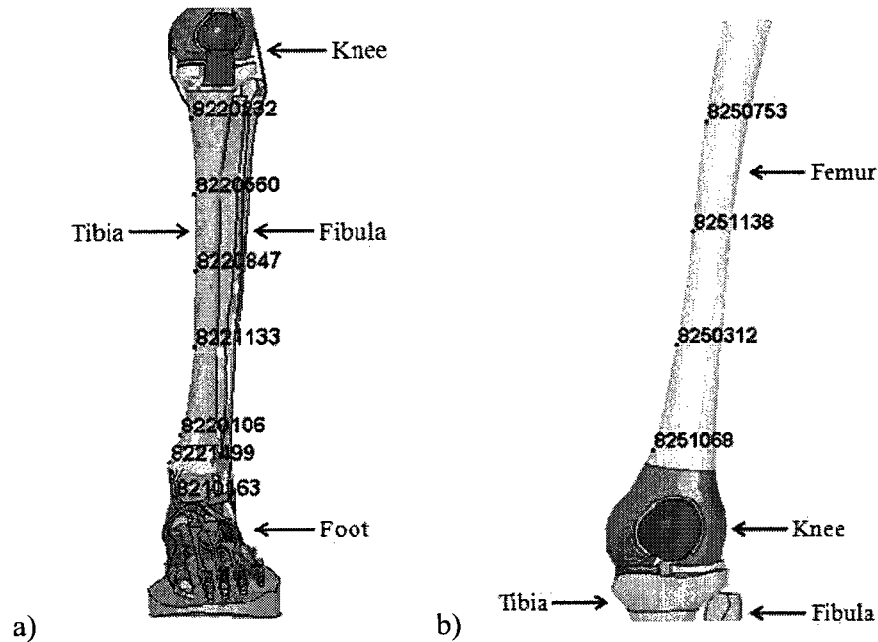


**Figure 31:** Selected nodes for acceleration measurements along the a) ankle and tibia; b) femur. The seven-digit numbers represent node ID numbers in the finite element code.

The accelerations were sampled at 2.4 MHz, in order to capture an adequate number of samples during the time period that the shock wave was travelling along the bones. The data were then filtered with a dual-pass Butterworth low pass filter with a channel frequency class of 180 Hz. The PA and TPA for each of the curves were then determined. The TPA values were used to determine whether the times at which peak accelerations occurred were delayed between subsequent nodes as the shock wave moved proximally through the bones of the lower extremity. Additionally, PA values were compared between the nodes to determine the extent to which the PA was attenuated as the shock wave travelled along the length of the tibia and femur. The shock attenuation, represented by the reduction in peak acceleration, was calculated using Equation 5:

$$SA = [1 - (a_{\text{proximal}} / a_{\text{distal}})] \times 100 \quad [5]$$

where SA represents shock attenuation, ‘ $a_{\text{proximal}}$ ’ represents the PA at the proximal node, and ‘ $a_{\text{distal}}$ ’ represents the PA at the distal node (closest to the site of impact) (Dufek et al.,

2009). Using this formula, if the proximal PA is less than the distal PA, the SA value will be positive, indicating that the acceleration is being attenuated. Conversely, if the proximal PA is greater than the distal PA, the SA value will be negative, representing amplification of the acceleration as the wave travels proximally.

## Chapter 4 Results

### 4.1 Objective #1

#### 4.1.1 Shoe Crush Simulations

The original shoe was approximately 28 mm thick at the centre of the calcaneus, and the geometry resembled the sole of a shoe. Further, the material properties assigned to the shoe, specifically the Young's modulus ( $8.9\text{E}+06$  Pa) and the stress-strain curve (Figure 32), were not representative of those found in a biological heel pad.

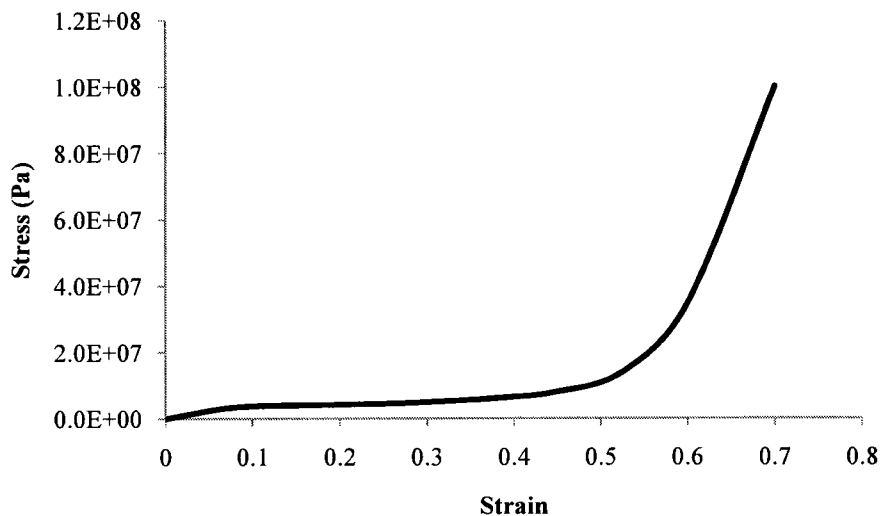
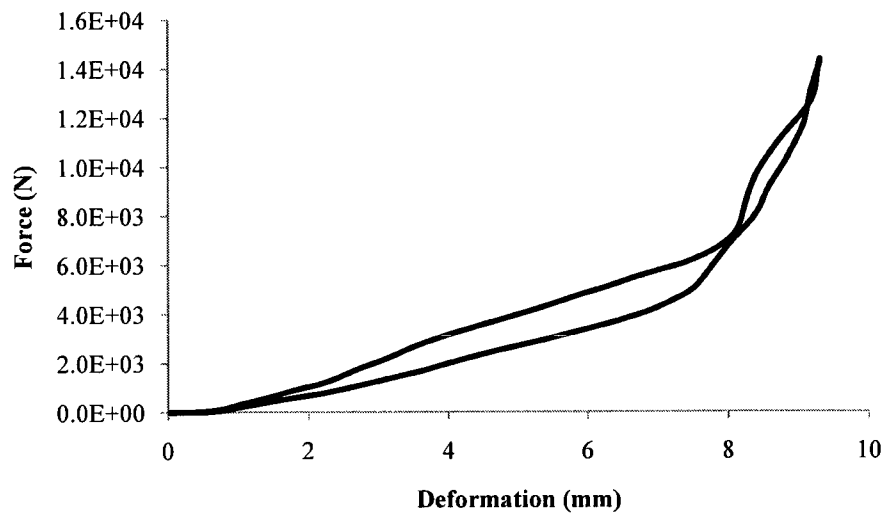
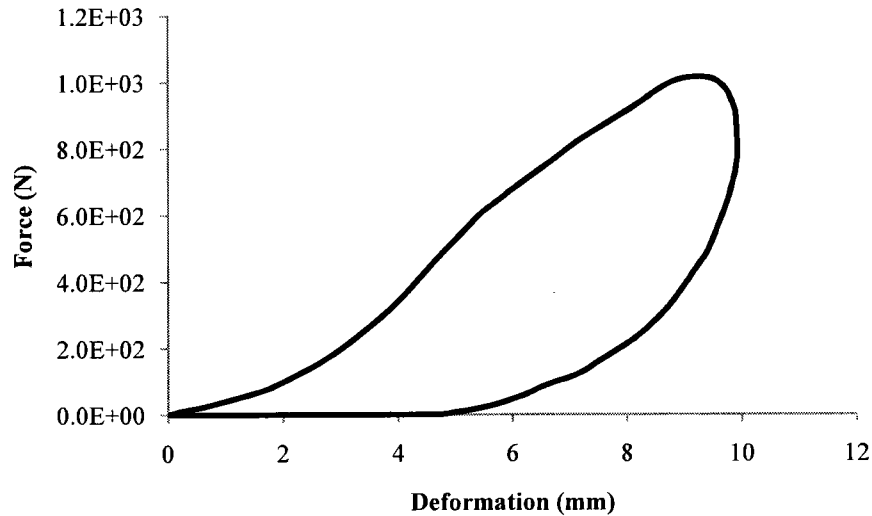


**Figure 32:** Stress-strain curve assigned to the original THUMS shoe.

When the displacement loading curve was prescribed to the rigid body inferior to the shoe for the crush simulation, a peak force of approximately 14 kPa was reached when the shoe was compressed by 9 mm (Figure 33a). The forces output from this version of the shoe crush model were substantially higher, by approximately an order of magnitude, than those obtained from in vivo testing of human heel pads (Aerts & De Clercq, 1993) (Figure 33b).



a)



b)

**Figure 33:** a) Force-displacement curve obtained from the crushing of the original THUMS shoe; b) Force-displacement curve obtained from in vivo human heel pad testing (adapted from Aerts & De Clercq, 1993).

Following the conversion and extrapolation of the force-deformation data from Aerts and De Clercq (1993) to a stress-strain curve (Figure 34), the coefficients to define the unloading behaviour for the shoe were determined. A hysteretic unloading factor of 0.01, a shape factor of 8.00, and a damping coefficient of 0.30 provided the best

replication of the human heel pad force-deformation data (Aerts & De Clercq, 1993)  
(Figure 35).

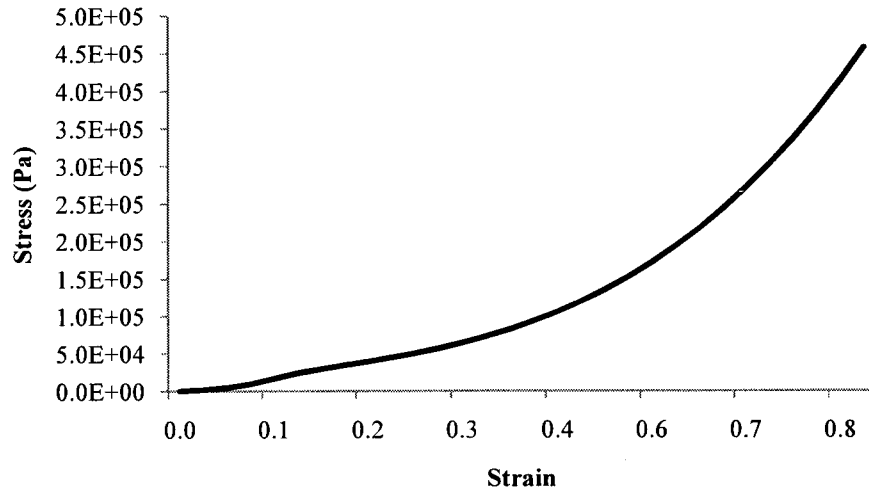


**Figure 34:** Extrapolated stress-strain curve based on Aerts and De Clercq's (1993) data.

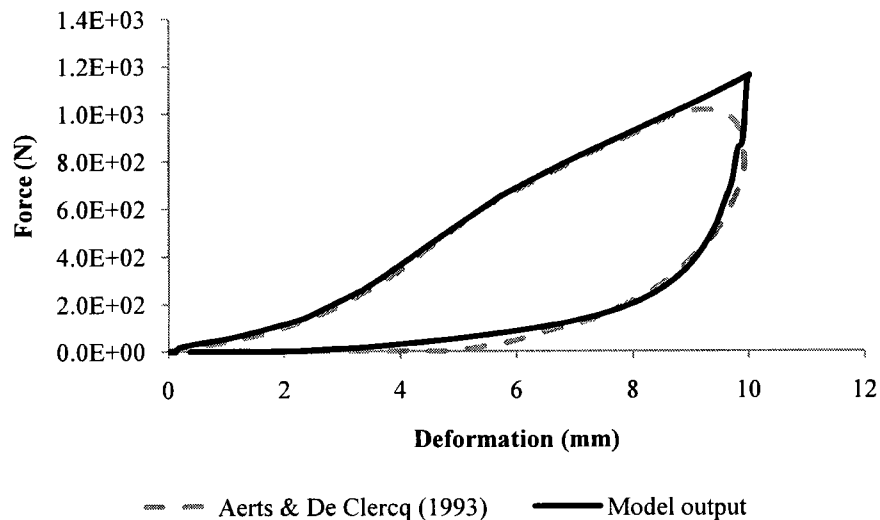


**Figure 35:** Final shoe crush simulation force-deformation curve, compared to in vivo heel pad data (Aerts & De Clercq, 1993).

Finally, the stress-strain data presented by Wearing et al. (2009) were extrapolated from 40% to approximately 90% strain (Figure 36). The data from 0-40% strain were used to calculate the value of Young's modulus ( $4.90E+05$  Pa). These parameters, along

with the coefficients for unloading determined from the shoe crush simulation, were input into versions 2 and 3 of the full body impact model. The complete material model for the modified shoe properties can be found in Appendix C.

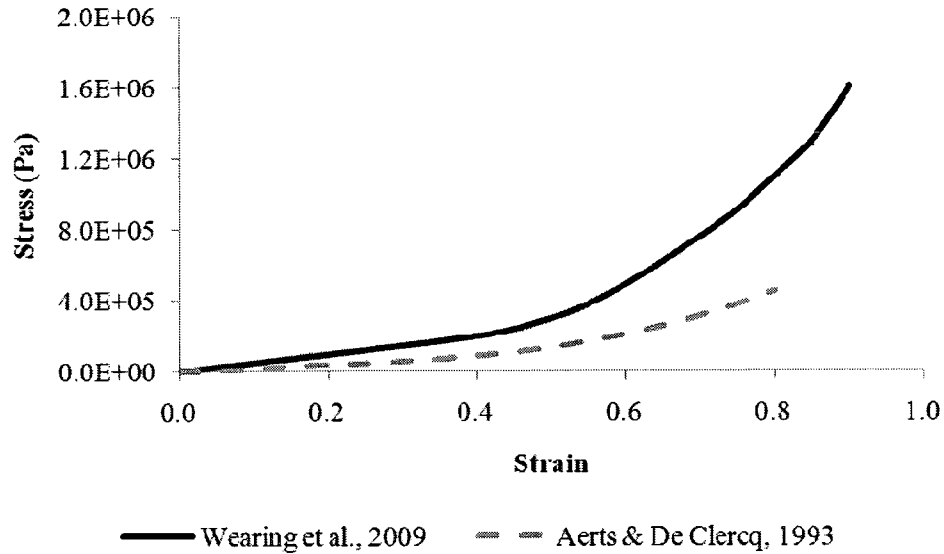


**Figure 36:** Extrapolated stress-strain curve based on Wearing et al.’s (2009) data (Curve from Figure 27 also presented for comparison).

#### 4.1.2 *Experimental Dependent Variables*

Ten experimental impact trials were analyzed for initial velocity, ankle angle, and activation levels for the TA and LG. Additionally, the impact force and tibial acceleration data were analyzed to determine the dependent impact force variables (peak force (PF), time to peak force (TPF), and loading rate (LR)) and tibial acceleration variables (peak acceleration (PA), time to peak acceleration (TPA), and acceleration slope (AS)) (Table 6). Additionally, the mean force-time and acceleration-time profiles for the 10 trials are displayed in Figures 37 and 38, respectively.

**Table 6:** Means (SD) for all experimentally measured variables (1 = first peak; 2 = second peak for force and acceleration).

Variable	Mean (SD)
Initial velocity (m/s)	1.1 (0.0)
Ankle angle (°)	89.4 (1.3)
TA activation (% MVE)	16.1 (2.8)
LG activation (% MVE)	8.1 (1.0)
Impact Force Variables	
Peak force 1 (N)	1822.6 (145.5)
Peak force 1 (BW)	2.4 (0.2)
Time to peak force 1 (ms)	27.6 (9.1)
Loading rate (kN/s)	283.7 (36.4)
Loading rate (BW/s)	378.7 (48.6)
Peak force 2 (N)	1315.9 (133.4)
Peak force 2 (BW)	1.8 (0.2)
Time to peak force 2 (ms)	85.8 (9.9)
Tibial Acceleration Variables	
Peak acceleration 1 (g)	19.2 (2.8)
Time to peak acceleration 1 (ms)	22.4 (8.3)
Acceleration slope (g/s)	4789.7 (1982.0)
Peak acceleration 2 (g)	3.2 (1.6)
Time to peak acceleration 2 (ms)	78.9 (9.3)

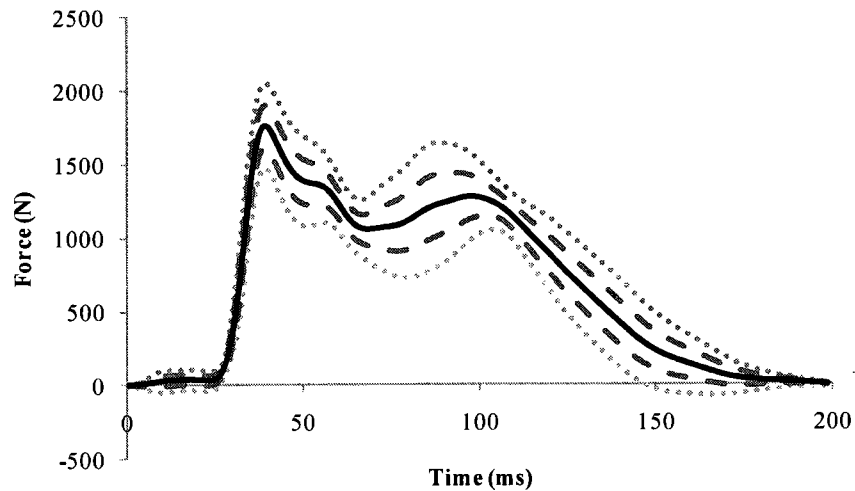


**Figure 37:** Mean force-time profile for the 10 experimental trials, represented by the solid black line. The dashed and dotted lines bound one and two SD, respectively.

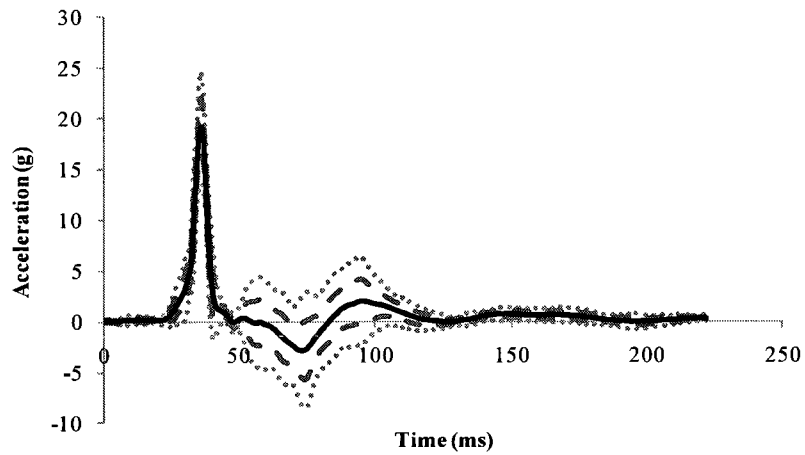


**Figure 38:** Mean acceleration-time profile for the 10 experimental trials, represented by the solid black line. The dashed and dotted lines bound one and two SD, respectively.

### 4.1.3 Full Body Impact Simulations

#### 4.1.3.1 Penetrations

No visible penetrations were observed at the ankle, knee, or hip joints of the left lower extremity, in either external (soft tissue included) or internal (soft tissue disabled) views. Version 2 of the full body model displayed approximately 9.15 mm of penetration between the calcaneus and the shoe. As version 2 demonstrated excessive penetrations between the shoe and the calcaneus, this version of the model was considered invalid, and will not be discussed in the remainder of Chapters 4 and 5.

#### 4.1.3.2 Global Energy Balance

The mean peak kinetic, internal, and total energy across versions 1 and 3 of the full body model were 102.1 J, 645.4 J, and 49.3 J, respectively (Table 7). Additionally, the time histories for each type of energy are displayed in Figure 39.

**Table 7:** Peak global kinetic, internal, and total energy (J) for each version of the model.

	Peak Kinetic Energy	Peak Internal Energy	Peak Total Energy
Version 1	101.4	790.1	46.4
Version 3	102.8	500.6	52.1

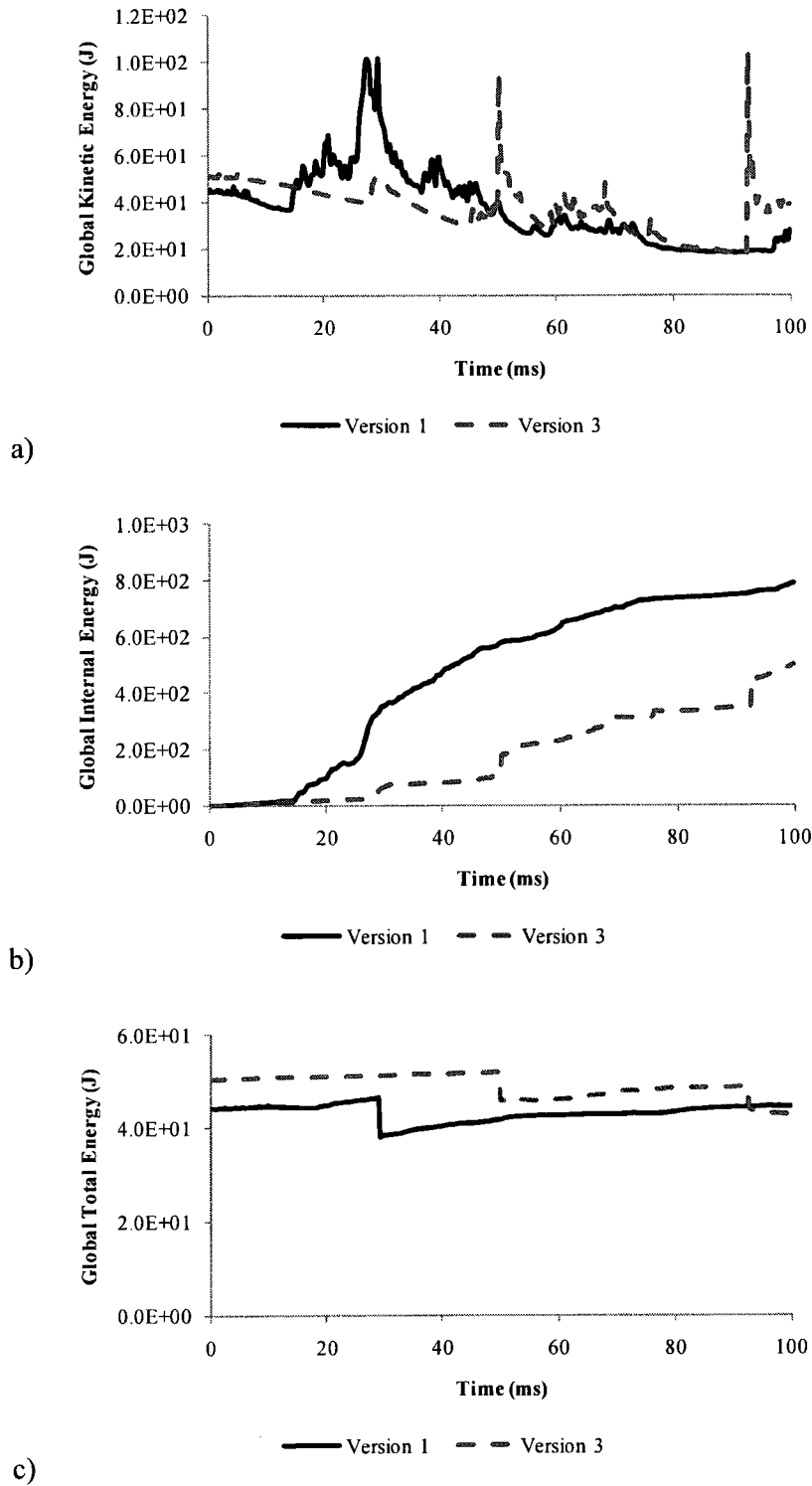


**Figure 39:** Time histories for the global a) kinetic energy; b) internal energy; c) total energy for each version of the model.

#### 4.1.3.3 Hourglass Energy and Sliding Interface Energy

The maximum HGE for versions 1 and 3 were 3817.4 J and 3624.9 J, respectively (Figure 40). Parts with HGEs exceeding 25.0 J accounted for 96.0% and 91.6% of the global HGE in versions 1 and 3 (Table 8). No left lower extremity parts were major contributors to the global HGE in either of the full body models.

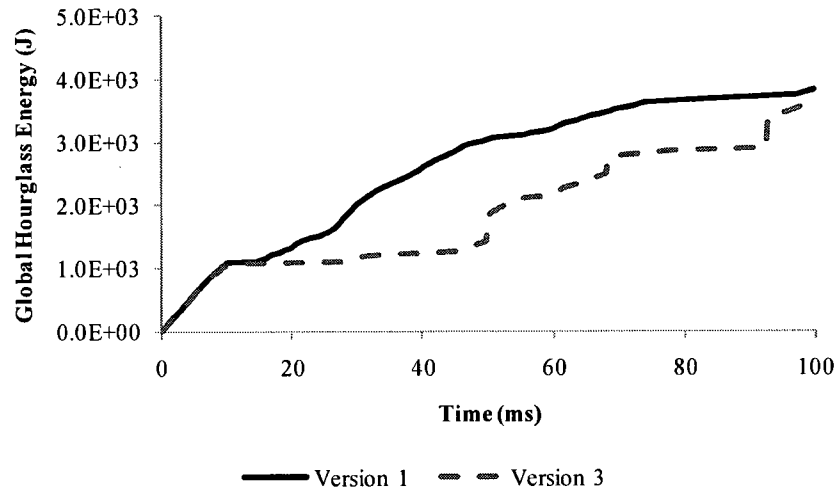


**Figure 40:** Global hourglass energies for each version of the model.

**Table 8:** Major sources of hourglass energy (HGE (J)) for each version of the model. (–) indicates that a part did not contribute substantially to the global HGE for that version.

Side of Body (L/R)	Part Name	Part #	Version 1	Version 3
R	Femur	8150200	978.8	967.4
R	Femur	8150400	77.7	767.0
R	Scapula	8550500	88.5	101.7
R	Scapula	8550510	–	30.4
R	Upper arm soft tissue	8580200	1151.6	429.8
R	Shoulder soft tissue	8580300	951.6	352.9
R	Shoulder skin	8580310	46.6	–
L	Humerus	8640100	28.7	–
L	Upper arm soft tissue	8680200	232.8	241.0
L	Shoulder soft tissue	8680300	35.1	63.6
R	Rib 10	8920900	–	314.6
L	Rib 10	8922900	–	347.5
R	Rib cartilage	8924000	–	205.7
L	Rib cartilage	8924100	–	26.2
R	Thorax soft tissue	8980000	–	137.6
R	Upper torso skin	8983000	73.3	25.8

The maximum SLE for versions 1 and 3 were -4591.2 J and -4121.6 J, respectively (Figure 41). For version 1, the SLEs associated with four contact algorithms in the right lower extremity and left and right upper extremities accounted for 98.5% of the global SLE. Similarly, for version 3, the SLEs associated with five contact algorithms in the right lower extremity, left and right upper extremities, and thorax accounted for 97.5% of the global SLE (Table 9). No left lower extremity contact algorithms were major contributors to the global SLE in either of the full body models.

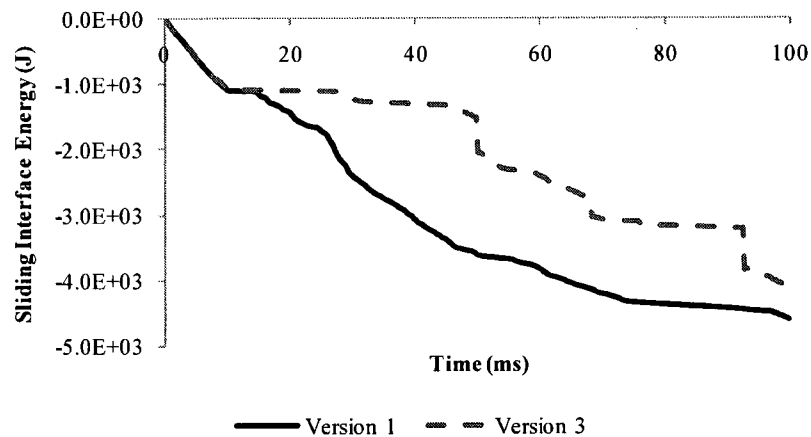


**Figure 41:** Global sliding interface energies for each version of the model.

**Table 9:** Major sources of sliding interface energy (SLE (J)) for each version of the model. (–) indicates that a part did not contribute substantially to the global SLE for that version.

Side of Body (L/R)	Contact Algorithm Name	Contact Algorithm #	Version 1	Version 3
R	ACL-PCL	8000030	-1060.0	-1048.0
L	Upper arm-bone	8000086	-264.6	-225.4
R	Viscus-in_muscle (thorax)	8000123	–	-1461.0
R	Shoulder soft tissue-upper arm	8000131	-3065.0	-1061.3
L	Shoulder soft tissue-upper arm	8000132	-131.5	-223.3

#### 4.1.3.4 Joint Kinematics

Qualitatively, it was observed that there were no major discrepancies between the left lower extremity joint behaviours of the model and the human participant. The joints of the model did, however, exhibit small movements in the frontal and sagittal planes at both the ankle and knee joints. The maximum range of motion exhibited at the left lower extremity joints over the course of the simulation, as well as the net change in angle from the beginning to the end of the simulation, are presented in Table 10.

**Table 10:** Changes in joint angles following impact for each version of the model. (+) moving in the direction of motion specified; (-) moving in the opposite direction within the same plane. \* left hip elevated relative to right hip.

Joint	Motion	Maximum Change (°)		Net Change (°)	
		1	3	1	3
Ankle	Dorsiflexion	+2.8	+4.8	+1.5	+4.5
	Eversion	+5.0	+3.7	+4.1	+3.1
Knee	Flexion	+8.0	+6.1	+6.4	+4.0
	Valgus	-3.8	+2.7	-2.1	+0.1
		Maximum Bilateral Difference (mm)		Net Bilateral Difference (mm)	
		1	3	1	3
Hip	Elevation	*42.6	*42.9	*40.0	*42.9

#### 4.1.3.5 Model Dependent Variables

Version 1 of the model resulted in greater impact forces and tibial accelerations compared to version 3 (Table 11). The PF and LR were higher in version 1 than in version 3 by 45.9% and 93.5%, respectively. Additionally, the TPF for version 3 was 11.2 ms longer than that of version 1. A similar pattern was observed for the tibial acceleration variables, in that the PA and AS were 55.6% and 58.9% higher, respectively, in version 1 than in version 3. As well, the TPA was 0.7 ms longer in version 3 than in version 1.

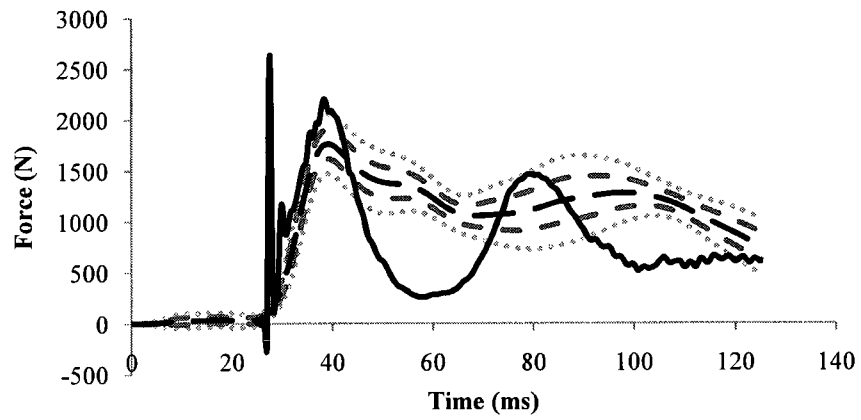
**Table 11:** Impact force and tibial acceleration variables for each version of the model (1 = first peak; 2 = second peak; a = output lined up at experimental data t=0; b = output lined up at t=25 ms and t=30 ms for force and acceleration, respectively).

Variable	Version 1	Version 3
<b>Impact Force Variables</b>		
Peak force 1 (N)	2208.3	1194.0
Peak force 1 (BW)	2.9	1.6
Time to peak force 1a (ms)	13.4	24.7
Time to peak force 1b (ms)	38.3	49.6
Loading rate (kN/s)	218.9	14.2
Loading rate (BW/s)	285.5	18.5
Peak force 2 (N)	1467.9	1249.9
Peak force 2 (BW)	1.9	1.6
Time to peak force 2a (ms)	54.2	65.4
Time to peak force 2b (ms)	79.1	90.3
<b>Tibial Acceleration Variables</b>		
Peak acceleration 1 (g)	24.2	10.7
Time to peak acceleration 1a (ms)	3.4	4.2
Time to peak acceleration 1b (ms)	35.9	35.9
Acceleration slope (g/s)	14394.4	5918.1
Peak acceleration 2 (g)	5.1	2.7
Time to peak acceleration 2a (ms)	49.3	66.9
Time to peak acceleration 2b (ms)	81.8	98.6

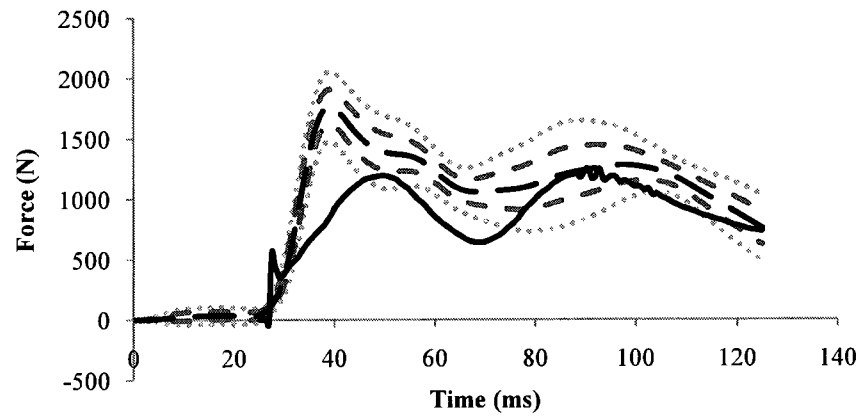
#### **4.1.4 Model Validation**

##### *4.1.4.1 Force- and Acceleration-Time Histories*

The mean experimental force and acceleration curves are plotted against the model outputs in Figures 42 and 43. Although the exact fit of the model force and acceleration data to the experimental data varied among the versions of the model, the curves qualitatively resembled the approximate time history of the experimental data, although the timing of the peaks varied in some instances.

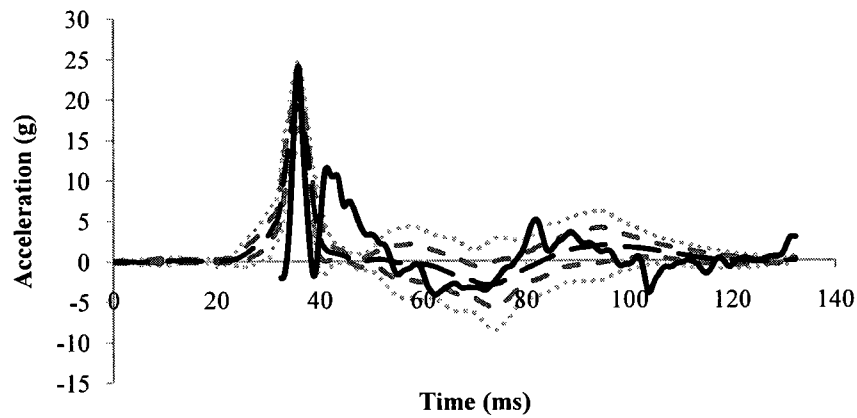


a)

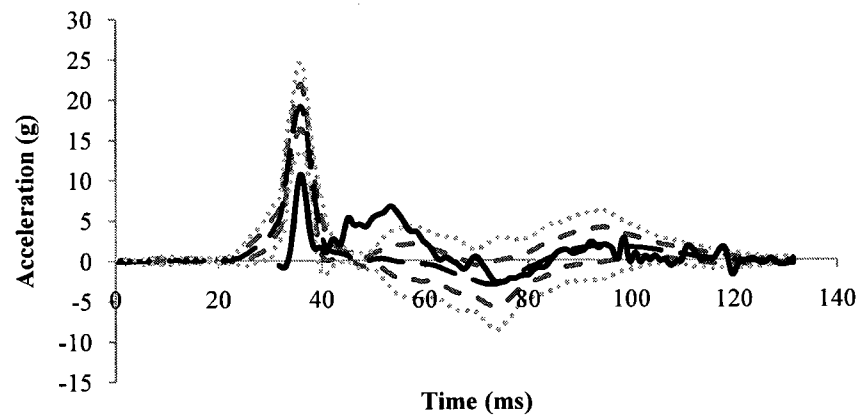


b)

**Figure 42:** Time shifted model versus experimental force-time histories for a) version 1; b) version 3 (large dashed, small dashed, and dotted lines = experimental mean, 1SD, and 2SD; solid black = time shifted model data).



a)



b)

**Figure 43:** Time shifted model versus experimental acceleration-time histories for a) version 1; b) version 3 (large dashed, small dashed, and dotted lines = experimental mean, 1SD, and 2SD; solid black = time shifted model data).

#### 4.1.4.2 Relative Error in Dependent Variables

The greatest relative error for the impact force variables was found between the experimental and version 3 LR, in that the version 3 LR was 95.0% smaller than the experimental value (Table 12). Conversely, the LR for version 1 was only 22.8% smaller than the experimental LR. Additionally, the full body model appeared to replicate the second force peak relatively well, with errors of less than 12.0% in the peak force magnitude for both versions. With respect to the acceleration variables, the greatest relative errors were seen between the experimental and version 1 AS (200.5% greater

than the experimental value), while the lowest errors were observed between the experimental and version 3 second acceleration peak (14.2%), and experimental and version 3 AS (23.6%).

**Table 12:** Relative error comparisons (% of experimental value, Equation 3) between the experimental and model data for impact force and tibial acceleration variables (1 = first peak; 2 = second peak; a = model output lined up at experimental data t=0; b = model output lined up at t=25 ms or t=30 ms for force and acceleration, respectively).

Variable	Version 1	Version 3
<b>Impact Force Variables</b>		
Peak force 1	21.2	-34.5
Time to peak force 1a	-51.4	-10.8
Time to peak force 1b	38.7	79.3
Loading rate	-22.8	-95.0
Peak force 2	11.6	-5.0
Time to peak force 2a	-36.9	-23.8
Time to peak force 2b	-7.8	5.3
<b>Tibial Acceleration Variables</b>		
Peak acceleration 1	26.0	-44.0
Time to peak acceleration 1a	-84.7	-81.5
Time to peak acceleration 1b	N/A	N/A
Acceleration slope	200.5	23.6
Peak acceleration 2	59.1	-14.2
Time to peak acceleration 2a	-37.5	-15.2
Time to peak acceleration 2b	3.7	25.0

#### 4.1.4.3 Validation Metric

The mean validation metric value for force was 0.68, ranging from 0.61 (version 1, t=0 ms) to 0.78 (version 3, t=25 ms) (Table 13). The mean validation metric value for acceleration was 0.34, with values ranging from 0.21 (version 3, t=0 ms) to 0.51 (version 3, t=30 ms). The corresponding relative errors for the entire time domain ranged from 0.22, or 22% (version 3 force, t=25 ms) to 1.08, or 108% (version 3 acceleration, t=0 ms).

**Table 13:** Validation metric values and relative error for force- and acceleration-time histories. Relative errors are presented in decimal form to correspond with Figure 22.

Version #	Variable	Time (ms)	Validation Metric Value	Relative Error
1	Force	t=0	0.61	0.41
	Force	t=25	0.62	0.40
	Acceleration	t=0	0.26	0.96
	Acceleration	t=30	0.37	0.75
3	Force	t=0	0.69	0.32
	Force	t=25	0.78	0.22
	Acceleration	t=0	0.21	1.08
	Acceleration	t=30	0.51	0.54

#### 4.2 Objective #2

The tracking of x-accelerations at specific nodes at the talus and along the length of the left tibia revealed that peak acceleration values decreased in magnitude as the distance from the site of impact increased (Table 14). Further, the times to peak acceleration tended to increase from distal (site of impact) to proximal along the lower extremity to the proximal tibia. However, the opposite trend was observed along the length of the femur, in that an increase in peak acceleration often occurred from distal to proximal locations. The times to peak acceleration along the femoral nodes were all very similar, and did not exhibit a consistent trend along the length of the femur. Acceleration-time histories for all ankle, tibial, and femoral nodes for versions 1 and 3 are displayed in Figures 44 and 45.

**Table 14:** Peak accelerations and times to peak acceleration for all ankle, tibial, and femoral nodes for each version of the model. Nodes are listed from distal (closest to the site of impact) to proximal.

Node Location	Node	PA (g)		TPA (ms)	
		Version 1	Version 3	Version 1	Version 3
Ankle (distal)	8210163	67.1	19.3	2.4	3.0
Tibia	8221499	50.0	17.5	2.7	3.4
	8220106	43.2	15.4	2.8	3.5
	8221133	35.5	13.1	3.0	3.7
	8220847	32.2	12.4	3.1	3.9
	8220560	29.7	11.7	3.1	4.0
	8220232	29.1	11.3	3.1	4.1
Femur	8251068	17.7	8.2	9.5	22.7
	8250312	17.9	9.0	9.5	22.8
	8251138	18.4	9.3	9.5	22.8
	(proximal)	8250753	18.3	9.6	9.5

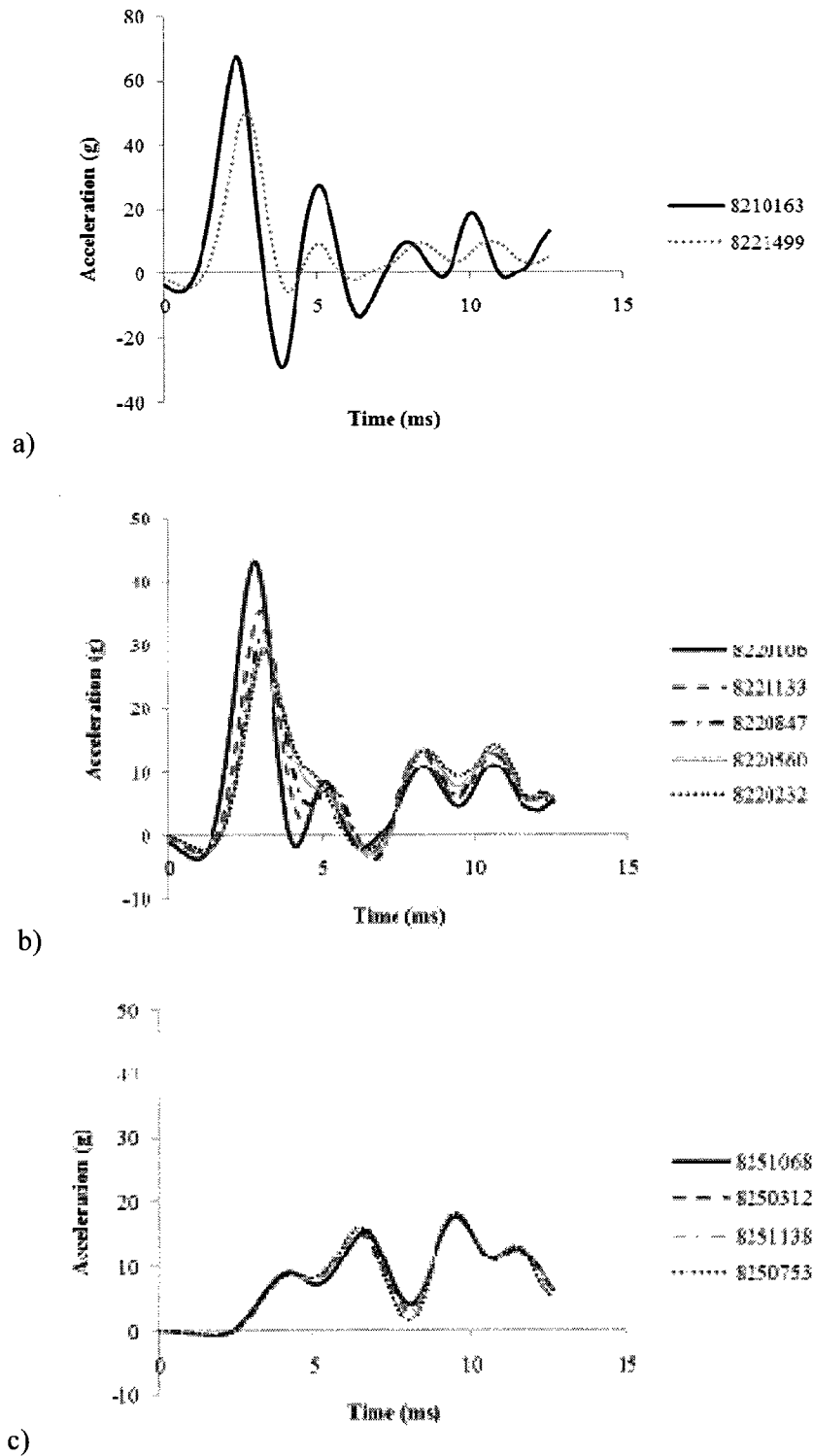
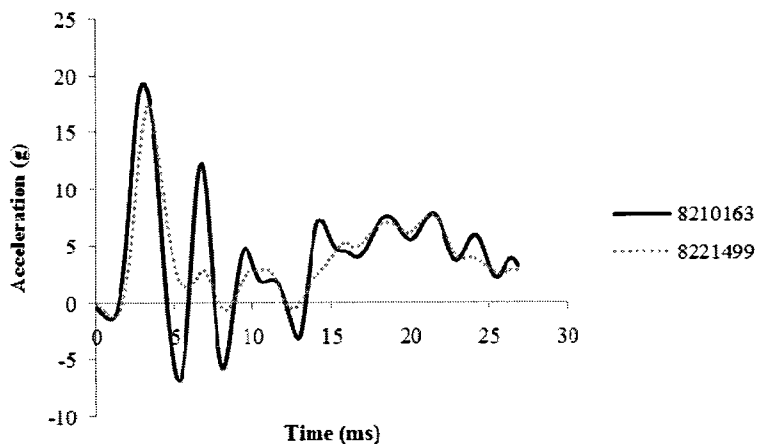
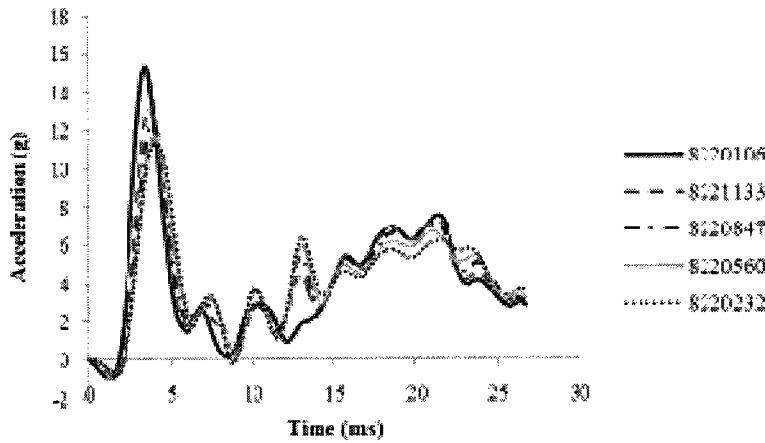


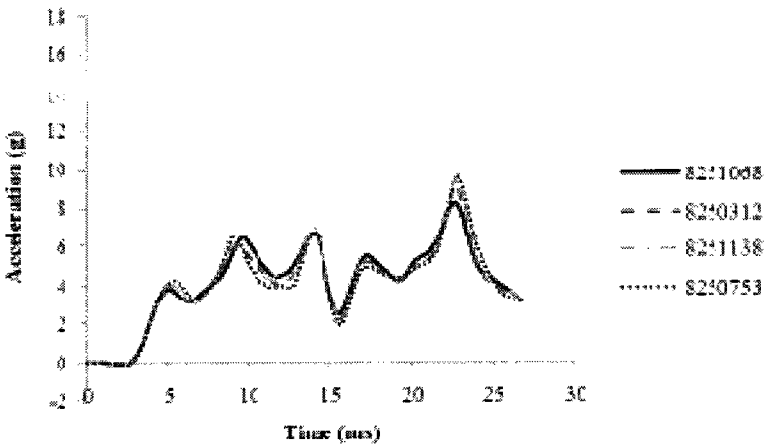
**Figure 44:** Acceleration-time histories for a) ankle nodes; b) tibial nodes; c) femoral nodes for version 1. Nodes are listed from distal to proximal.



a)



b)



c)

**Figure 45:** Acceleration-time histories for a) ankle nodes; b) tibial nodes; c) femoral nodes for version 3. Nodes are listed from distal to proximal.

Attenuation of the peak accelerations, as represented by the calculated shock attenuation values (Table 15), was observed across the ankle, along the tibia, and across the knee for each version of the model. With respect to attenuation across the ankle, the PA was reduced by 25.5% and 9.5% for versions 1 and 3, respectively. Similarly, the PA was reduced along the tibia by 32.7% and 26.4%, and across the knee by 39.2% and 27.3% for versions 1 and 3, respectively. Attenuation was more variable along the femur; in most cases, the peak accelerations were amplified as the shock wave moved proximally.

**Table 15:** Shock attenuation (SA) (%) between nodes along the lower extremity. Positive numbers indicate a reduction in PA (attenuation), while negative values indicate an increase in PA (amplification).

Location	Distal Node	Proximal Node	SA (%)	
			Version 1	Version 3
Ankle	8210163	8221499	25.5	9.5
Tibia	8221499	8220106	13.7	12.2
	8220106	8221133	17.8	14.5
	8221133	8220847	9.2	5.4
	8220847	8220560	8.0	5.8
	8220560	8220232	2.0	3.3
Knee	8220232	8251068	39.2	27.3
Femur	8251068	8250312	-1.2	-9.6
	8250312	8251138	-2.6	-3.5
	8251138	8250753	0.5	-3.0

## *Chapter 5 Discussion*

### 5.1 Objective #1

#### *5.1.1 Shoe Crush Simulations*

The first phase of Objective #1 was addressed in order to improve the biological fidelity of the shoe structure in the THUMS model. The original THUMS shoe was developed using material model 57 (MAT\_057 or MAT\_LOW\_DENSITY\_FOAM) in LS-DYNA, which is often employed to simulate highly compressible low density foams (LSTC, 2007). Common uses include the modelling of seat cushions and padding on Side Impact Dummies in automobile crash test modelling (LSTC, 2007). A limitation of MAT\_057 is that Poisson's effects are not accounted for, as the assumption is made that when the material is loaded uniaxially, its response does not couple significantly in the perpendicular axes (LSTC, 2007).

In accordance with the intended uses of the THUMS model (pedestrian-automobile impact testing), the shoe structure at the base of the THUMS foot was designed to behave as a shoe as opposed to a heel pad, in terms of both material properties and geometry. In order to improve the biological fidelity from the original material model, a stress-strain curve representing in vivo human heel pad properties was defined for the shoe, and the force and deformation data of a shoe crush simulation were compared to those available in the literature. However, to the best of the author's knowledge, very few, if any, previous studies have presented both stress-strain and force-deformation data for in vivo heel pads. Therefore, an in vivo force-deformation curve from Aerts and De Clercq (1993) was converted into a stress-strain curve using the geometry of the original THUMS shoe, and extrapolated past the available data points, as

instabilities can result in numerical simulations if a stress-strain curve does not encompass the full range of strains that occur in response to the imposed loading. This curve was used as an input into the shoe model, and the resulting force-deformation data from the shoe crush simulation were compared to the original curve from Aerts and De Clercq (1993) (Figure 35).

However, when the stress-strain curve from the shoe crush simulation was input into the full body model, it was found that the shoe was not stiff enough, which resulted in some penetration between the shoe and calcaneus. Upon further examination of the stress-strain curve compared to that presented by Wearing et al. (2009) for in vivo heel pads, it was found that the converted curve based on the data from Aerts and De Clercq (1993) represented a stress-strain response, and therefore a Young's modulus value, that was approximately 50% of those seen biologically (Figure 36). This resulted from the normalization of the force and deformation data from Aerts and De Clercq (1993) to obtain the corresponding stress-strain relationship. As the heel pad geometry of the participants in Aerts and De Clercq's (1993) study was not available, the thickness (0.041 m) and cross sectional area (0.027 m<sup>2</sup>) of the original THUMS shoe were used to normalize the deformation and force data to obtain strain and stress measurements, respectively. These measurements were substantially higher than those observed for heel pads in vivo (for example, heel pad thickness has been cited as anywhere from 0.012 m to 0.019 m (Gefen et al., 2001; Wearing et al., 2009)), thereby resulting in substantially lower stress and strain values following normalization to the shoe model thickness and cross sectional area. However, the shoe crush simulations with the stress-strain curve from Aerts and De Clercq's (1993) data were still used to determine the hysteretic unloading (HU) and shape factors associated with the shoe during the unloading phase,

which characterized the energy dissipation behaviour. The HU and shape factors were assigned as 0.01 and 8.00, respectively, which increased the energy dissipation of the shoe (Figure 46).

Ultimately, the stress-strain curve presented by Wearing et al. (2009) was extrapolated, and combined with the hysteretic unloading and shape factors that were determined previously. The values defined in the stress-strain curve were substantially lower than the original THUMS shoe stress-strain curve; for example, at 70% strain, the stress response for the modified curve based on Wearing et al.'s (2009) data was approximately 125 times less than the stress response for the original shoe ( $8.0\text{E}+05$  Pa versus  $1.0\text{E}+08$  Pa).

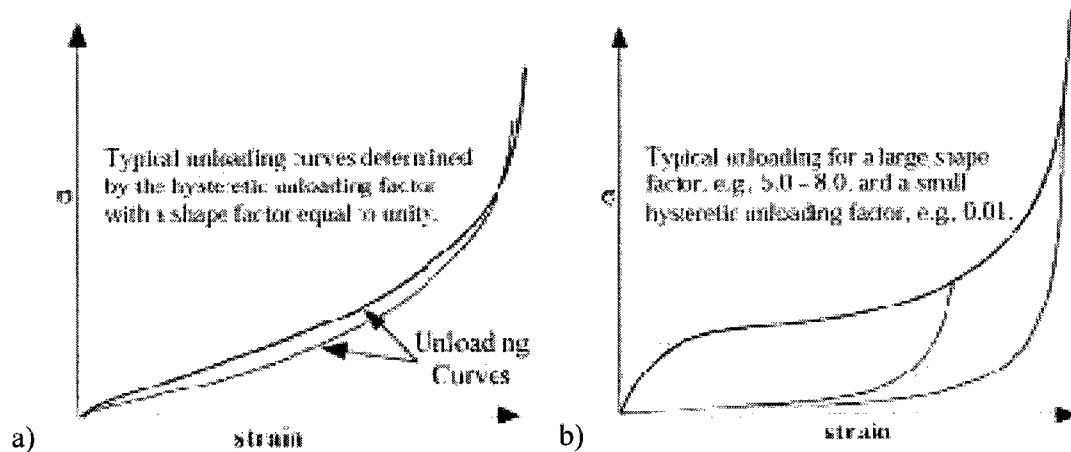


**Figure 46:** Effects of hysteretic unloading (HU) factor and shape (SHAPE) factors on the MAT\_057 unloading curve, a) HU and SHAPE equal to unity; b) small HU and large SHAPE (LSTC, 2007).

### 5.1.2 Experimental Dependent Variables

The mean (SD) experimental peak impact force ( $2.4$  ( $0.2$ ) BW) and impact velocity ( $1.1$  ( $0.0$ ) m/s) fell within the targeted range of  $1.8$ - $2.8$  BW and  $1.0$ - $1.15$  m/s used in previous studies (for example, Flynn et al., 2004; Holmes & Andrews, 2006).

The ankle angle ( $89.4$  ( $1.3$ ) °) and activation levels of the TA ( $16.1$  ( $2.8$ ) % MVE) and LG

(8.1 (1.0) % MVE) were found to be relatively consistent across the ten impact trials for the participant tested. The impact force variables (PF, TPF, and LR) were all similar to values that have been found previously using a human pendulum (Table 16). Conversely,

**Table 16:** Previous findings for dependent impact force and tibial acceleration variables. Conditions are reported only for those characteristics that are dissimilar from the present study (differing units are also reported in the Conditions column).

Authors	Conditions	Session	PF (N)	TPF (ms)	LR (kN/s)	PA (g)	TPA (ms)	AS (g)
Chavet et al. (1997)	- 20° knee flexion	Dominant leg	1268 (206)	-	131.3 (29.3)	9.8 (1.8)	-	-
	- LR 30-70% of peak	Non-dominant leg	1289 (201)	-	139.0 (35.9)	10.1 (2.0)	-	-
Flynn et al. (2004)	- Females only	Session 1	2.4 (0.3)	-	-	12.96 (4.7)	10.2 (3.0)	2830 (1972)
	- PF reported as BW	Session 2	2.4 (0.3)	-	-	11.86 (3.4)	10.7 (3.0)	2322 (1662)
Holmes & Andrews (2006)	- PF reported as BW	Session 1	2.2 (0.3)	-	-	12.11 (1.4)	9.0 (2.2)	1703 (549)
		Session 2	2.2 (0.2)	-	-	12.73 (1.7)	8.4 (1.9)	2095 (801)
Lafortune & Lake (1995)	- LR, AS 10-90% of peak		2.0 (0.2)	36.3 (6.9)	66.8 (22.5)	6.39 (0.7)	16.1 (3.0)	671.0 (220.0)
	- PF, LR reported as BW							
Lafortune et al. (1996a)	- LR 30-70% of peak	0° knee flexion	1425 (241)	26.7 (11.1)	194 (131)	9.4 (4.0)	22.5 (5.5)	1.2 (0.9)
	- AS reported as g/ms	Bare-foot	1430 (298)	14.2 (3.7)	335 (82)	16.1 (4.7)	17.4 (3.1)	3.0 (1.3)
Lafortune et al. (1996)	- 20° knee flexion		-	-	-	8.8 (2.6)	23.7 (4.1)	-
Schinkel-Ivy et al. (2010)	- Males only		-	-	-	9.6 (2.1)	14.4 (4.7)	1493.3 (697.3)
Current study	- PF reported as BW		2.4 (0.2)	27.6 (9.1)	378.7 (48.6)	19.2 (2.8)	22.4 (8.3)	4789.7 (1982.0)
	- LR reported as BW/s							

the dependent tibial acceleration variables (PA, TPA, and AS) were at the higher end of the range of the values reported in the literature (Table 16), potentially due to methodological differences or individual differences exhibited by the participant in the current study.

With respect to methodological differences, although all of the studies reviewed in Table 16 employed a human pendulum approach, some of the authors chose to have participants assume a knee flexion angle of 20°, in order to more closely imitate those knee angle conditions experienced during running. Increased angles of knee flexion tend to improve the ability of the body to attenuate shock, thereby reducing the magnitude of the accelerations measured at the tibia (Lafortune et al., 1996b; McMahon et al., 1987). Further, to the best of the author's knowledge, this is the first study in which the participant's non-impact leg was extended, as opposed to previous studies in which the non-impact leg was flexed with the foot resting on the pendulum frame. Although the potential for participants to use the non-impact foot to brace themselves against the frame of the pendulum during impacts has not been determined, it is possible that participants in the past studies have used this approach, either consciously or subconsciously, in an attempt to reduce the severity of the impacts. The participant in the current study was unable to use this approach, as his non-impact leg was abducted in order to better mimic the posture of the THUMS model, which may partially account for the higher tibial acceleration values found in the current study.

Furthermore, as only one participant was tested in the current study, it is possible that individual differences in his body and leg composition, kinematics, or muscle activation strategies may have contributed to the high acceleration values, as the aforementioned factors have been found to affect the propagation of the shock wave and

the accelerations measured at the tibia (Holmes & Andrews, 2006; Lafortune et al., 1996b; Schinkel-Ivy et al., 2010). Additionally, previous work has shown that inherent variability exists between individuals in terms of their tibial acceleration parameters; for example, Flynn et al. (2004) reported mean (SD) acceleration slope values of 2830 (1972) g/s and 2322 (1662) g/s over two sessions. Therefore, the mean AS value for the participant in the current study falls within 1 SD and 2 SD of the mean of the first and second sessions, respectively, for Flynn et al.'s (2004) participants.

### **5.1.3 Full Body Impact Simulations**

#### **5.1.3.1 Penetrations**

The only major penetration observed along the left lower extremity for any of the three versions of the model was between the shoe and the calcaneus in version 2 (Figure 47a). This was a result of the modification of the shoe material properties, which subsequently reduced the stiffness of the shoe. However, penetrations were not observed at this location for either of the remaining versions of the model, including version 3 (Figure 47b), in which the shoe material properties were identical to those in version 2. Upon visual inspection of the penetration in version 2, and comparison to version 3 where penetrations were not observed, it was found that the shoe in version 2 was able to act as more of a cushion to the calcaneus, and experienced a greater amount of deformation in the antero-posterior direction, than the shoe in version 3. Further, the shoe in version 2 was not flat along the bottom surface, with the result that each node contacted the rigid wall at slightly different times in the simulation, leading to some wobble in the shoe. Therefore, it was concluded that the penetration observed in version 2 was due to the coupling of the modified shoe properties with the original shoe geometry.

The generally accepted method used to combat penetration at contacting surfaces in finite element analysis is to increase the stiffness of the part experiencing the penetration. However, the reduction in the shoe's stiffness in version 2 that resulted in the penetration was necessary to increase the biological fidelity of the shoe, and therefore could not be avoided in this case. Due to this limitation, version 2 was removed from further analysis.

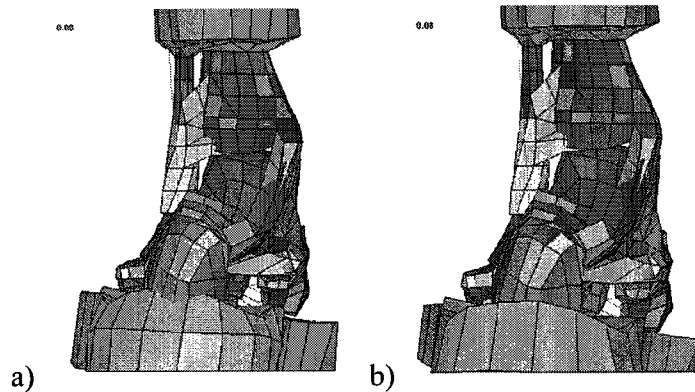


**Figure 47:** Posterior view of the shoe, foot, and ankle at 80 ms for a) version 2, in which 9.15 mm of penetration was observed between the shoe and calcaneus; b) version 3, in which no visible penetrations were observed.

#### 5.1.3.2 Global Energy Balance

The peak global kinetic energy was relatively consistent across both versions of the model. However, there were substantial variations in the global internal energy, in that the internal energy for version 1 was greater than that for version 3 (Table 7). This difference was primarily accounted for by the internal energies of parts representing the soft tissue and skin of the right upper extremity, indicating that the strain energy associated with the elements comprising those parts was greater in version 1. This was potentially due to different modifications in contact algorithms between the versions of the full body model. However, the internal energies of the parts of the left lower extremity remained consistent across both versions of the full body model.

Finally, the peak total energy also remained relatively consistent across both versions of the model (Table 7). Although ideally the total energy should equal the sum of the kinetic and internal energies, the results presented in Table 7 indicate that this was not the case for either version of the full body model. This was due to the means of calculating total energy as the sum of kinetic, internal, sliding, hourglass, system damping, and rigid wall energies. The global hourglass energy and global sliding interface energy were found to contribute substantially to the global energy balance of both versions of the full body model, which is generally considered undesirable. However, upon further investigation of the hourglass energies of each part, and sliding interface energies of each contact algorithm comprising the full body model, it was found that all of the major sources of hourglass energy and sliding interface energy were located in regions other than the left lower extremity (see section 5.1.3.3).

#### *5.1.3.3 Hourglass Energy and Sliding Interface Energy*

In finite element simulations, hourglass energy is undesirable, as deformation without the production of strain energy physically does not make sense. Although the global hourglass energies resulting from the model were quite high, peaking at 3817.4 J and 3624.9 J for versions 1 and 3, respectively (Figure 40), the vast majority of the global hourglass energy (greater than 90% of the peak value) was accounted for by parts located in the upper extremities (specifically the shoulders and upper arm soft tissue), thorax, and right lower extremity (Table 8). None of the parts of the left lower extremity, which was the region of primary interest in the current study, contributed substantially to the global hourglass energy. Therefore, it was concluded that no major nonphysical deformation occurred within the left lower extremity in either version of the full body model.

Similarly, the global sliding interface energies output from the model peaked at relatively high values of -4591.2 J and -4121.6 J for versions 1 and 3 (Figure 41), respectively, indicating that penetrations were occurring at various locations within the model. However, greater than 97% of the global SLE in both versions of the model was accounted for by contact algorithms within the upper extremities, thorax, and right lower extremity (Table 9). Any sliding interface energies resulting from contact algorithms in the left lower extremities were minimal (generally less than 1.0 J); therefore, it was concluded that no major penetrations existed with the contact algorithms in the left lower extremity for either version 1 or 3 of the full body model.

#### *5.1.3.4 Joint Kinematics*

Upon tracking the joint angles for ankle and knee movements in the frontal and sagittal planes, it was found that the model consistently exhibited small amounts of ankle dorsiflexion (mean net change in angle of 3.0°), ankle eversion (3.6°), and knee flexion (5.2°) in response to the imposed impact (Table 10). Changes in the angles at the ankle, both in the frontal and sagittal planes, could simply have been due to the loading pathway, and the location at which the force was concentrated under the heel. When the foot contacted the rigid wall, the impact force pathway may have been directed primarily through the medial, as opposed to the lateral, side of the heel, which may have caused elevation of the anterior and lateral sides of the foot in response to the impact. The small amount of observed knee flexion in the model could potentially be reduced by modelling the pendulum as a separate entity. Strapping the model to the pendulum as in the experimental protocol may aid in maintaining an extended knee. However, overall, the small changes in joint angles in the full body model indicated that the global behaviour of

the left lower extremity was relatively realistic in comparison to the experimental pendulum impacts.

Knee valgus-varus movements were more variable between the versions of the model, in that a net change in the varus direction was exhibited in version 1, while the opposite was observed for version 3. These differences were minor (net changes of  $-2.1^{\circ}$  and  $0.11^{\circ}$ , respectively), and were likely caused by changes in the shoe geometry. That is, in the original shoe geometry that was used in version 1, the nodes along the bottom of the shoe were all defined by slightly different z-coordinates, and therefore did not all contact the rigid wall at precisely the same time. Conversely, in version 3, all nodes were defined by an identical z-coordinate. These differences in the contact between the shoe and rigid wall may have contributed to the discrepancies in the knee valgus-varus movements. Additionally, the reduced stiffness of the shoe in version 3, and the cushioning effect that it provided to the bones of the foot, may have aided in reducing the joint excursions at the knee in the frontal plane.

The left hip was consistently elevated in relation to the right hip in response to the impact. This type of movement occurred due to inertial effects; although the movement of the left lower extremity was impeded by the rigid wall, the right lower extremity continued to move, resulting in the depression of the right hip. As no experimental work has examined this type of hip movement using a human pendulum approach, it was difficult to determine whether the extent of the elevation seen in the model is realistic. Potentially, as with the knee flexion-extension response, the extent of the elevation of the left hip may be improved by modelling the pendulum as an independent mass, and strapping the model to it.

The lack of active muscle properties in the model may have also contributed to the changes in joint angles, specifically the more proximal joints (knee and hip). Activation of the leg and thigh musculature improves the stability of the knee joint in vivo, thereby reducing the motion in both the frontal and sagittal planes, and may also assist in reducing the elevation of the left hip, thereby maintaining a more level pelvis.

#### *5.1.3.5 Model Dependent Variables*

When the force- and acceleration-time histories were examined for both versions of the model, similar trends were observed for the dependent impact force and tibial acceleration variables (Table 11). The highest PF, LR, PA, and AS values were observed for version 1, while version 3 had the longer TPF and TPA. Ultimately, version 1 experienced the greatest amount of force and acceleration over a shorter period of time, while version 3 exhibited lesser amounts of force and acceleration over a longer time.

The greater force and acceleration responses of version 1 were due primarily to the original shoe of the THUMS model. The original THUMS shoe material properties were substantially stiffer than those that were input for version 3. Additionally, the coefficients that defined the unloading behaviour, and thereby the energy dissipation of the shoe (hysteretic unloading and shape factors), were both set as zero. This combination of factors in the version 1 shoe increased the amount of force experienced by the model in response to impact, decreased the amount of energy dissipated by the shoe structure, and increased the magnitude of acceleration that was subsequently transferred through the foot, across the ankle, and along the tibia. These results agree with the general trend observed by Pain and Challis (2004), in that an increase in the stiffness of the heel pad of the model produced an increase in vertical GRF. The reduction in the stiffness of the shoe in version 3 enabled an increase in collision time due to greater

deformation, which contributed to an increase in energy dissipation, thereby reducing the peak force (Jorgensen & Bojsen-Moller, 1989), as well as the peak acceleration.

#### **5.1.4 Model Validation**

##### *5.1.4.1 Force- and Acceleration-Time Histories*

With respect to the force-time histories output from the full body model, both versions followed the general shape of the experimental force data, in that two peaks were seen in the forces over the duration of the event (Figure 42). The curve from version 1 matched relatively well with the experimental data in terms of both the magnitude and timing of the first peak, while the second peak occurred sooner than in the experimental data. Conversely, for version 3, the first peak was somewhat delayed in time relative to the experimental data, but the second peak matched up relatively well with the model data. The differences in force profiles between the versions may be attributed to the changes in shoe material properties and geometry, which will be further addressed during the discussion of the relative error in the dependent variables (see section 5.1.4.2).

Both versions of the full body model exhibited a transient change in force at the beginning of the time history. Previous work has examined this ‘heel strike transient’ phenomenon in gait (Dickinson et al., 1985; Light et al., 1979, Whittle, 1999) (Figure 48). These transients represent a rapid, sizeable deceleration that occurs following heel strike during barefoot gait, with peaks usually reached within 5 ms (Dickinson et al., 1985). The magnitudes of the heel strike transients recorded by Dickinson et al. (1985) (approximately 1.86 BW) were substantially different than any produced by the full body model in the current study; however, it is possible that the transient regions in the model force outputs represented an in vivo phenomenon. The fact that this transient region was not detected in the experimental impact force data may have been due to limitations with

the instrumentation used during the experimental protocol, specifically the force plate. The force plate had a natural frequency of 1000 Hz, and this frequency response may have limited the ability to detect the transient in the experimental data (Dickinson et al., 1985). Finally, the heel strike transient has only been examined in the context of gait, but not using a human pendulum approach; therefore, it is possible that the transient results from specific mechanics of gait that cannot be replicated with the human pendulum.

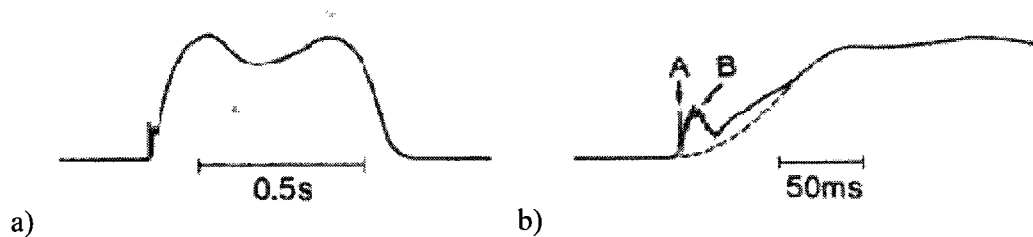


**Figure 48:** Schematic representing the ‘heel strike transient’ at the beginning of a typical gait profile; a) Typical force profile from a ‘vigorous’ step; b) Same as a), but with an expanded time scale (Light et al., 1979).

Finally, it is interesting to note that in both versions of the model, the forces returned to the original body weight of the full body model by the end of the simulation time. Version 1 returned to its body weight of 767.0 N within approximately 68.5 ms, while version 3 returned to the mean body weight of 883.5 N within approximately 92.5 ms. From this, it may be concluded that the model remained in contact with the wall following impact, as opposed to the experimental condition in which a rebound effect was observed following impact. Ultimately, this likely did not substantially affect the relative error between the experimental and model data with respect to the variables associated with the first impact force and tibial acceleration peaks (which were the primary focus of Objective #2, as opposed to the entire time history for force and acceleration); however, it may have contributed to some of the relative error measured across the entire time interval using the validation metric technique (Oberkampf & Trucano, 2002).

The acceleration-time histories from both versions of the model also approximated the general profile of the experimental data in terms of shape (Figure 43). Because accelerations were achieved by differentiating the velocity data using a central difference scheme, high frequency noise in the velocity data was amplified. Therefore, the model acceleration signals were substantially noisier than the experimental acceleration data, which were obtained directly from an accelerometer. As in the model force data, it was observed that by the end of the 100 ms simulation, the accelerations either returned to, or almost returned to, a steady state. Although this was somewhat faster than the documented 200-250 ms for soft tissue (Andrews & Dowling, 2000; Lafortune et al., 1996a; Pain & Challis, 2002), it was not entirely surprising, as visual inspection of the model following impact revealed that the soft tissue did not appear to wobble to the same extent as biological soft tissues. Therefore, it was concluded that the model exhibited reduced soft tissue motion in response to impact (compared to in vivo impact testing), and the soft tissues settled back to the baseline (pre-impact) state in a shorter period of time.

#### *5.1.4.2 Relative Error in Dependent Variables*

Both versions of the full body model exhibited a similar pattern with respect to the direction of the relative error from the experimental values for both the impact force and tibial acceleration variables (Table 12). Version 1 exhibited higher PF, PA, and AS values than the experimental values, while version 3 exhibited lower values than the experimental for PF, LR, and PA. Further, both versions exhibited smaller TPA values than the experimental, although those for version 1 were shorter than for version 3.

The impact force and tibial acceleration variables from version 1 were greater in magnitude and occurred more quickly than those experienced by the participant tested in the experimental protocol, and those reported previously in the literature. However, it is

important to note that the version 1 LR fell within the two-standard deviation range around the mean of the experimental data, and the PF and PA also fell close to this range.

The differences between the experimental and version 1 force and acceleration variables could potentially be due to the higher stiffness of the shoe structure in version 1, relative to an *in vivo* human heel pad. As discussed previously, an increased stiffness of the shoe would decrease the collision time, reducing the ability of the shoe to dissipate energy and ultimately increasing the impact force experienced by the model (Jorgensen & Bojsen-Moller, 1989). The increased impact force exhibited by version 1 would subsequently contribute to a greater transfer of acceleration across the ankle and along the tibia, resulting in the high PA value measured at the proximal tibia. This relationship between the magnitudes of impact forces and tibial accelerations has also been observed in live humans (Milner et al., 2006). Additionally, the version 1 AS value was substantially greater than the mean experimental value, in part due to the greater PA but primarily to the very fast rise in acceleration to its peak value (3.4 ms). This rapid response indicates that the shock wave, which is represented by the peak acceleration, was transferred more quickly across the ankle and along the length of the tibia of the model than what has been observed physiologically.

Version 3 also responded similarly in terms of the times to peak for both force and acceleration, although the relative error with respect to the experimental data was improved compared to version 1. The biological material properties assigned to the shoe appeared to have an effect in terms of lengthening the force and acceleration responses (increased times to peak), as well as reducing the magnitudes of the peak values (PF, PA) and slopes (LR, AS). Although the PA value for version 3 (10.7 g) was substantially lower than the PA measured experimentally in the current study, the version 3 PA fell

within the range of experimental PA values documented previously in the literature (Chavet et al., 1997; Flynn et al., 2004; Holmes & Andrews, 2006; Lafortune & Lake, 1995; Lafortune et al., 1996a, b; Schinkel-Ivy et al., 2010) (Table 15). It is also important to note that although an attempt was made to replicate, as closely as possible, the location of the selected tibial node (at which accelerations were measured) with respect to the experimental condition, the acceleration data collected during the simulations were measured directly at the node. Conversely, in the experimental protocol, the acceleration data were not measured directly at the point of interest, as an interface existed between the accelerometer and the point of interest on the soft tissue. An effort was made to minimize any effects of the interface by preloading the accelerometer using an elastic strap; however, the presence of the accelerometer may have had a small effect on the measured accelerations, although it was not expected that this would account for the majority of the error in the dependent tibial acceleration variables.

Although the reduced stiffness of the heel pad served to lengthen the times to peak acceleration for version 3 relative to version 1, the TPA values for both versions were substantially lower than those found experimentally (Table 12). There are several possible explanations for this phenomenon. In both versions of the model, the entire surface area of the heel of the shoe contacted the rigid wall simultaneously. However, due to the geometry of an unshod human heel, the centre of the heel would contact the force plate first, followed by the remaining surface area over a period of several milliseconds. The resulting increased time of contact between the heel and the force plate could potentially lengthen the tibial acceleration waveforms and resulting TPA values.

Further, substantial soft tissue movement can be observed when human participants are subjected to running-type impacts. However, when qualitatively

examining the response of the full body model to a running-type impact, very little soft tissue motion was observable in the shank and thigh. As previous studies have found that an increase in the amount of soft tissue movement relative to the bone results in longer TPA values following impact (Duquette & Andrews, 2010b; Flynn et al., 2004; Holmes & Andrews, 2006), the fact that minimal soft tissue motion occurred in the full body model may have also contributed to the low TPA values.

Through the comparison of the experimental dependent force and acceleration variables with the same values from the two versions of the model, it is evident that the properties and geometry of the shoe structure have a relatively large effect on both the forces and accelerations experienced by the model. The combination of modified material properties and geometry resulted in 45.9% and 55.6% reductions in peak force and acceleration from the original model, respectively. The effects of modifications to the shoe structure are supported by the literature, in that heel pads have been found to be major contributors to energy dissipation following impact; for example, Cavanagh et al. (1984) found that in vivo heel pads absorbed 85% and 90% of the energy at impact velocities of 1.03 and 1.44 m/s, respectively. Overall, although the modifications to the heel pad resulted in impact force values that were indicative of a lower-magnitude impact than the experimental protocol, the tibial acceleration magnitudes were similar to those observed previously in the literature.

#### *5.1.4.3 Validation Metric*

The validation metric employed in the current study was proposed by Oberkampff and Trucano (2002) to quantify the relative error between experimental and model data. Although the resulting relative errors appeared to be substantial (mean relative error of 34% and 83% for force and acceleration, respectively), it is important to note two

characteristics of the validation metric: the relative error was calculated across the entire time interval (in this case, 100 ms); and as the absolute value of the error at each discrete point was taken, the error could only accumulate, as opposed to positive and negative values cancelling each other (Jin et al., 2010).

For both versions of the model, the validation metric values for both force and acceleration were improved by artificially inducing a phase shift in the model profiles relative to the experimental data (Table 13). Upon impact with the wall, the model experienced an almost instantaneous increase in force, and subsequent rise in acceleration. However, experimentally, the force and acceleration were maintained around 35 N and 0.5 g, respectively, for approximately the first 25 ms following impact, thereby accounting for the higher relative errors when the model data were lined up at the experimental  $t=0$  ms. Although the phase shift in the full body model impact force and tibial acceleration profiles did result in higher validation metric values and lower associated relative errors, it must be noted that the phase shift was imposed to demonstrate that features of the model waveforms, such as the approximate shape and, in some cases, loading rates and acceleration slopes, were reflective of the experimental data. The fact that the full body model could reproduce these features of the experimental data to some extent was encouraging; however, it may be prudent in future work to address differences in the timings of the experimental and model peak accelerations in response to impact, in order to improve the agreement between the TPA values (see section 3.1.4.1).

Overall, for the comparisons of the force profiles, version 3 provided the highest validation metric value (0.78), and therefore the lowest relative error (22%). The force profile from version 1 qualitatively provided a close fit to the first part of the curve

(approximately the first 10-15 ms). However, version 3 appeared to exhibit a better fit to the experimental data for the last 60-70 ms of the curve, in that the local minimum following the first peak, as well as the second peak, fell within 1-2 standard deviations around the mean experimental force curve. Additionally, the force curve for version 1 fell to a steady state (around approximately 1 BW) much more quickly than those of the experimental data or version 3. These characteristics of the force curve for version 3 contributed to the lower relative error than that calculated for version 1.

The model acceleration profiles exhibited substantially smaller validation metric values, and therefore larger relative error, when compared to those for the force profiles. This could potentially be due to the methods used by LS-DYNA to obtain the force and acceleration data. The force data were calculated directly, while the acceleration data were obtained through the differentiation of nodal velocities, which amplified any high frequency noise within the velocity data. Therefore, although the general shapes of the acceleration-time histories from the three versions of the model mimicked the approximate shape of the mean experimental acceleration profile, the model data were substantially noisier than those obtained from the experimental protocol, thereby contributing to higher relative error.

Similar to the comparisons for the force profiles, the acceleration profiles for version 3 provided a better approximation relative to the experimental data (validation metric values of 0.51 and relative error of 54%). Although the profile for version 1 appeared to provide a better representation than version 3 with respect to the initial peak acceleration, the remainder of the profile for version 1 exhibited more variability around the mean experimental acceleration than did version 3. Qualitatively, version 3 appeared to match relatively well with the second half of the experimental curve.

## 5.2 Objective #2

Across the ankle joint and along the length of the tibia, it was consistently found for both versions of the model that the peak accelerations were attenuated between each consecutive node (Tables 14 & 15). Although the ankle was responsible for a smaller proportion of shock attenuation than the distal tibia, this potentially could have been a function of the smaller distances between the most distal nodes. As previously discussed, version 3 exhibited the most biologically realistic peak acceleration values at the bone surface of the proximal tibia at 11.3 g, which is similar to those reported previously in the literature (Chavet et al., 1997; Flynn et al., 2004; Holmes & Andrews, 2006; Lafortune et al., 1996 a, b; Schinkel-Ivy et al., 2010) (Table 16). With respect to the times to peak acceleration at each node, although the absolute TPA values may have been somewhat smaller than what were measured experimentally in the current study, the trend for each TPA value to be slightly delayed from that at the previous node indicated that the model reasonably represented the proximal movement of the shock wave across the ankle and along the tibia. Furthermore, previous work has reported that the peak accelerations at the distal tibia and head are removed in time by 10 ms (Derrick et al., 1998) and an average of 5.6 ms depending on impact velocity (Lafortune et al., 1996b). When these past results are taken into consideration, it appears that the small delays in time between adjacent nodes across the ankle and along the tibia may not be completely biologically unrealistic.

Similarly, it was observed that the peak accelerations were reduced from the most proximal tibial node to the most distal femoral node, indicating that the propagation of the shock wave was also represented across the knee joint (Wosk & Voloshin, 1981). The accelerations at the latter node took much longer to reach their peak magnitude, which

could potentially be explained due to the increased distance between the two nodes (13.1 cm, compared to the 7-8 cm between the rest of the nodes), as well as the time necessary for the joint structures (for example, the joint spaces and menisci) to compress and transmit the acceleration across the knee to the femur.

However, the acceleration profiles at the femoral nodes showed the opposite trend, in that a small gain in PA occurred along the length of the femur. Further, the TPA values showed no consistent trend from the most distal to most proximal node.

Considering that the tibia displayed evidence of a shock wave response following impact, some difference must exist between the tibia and femur that resulted in the variations in acceleration patterns. Although there are slight differences in the material models for each of the bones (for example, slightly lower Young's modulus and yield stress, slightly greater tangent modulus in the femur), the variations in shock wave behaviour may be due more to the behaviour of the structures located inferior to each bone. The shoe and menisci sit inferior to the tibia and femur, respectively, and both are represented by the same material model, MAT\_057 (low density foam). However, the modulus value for the menisci ( $2.2E+7$  Pa) is somewhat stiffer than that of the shoe ( $8.9E+6$  Pa). Additionally, the bones of the foot separate the shoe and the tibia, and may assist in the attenuation of any wobble or rebounding behaviour of the shoe (similar to what was seen during the shoe crush simulations performed during the first phase of the study). Conversely, the femur sits immediately superior to the menisci, so any rebound behaviour would be transmitted directly to the femur.

In addition, some support for these findings may be found within the body of literature focusing on low back pain and the biomechanical modelling of the spine. McGill et al. (1989) investigated the transmission of impact forces through the trunk in

sitting participants. Impacts were applied at the shoulders and the head, and the resulting forces were considered to be the input to the system, while the reaction forces measured at the bottom of the pelvis were considered to be the output. It was expected that the impact forces would be attenuated between the sites of input and output; conversely, the authors found that the forces were actually amplified when the time to peak force was less than 300 ms (McGill et al., 1989). The authors hypothesized that the amplification of the impact force may have been due to the upper body mass first being driven downwards under the force of the impact, and subsequently rebounding away (McGill et al., 1989).

A similar effect may apply to the amplification of peak accelerations along the length of the femur of the full body model found in the present study. That is, the peak accelerations recorded in the femur may have been due to the impact of the upper body mass with the femur at the hip joint, and subsequent rebound of the upper body mass away from the femur. Further, this impact at the hip joint may have initiated a second shock wave which was transmitted distally along the femur to the knee joint. This would explain the trend of increasing peak accelerations with proximal movement along the length of the femur. It is possible that some of the oscillation in the acceleration measurements at the femoral nodes resulted from shock waves originating at two locations: one at the site of external impact between the foot and the wall, and another at the hip joint, due to the impact between the head of the femur and the upper body mass.

Through an examination of Figures 44 and 45, it can be seen that while the peak acceleration at the most proximal tibial node occurred at 3.1 and 4.1 ms for versions 1 and 3, respectively, the TPA for the most distal femoral node occurred at 9.5 and 22.7 ms (Table 14). However, for both versions of the model, some oscillation was evident in the acceleration profiles of the most distal femoral node, and two local maxima occurred

prior to the peak acceleration. Therefore, if the peak acceleration was representative of a shock wave initiated at the hip joint, one of the local maxima preceding the peak may have been representative of the original shock wave (initiated at the foot-ground interface). However, these local maxima values were not used to calculate shock attenuation along the femur; it is suggested that this issue be addressed in future work, in order to determine which of the maxima in the acceleration-time history corresponds to the shock wave originating from the foot-ground impact.

It is important to note that the validation phase of this study was only conducted on the shank segment of the model, and did not include the knee joint or femur of the model. Additionally, experimental acceleration data were only collected at the level of the proximal tibia, so it is unknown whether this amplification effect would also be observed along the length of the femur during an *in vivo* impact scenario. If the amplification effect does occur physiologically, it may not be possible to observe it using the human pendulum protocol, as the method used to secure participants to the pendulum (using a 5 cm wide strap across the thigh of the impact leg) may interfere with the measurement of accelerations proximal to the tibia. Should this be the case, it may be necessary to use a protocol involving drop landings or running impacts. Regardless, further investigation should be conducted regarding the behaviour of the knee joint and femur both in live humans and in the full body impact model, in order to determine the cause(s) of the amplification of accelerations along the femur.

To the best of the author's knowledge, no studies using human participants have been performed to examine the changes in acceleration variables along the length of the tibia. Traditionally, previous work has either measured acceleration at a sole location on the tibia, in order to examine the effects of variables such as muscle fatigue (Flynn et al.,

2004), muscle activation (Holmes & Andrews, 2006), or leg tissue composition (Schinkel-Ivy et al., 2010), or at one location on the tibia and one on the head, to examine shock attenuation by the body in response to different gait conditions such as altered stride length (Derrick et al., 1998; Mercer et al., 2003b) or stride frequency (Hamill et al., 1995). The body of work representing the latter protocol has found that the shock attenuation between the tibia and the head is approximately 70% (Table 17). The shock attenuation values of 32.7% and 26.4% along the length of the tibia for versions 1 and 3 of the model, although possibly slightly higher than what occurs biologically based on the whole body shock attenuation values, are not completely unreasonable. Conversely, the times at which the peak accelerations occurred along the tibia may be unlikely in a live human, as they occur very quickly; however, it is encouraging that each peak acceleration along the length of the tibia was slightly delayed in time from that of the previous node, indicating that the shock wave phenomenon seen experimentally in the literature (for example, Dufek et al., 2009; Mercer et al., 2002, 2003a, Thomas & Derrick, 2003; Voloshin et al., 1981; Wosk & Voloshin, 1981) was being represented to a certain extent. Further, although the model has not been validated above the level of the proximal tibia for gait-type impacts, the shock attenuation observed across the knee of the model (39.2% and 27.3% for versions 1 and 3, respectively) is very similar to the values reported by Wosk and Voloshin (1981). Those authors found that between the tibial tuberosity and medial femoral condyle, the peak acceleration was attenuated, on average, by 26.9% (Wosk & Voloshin, 1981).

**Table 17:** Reported values of shock attenuation (SA) between the tibia and the head.  
 \*values originally presented as  $PA_{\text{proximal}} / PA_{\text{distal}}$ .

Authors	Method of SA Calculation	Whole Body SA
Wosk & Voloshin, 1981: walking	$[1 - (PA_{\text{proximal}} / PA_{\text{distal}})] \times 100$	69.8%
Voloshin et al., 1981: barefoot walking	$PA_{\text{tibial}} / PA_{\text{head}}$	3.7
Mercer et al., 2002: running	$[1 - (PA_{\text{proximal}} / PA_{\text{distal}})] \times 100$ *	85% at 50% max running speed 86% at 60% max running speed 90% at 70% max running speed 91% at 80% max running speed 92% at 90% max running speed 94% at 100% max running speed
Mercer et al., 2003a: running	$[1 - (PA_{\text{proximal}} / PA_{\text{distal}})] \times 100$	70.0%
Thomas & Derrick, 2003: running	$PA_{\text{head}} / PA_{\text{tibial}} \times 100$	72.4%
Dufek et al., 2009: running	$[1 - (PA_{\text{proximal}} / PA_{\text{distal}})] \times 100$	72.1%

### ***5.3 Hypotheses Revisited***

- 1. The shoe structure of the THUMS model would be more representative of a shoe with respect to its material properties and behaviour. The material properties of the shoe will require modifications to better represent the behaviour of a human heel pad.*

The structure inferior to the THUMS foot bones was developed to be representative of a shoe, as opposed to a heel pad. Modifications to the shoe with respect to the loading (defined by the stress-strain curve and Young's modulus) and unloading behaviour (defined by the hysteretic unloading factor, shape factor, and damping coefficient) were necessary, and appeared to improve the relative errors between the experimental and model impact force and tibial acceleration data for some of the dependent variables (PF, TPF, LR; PA, TPA, AS).

- 2. It was hypothesized that the model would represent the response of the lower extremity to a simulated running impact to a certain extent. However, some*

*modifications to the model at the interface between the foot and impact surface may be necessary.*

Various modifications to the contact algorithms of the upper arms, shoulders, and torso were necessary to enable the simulation to run to its full completion time without terminating due to numerical instabilities. However, the knee and ankle joints of the left lower extremity behaved in a realistic manner with respect to joint movements in the frontal and sagittal planes. Further, although the some of the relative errors between certain impact force and tibial acceleration variables were substantial, others were relatively close to the experimentally measured values, and the shapes of the force- and acceleration-time histories from both versions of the full body model qualitatively resembled the approximate shape of the equivalent experimental curves.

3. *It was hypothesized that the amplitude of the acceleration would decrease in magnitude with proximal movement along the lower extremity, and that the knee joint of the model would attenuate a substantial proportion of the acceleration. With respect to temporal characteristics, the times at which the peak accelerations occur at each node will be slightly delayed from that of the node immediately before.*

The peak accelerations for both versions of the model decreased in magnitude with proximal movement along the tibia, and underwent a substantial reduction across the knee joint. Additionally, the peak accelerations were all delayed in time from the adjacent distal node. However, the opposite trend was observed for the femoral nodes; the peak accelerations increased in magnitude with proximal movement, and a consistent trend in terms of times to peak acceleration was not observed.

## *Chapter 6*

### *Limitations and Future Directions*

The limitations of the human pendulum approach for simulating lower extremity impacts have been well documented (Flynn et al., 2004; Lafortune & Lake, 1995). The human pendulum approach enables a high level of control over initial impact conditions, which may not be possible during real-life scenarios such as running. This is achieved at the expense of a completely accurate representation of the dynamic kinematics of the lower extremity during running (Flynn et al., 2004); specifically, the ankle, knee, and hip angles during human pendulum impacts differ from those exhibited by humans during gait. Additionally, although the vertical component of the ground reaction forces and the axial component of tibial accelerations fall within the range of those documented for running, the restricted line of progression used in this approach does not necessarily allow for the realistic simulation of the remaining components of force and acceleration (Lafortune & Lake, 1995). Despite the limitations of the human pendulum approach, the high level of control is beneficial in that it reduces the variability between trials; as well, the joint positions remain relatively constant and easy to replicate in a model. While this approach provided a means for an initial attempt to explore shock wave propagation and attenuation through the lower extremity, future work could potentially move towards modifying the THUMS model, or alternatively developing a new lower extremity and/or full body model, in order to better represent the body postures, kinematics, and kinetics of human gait, such as walking, running, or jumping (see the following discussion of passive muscle modelling in THUMS).

Although the THUMS model and finite element analysis provide a method to obtain and analyze bone accelerations within the lower extremity following impact, there

are some limitations inherent in the model. The AM-50 model, with specific height and weight parameters, is applicable only to a very small proportion of the male population, and may not necessarily apply to females; therefore, future work may involve simulations with other versions of the THUMS model, such as the AF-05 (5<sup>th</sup> percentile American female) or AM-95 (95<sup>th</sup> percentile American male) models. The fixed nature of the posture of the THUMS model is also limiting; the arms are fixed at approximately 30° from the horizontal when the model is oriented in a supine position, thereby possibly changing the inertial properties of the model from those seen experimentally. In the present study, this was addressed by maintaining the participant's shoulder angle at approximately 30° during impact. However, this posture is not representative of that seen during running. Should the THUMS model be adopted for further examination of shock wave propagation in the future, the arm posture of the model should be addressed to mimic the typical position of the arms during pendulum impacts (crossed across the chest or resting on the pendulum frame) or during running, depending on the approach used.

The method by which the additional mass of the pendulum was accounted for in the THUMS model may have contributed slightly to some of the differences between the experimental and model results. The extra mass was simply incorporated into structures within the torso by increasing the mass densities of two parts located within the torso. These two parts were bilaterally symmetrical, and were modelled as solids in order to represent the internal (visceral) soft tissues. However, this technique involved the assumption that the participant in the experimental protocol was rigidly constrained to the pendulum, and that no relative movement between the participant and the pendulum occurred. In addition, by strapping the participant to the pendulum in the experimental protocol, potential movements at the hip and knee joints were constrained, in order to

increase the level of control over initial impact conditions. However, the model's hip and knee joints were not constrained, thereby allowing for movements at these joints which may not have been possible experimentally. Should it be desired in future work to employ the human pendulum approach, an attempt should be made to include a rigid body along the back of the model to represent the pendulum, and use a material model such as MAT\_B01 (MAT\_SEATBELT) to secure the model to the pendulum, in order to constrain some of the joint movements of the model.

Additionally, the sparsity of the tissues incorporated around the ankle joint in the full body THUMS model may have posed some limitations to the examination of shock wave propagation through the lower extremity. The original version of the THUMS model incorporated a shoe structure inferior to the foot bones, but there was no identifiable structure to represent the heel pad. In the experimental protocol, the participant underwent barefoot impacts, and as the heel pad has been found to contribute substantially to energy dissipation following impact (up to 95% (Pain & Challis, 2001)), it was necessary to make an attempt to alter the shoe, thereby resulting in behaviour that was more representative of a human heel pad. An initial attempt was made to alter both the material properties and geometry of the shoe, based on those characteristics of in vivo heel pads that have been reported in the literature (Aerts & De Clercq, 1993; Gefen et al., 2001; Wearing et al., 2009). Although this appeared to reduce the peak accelerations at the tibia to a reasonable magnitude relative to what is typically seen in vivo, the impact forces were also reduced to far less than the range of 1.8-2.8 times body weight that is typically cited for human pendulum impacts (Duquette & Andrews, 2010a, b; Flynn et al., 2004; Holmes & Andrews, 2006; Schinkel-Ivy et al., 2010).

Given that the dependent force and acceleration variables output from the full body THUMS model appeared to be relatively sensitive to the characteristics of the shoe of the model, it seems warranted that future work should encompass a closer examination of the THUMS shoe structure, as well as either in vitro or in vivo experimentation to document the necessary characteristics of heel pad specimens. Primarily, the geometry of the shoe should be addressed in order to better represent that of a heel pad; the current geometry is essentially flat along the bottom of the shoe, while a human heel pad wraps around the inferior aspect of the calcaneus, thereby reducing the surface area that contacts the ground or force plate during impact. Further, the current shoe geometry of the model extends several millimetres past the edges of the foot bones on all sides, thereby providing additional surface area during impact. In order to alter the geometry of the shoe structure, the nodal coordinates of the existing nodes along the inferior surface of the shoe could be modified. Alternatively, the existing shoe structure could be removed from the model, and an entirely new heel pad structure created in its place. Using either approach, modifications of the shoe geometry to better represent that of a heel pad may contribute to improved agreement between the experimental and model force- and acceleration-time histories, especially with respect to the times to peak force and acceleration, which are substantially shorter for the model than for the experimental data.

Finally, the purely passive characteristics of the muscles in the full body THUMS model do not reflect the active nature of human muscle. As THUMS was developed to simulate an occupant's response to an automobile impact, the muscles are modelled passively. In scenarios involving rapid loading, such as an automobile impact, it takes approximately 220 ms for muscles to produce force (Pope et al., 1979), which does not occur quickly enough to provide joint protection (Kang et al., 2005; Pope et al., 1979).

Therefore, the assumption was made for the THUMS model that the occupant does not have sufficient time to react to an automobile impact and initiate muscle activation, which is often assumed for human numerical models of automobile collisions (Behr et al., 2006). Passive modelling enables the muscle tissues to modify the impact between the bone and external surface (Mukherjee et al., 2007), but does not account for changes in muscle activation that may occur during impact. However, muscle forces act to maintain posture and modify loads in the joints and ligaments (Mukherjee et al., 2007). This effect would likely be more pronounced during a human locomotion activity such as running, in which some level of muscle activation is necessary in order to swing the lower extremity through its range of motion, and support the body's weight during the stance phase.

In the experimental component of the present study, it was not possible for the participant to avoid activation of the shank musculature, as a certain level of activation was necessary for maintaining the desired angle of dorsiflexion at the ankle. This was addressed by providing visual feedback of the activation level of the tibialis anterior, so that the participant maintained a specific percentage of their MVE through the impact. Although the activation levels of the TA and LG muscles were maintained at a relatively consistent level across all of the experimental impact trials, differences in the stiffness of the human and model shank soft tissue may have contributed to some of the differences noted for the impact force and tibial acceleration variables. Further, as muscle activation increases joint stability (at the hip, for example), the lack of muscle activation in the full body THUMS model may have contributed to the joint movements observed for both versions of the model following impact.

In order to improve the biological fidelity of the THUMS model for running-type impacts, in which muscle activation is necessary within the lower extremity, it would be

beneficial to incorporate active muscle properties into the model. The incorporation of active muscle properties would increase the stiffness of body segments and joints, and would also enable pre-loading of the joints prior to impact. Past studies have indicated that the incorporation of active muscle properties have a substantial effect following a lateral knee impact, such as that applied to a pedestrian's knee following impact by a vehicle bumper (Soni et al., 2009). Muscle contractions resulted in reduced peak strain in the knee ligaments, increased von Mises stresses in the tibia and fibula, and increased effective stiffness at the knee joint in lateral bend (Soni et al., 2009). It would be expected that similar results would be seen in the full body THUMS model for running-type impacts, specifically increased joint stiffness, and as a result, reduced movements at the joints. However, the incorporation of active muscle properties into the full body THUMS model has yet to be attempted, and the question of whether this task can be accomplished appropriately in THUMS remains to be answered.

Potentially, the stiffness of the lower extremity soft tissue components could be altered, as muscle activation results in increased muscle stiffness (Latash & Zatsiorsky, 1993), although this may not adequately represent the dynamic nature of muscle contraction. Alternatively, Hill-type muscle models with active muscle properties are available in LS-DYNA, as material models S15 (MAT\_S15 or MAT\_SPRING\_MUSCLE) and 156 (MAT\_156 or MAT\_MUSCLE) (LSTC, 2007). The material behaviours of these models are adapted from Hill (1938), whose model is still widely used today for the modelling of musculoskeletal dynamics (LSTC, 2007). MAT\_S15 incorporates the force, length, and shortening velocity of the modelled muscle, while MAT\_156 replaces these variables with stress, strain, and strain rate (LSTC, 2007). However, as MAT\_S15 and MAT\_156 only apply to discrete elements (springs and

dampers) and truss elements, respectively (LSTC, 2007), these material models may not be appropriate to apply to the masses of soft tissues in the lower extremity, which are modelled as solid elements. Therefore, future work should address whether active muscle properties can be appropriately incorporated into the full body THUMS model, or if the development of a new lower extremity and/or full body model provides a better solution.

## *Chapter 7*

### *Conclusion*

In conclusion, in the first phase of the present study, an attempt was made to investigate the validity of the Total HUMAN Model for Safety in response to running-type impacts. It was concluded that although further work may be necessary to improve certain aspects of the THUMS model for this type of impact, there is certainly potential for the use of this type of model to investigate the propagation and attenuation of shock waves through the lower extremity. Through the modification of the material properties and geometry of the THUMS shoe, the resulting force-time histories following impact agreed relatively well with those produced experimentally through human pendulum impacts. Further, the peak accelerations that were measured at the tibia of the model fell within the range of those in the literature. The second phase of the study indicated that the model simulated, to a certain extent, the shock wave phenomenon along the length of the tibia in response to impact. Additionally, the tibia and knee joint also exhibited attenuation of the shock wave as it propagates proximally, which is promising for future investigations into the stresses within the lower extremity in response to impact, and the relation between these stresses and lower extremity overuse injuries.

*Appendix A*  
*Lower Extremity Material Models*

Material Model	Variable	Coefficient	Parts
MAT_012 ISOTROPIC_ ELASTIC_ PLASTIC	Mass density (RO)	999.9999	Cancellous bone: phalanges, metatarsals, cuneiforms, navicular, cuboid, calcaneus, talus
	Shear modulus (G)	2.53E+07	
	Yield stress (SIGY)	1.47E+06	
	Plastic hardening modulus (ETAN)	7.35E+07	
MAT_024 PIECEWISE_ LINEAR_ PLASTICITY	Bulk modulus, K (BULK)	2.45E+08	Cortical bone: phalanges, metatarsals, cuneiforms, navicular, cuboid, calcaneus, talus
	Mass density (RO)	2.00E+03	
	Young's modulus (E)	1.50E+10	
	Poisson's ratio (PR)	3.00E-01	
MAT_105 DAMAGE_2	Yield stress (SIGY)	2.24E+08	Cancellous bone (centre): tibia, fibula, femur
	Mass density (RO)	8.62E+02	
	Young's modulus (E)	4.00E+07	
	Poisson's ratio (PR)	4.50E-01	
	Yield stress (SIGY)	7.80E+06	
	Tangent modulus (ETAN)	1.33E+07	
	Failure flag (FAIL)	6.00E-02	
MAT_105 DAMAGE_2	Damage threshold (EPSD)	6.00E-02	Cancellous bone (end): tibia, fibula, femur
	Critical damage value (DC)	1.00E-10	
	Mass density (RO)	8.62E+02	
	Young's modulus (E)	1.60E+08	
	Poisson's ratio (PR)	4.50E-01	
	Yield stress (SIGY)	3.20E+07	
MAT_024 PIECEWISE_ LINEAR_ PLASTICITY	Tangent modulus (ETAN)	2.90E+07	Cortical bone: tibia (distal, centre, proximal)
	Failure flag (FAIL)	5.00E-01	
	Damage threshold (EPSD)	5.00E-01	
	Critical damage value (DC)	1.00E-10	
	Mass density (RO)	2.00E+03	
	Young's modulus (E)	1.80E+10	
	Poisson's ratio (PR)	3.00E-01	
MAT_024 PIECEWISE_ LINEAR_ PLASTICITY	Yield stress (SIGY)	3.61E+07	Cortical bone: fibula (distal, centre, proximal)
	Tangent modulus (ETAN)	1.48E+10	
	Failure flag (FAIL)	2.80E-02	
	Strain rate parameter (C)	3.61E+02	
	Strain rate parameter (P)	4.61E+00	
	Mass density (RO)	2.00E+03	
	Young's modulus (E)	1.85E+10	
MAT_024 PIECEWISE_ LINEAR_ PLASTICITY	Poisson's ratio (PR)	3.00E-01	Cortical bone: fibula (distal, centre, proximal)
	Yield stress (SIGY)	3.70E+07	
	Tangent modulus (ETAN)	1.67E+10	
	Failure flag (FAIL)	2.80E-02	
	Strain rate parameter (C)	3.61E+02	
	Strain rate parameter (P)	4.61E+00	

MAT_024	Mass density (RO)	2.00E+03	Cortical bone:
PIECEWISE_	Young's modulus (E)	1.73E+10	femur (distal,
LINEAR_	Poisson's ratio (PR)	3.00E-01	centre, proximal)
PLASTICITY	Yield stress (SIGY)	3.45E+07	
	Tangent modulus (ETAN)	1.56E+10	
	Failure flag (FAIL)	2.80E-02	
	Strain rate parameter (C)	3.61E+02	
	Strain rate parameter (P)	4.61E+00	
MAT_012	Mass density (RO)	999.9999	Cancellous bone:
ISOTROPIC_	Shear modulus (G)	2.54E+07	patella
ELASTIC_	Yield stress (SIGY)	1.00E+10	
PLASTIC	Plastic hardening modulus (ETAN)	2.54E+07	
	Bulk modulus, K (BULK)	2.45E+08	
MAT_012	Mass density (RO)	1.98E+03	Cartilage: patella
ISOTROPIC_	Shear modulus (G)	3.85E+08	
ELASTIC_	Yield stress (SIGY)	1.00E+10	
PLASTIC	Plastic hardening modulus (ETAN)	3.85E+08	
	Bulk modulus, K (BULK)	8.30E+08	
MAT_001	Mass density (RO)	2.00E+03	Cortical bone:
MAT_	Young's modulus (E)	1.03E+10	patella
ELASTIC	Poisson's ratio (PR)	3.00E-01	
MAT_001	Mass density (RO)	1.10E+03	Ligaments: deltoid,
MAT_	Young's modulus (E)	4.01E+08	anterior/posterior
ELASTIC	Poisson's ratio (PR)	4.90E-01	talofibular,
			calcaneo-fibular
MAT_001	Mass density (RO)	1.10E+03	Ligaments: anterior/
MAT_	Young's modulus (E)	5.30E+07	posterior
ELASTIC	Poisson's ratio (PR)	4.90E-10	tibiofibular, talus-
			calcaneus, cuboid-
			navicular-
			cuneiform, talus,
			calcaneo-navicular,
			talocalcaneum,
			posterior menisco-
			femoral, transverse
			Interosseous
			membrane
MAT_001	Mass density (RO)	1.00E+03	Ligament: cuboid-
MAT_	Young's modulus (E)	1.00E+08	navicular-cuneiform
ELASTIC	Poisson's ratio (PR)	3.00E-01	
MAT_001	Mass density (RO)	1.00E+03	Ligament: foot
MAT_	Young's modulus (E)	5.00E+07	
ELASTIC	Poisson's ratio (PR)	3.00E-01	
MAT_001	Mass density (RO)	1.00E+03	Ligament: long
MAT_	Young's modulus (E)	1.90E+09	plantar
ELASTIC	Poisson's ratio (PR)	3.00E-01	

MAT_001	Mass density (RO)	1.10E+03	Ligament: patellar,
MAT_	Young's modulus (E)	8.00E+08	quadriceps femoris
ELASTIC	Poisson's ratio (PR)	4.90E-01	
MAT_019	Mass density (RO)	1.10E+03	Ligaments:
STRAIN_	Young's modulus (E)	1.00E+00	tibial/fibular
RATE_	Poisson's ratio (PR)	4.90E-01	collateral, anterior/
DEPENDENT_	Load curve ID1	2.00E+00	posterior cruciate
PLASTICITY	Load curve ID2	3.00E+00	
	Load curve ID3	4.00E+00	
	Load curve ID4	5.00E+00	
MAT_B01	Mass per unit length (MPUL)	6.60E-02	Achilles tendon
SEATBELT	Minimum length (LMIN)	2.50E-03	
MAT_057	Mass density (RO)	1.00E+03	Menisci:
LOW_	Young's modulus (E)	1.20E+07	lateral/medial
DENSITY_	Tension cutoff stress (TC)	-	
FOAM		1.00E+20	
	Hysteretic unloading factor (HU)	6.00E-01	
	Viscous coefficient (DAMP)	1.00E-01	
	Shape factor (SHAPE)	8.00E+00	
MAT_006	Mass density (RO)	1.60E+03	Soft tissue: crural,
VISCO-	Elastic bulk modulus (BULK)	4.59E+06	knee, thigh
ELASTIC	Short-time shear modulus (G0)	7.01E+05	
	Long-time shear modulus (GI)	2.34E+05	
	Decay constant (BETA)	1.00E+02	
MAT_024	Mass density (RO)	1.60E+03	Skin: crural, knee,
PIECEWISE_	Young's modulus (E)	2.20E+07	thigh
LINEAR_	Poisson's ratio (PR)	4.00E-01	
PLASTICITY	Yield stress (SIGY)	6.86E+06	
MAT_002	Mass density (RO)	1.60E+03	Skin: knee
ORTHO-	Young's modulus in a-direction (EA)	4.40E+07	
TROPIC_	Young's modulus in b-direction (EB)	4.40E+07	
ELASTIC	Young's modulus in c-direction (EC)	2.20E+07	
	Poisson's ratio ba (PRBA)	4.00E-01	
	Poisson's ratio ca (PRCA)	1.00E-02	
	Poisson's ratio cb (PRCB)	1.00E-02	
	Shear modulus ab (GAB)	7.86E+06	
	Shear modulus bc (GBC)	7.86E+06	
	Shear modulus ca (GCA)	7.86E+06	

## Units

Variable	Unit
Bulk modulus	Pa
Decay constant	s <sup>-1</sup>
Elastic bulk modulus	Pa
Long-time shear modulus	Pa
Mass density	kg/m <sup>3</sup>
Mass per unit length	kg/m
Minimum length	m
Plastic hardening modulus	Pa
Poisson's ratio	Unitless
Shear modulus	Pa
Short-time shear modulus	Pa
Strain rate parameter	s <sup>-1</sup>
Tangent modulus	Pa
Tension cutoff stress	Pa
Viscous coefficient	Ns/m
Yield stress	Pa
Young's modulus	Pa

**Appendix B**  
**Left Lower Extremity Contact Algorithms and Coefficients**

Algorithm Number/ Name	Contact Algorithm	FS	FD	DC	VC	VDC	SOFT	SOF SCL
32: tibia top	CONTACT_TIED_NODES_TO_SURFACE_ID_OFFSET	0	0	0	0	0	-	-
33: tibia down	CONTACT_AUTOMATIC_SURFACE_TO_SURFACE_ID	0	0	0	0	0	-	-
34: ankle	CONTACT_AUTOMATIC_SURFACE_TO_SURFACE_ID	0	0	0	0	0	-	-
35: talus-calcaneus	CONTACT_AUTOMATIC_SURFACE_TO_SURFACE_ID	0	0	0	0	0	-	-
36: talus cort.-navicular cort.	CONTACT_AUTOMATIC_SURFACE_TO_SURFACE_ID	0	0	0	0	0	-	-
37: calcaneus cort.-cuboid cort.	CONTACT_AUTOMATIC_SURFACE_TO_SURFACE_ID	0	0	0	0	0	-	-
38: talus cort.-deltoid ligament	CONTACT_AUTOMATIC_SURFACE_TO_SURFACE_ID	0	0	0	0	0	1	0
39: navicular cort.-deltoid ligament	CONTACT_AUTOMATIC_SURFACE_TO_SURFACE_ID	0	0	0	0	0	1	0
40: ankle	CONTACT_AUTOMATIC_NODES_TO_SURFACE_ID	0	0	0	0	0	-	-
41: femur-patella	CONTACT_AUTOMATIC_SURFACE_TO_SURFACE_ID	0	0	0	0	0	1	0
42: femur-meniscus tibia	CONTACT_AUTOMATIC_SURFACE_TO_SURFACE_ID	0	0	0	0	0	1	0

43: femur-meniscus tibia 2	CONTACT_AUTOMATIC_SURFACE_TO_SURFACE_ID	0	0	0	0	20	1	0
44: tibia-meniscus	CONTACT_TIED_NODES_TO_SURFACE_ID	0	0	0	0	0	1	0
45: thigh-knee soft tissues	CONTACT_TIED_NODES_TO_SURFACE_ID	0	0	0	0	0	1	0
46: knee-crural soft tissues	CONTACT_TIED_NODES_TO_SURFACE_ID	0	0	0	0	0	1	0
47: knee bone-soft tissues	CONTACT_AUTOMATIC_SURFACE_TO_SURFACE_ID	0.1	0.1	0	0	0	1	0
48: knee bone-soft tissues 2	CONTACT_AUTOMATIC_SURFACE_TO_SURFACE_ID	0.1	0.1	0	0	0	1	0
49: knee bone-soft tissues 3	CONTACT_AUTOMATIC_SURFACE_TO_SURFACE_ID	0.1	0.1	0	0	0	1	0
50: knee bone-soft tissues 4	CONTACT_AUTOMATIC_SURFACE_TO_SURFACE_ID	0.1	0.1	0	0	0	1	0
51: knee bone-soft tissues 5	CONTACT_AUTOMATIC_SURFACE_TO_SURFACE_ID	0.1	0.1	0	0	0	1	0
52: knee bone-soft tissues 6	CONTACT_AUTOMATIC_SURFACE_TO_SURFACE_ID	0.1	0.1	0	0	0	1	0
53: between leg	CONTACT_AUTOMATIC_SURFACE_TO_SURFACE_ID	0.2	0.2	0	0	0	2	0
54: between leg 2	CONTACT_AUTOMATIC_SURFACE_TO_SURFACE_ID	0.2	0.2	0	0	0	-	-
55: between leg 3	CONTACT_AUTOMATIC_SURFACE_TO_SURFACE_ID	0.2	0.2	0	0	0	-	-
56: between leg 4	CONTACT_AUTOMATIC_SURFACE_TO_SURFACE_ID	0.2	0.2	0	0	0	-	-
57: foot-sole	CONTACT_TIED_NODES_TO_SURFACE_ID_OFFSET	0	0	0	0	0	-	-

58: LCL	CONTACT_AUTOMATIC_SURFACE_TO_SURFACE_ID	0.1	0.1	0	0	0	2	0
59: MCL	CONTACT_AUTOMATIC_SURFACE_TO_SURFACE_ID	0.1	0.1	0	0	0	2	0
60: patella	CONTACT_AUTOMATIC_SURFACE_TO_SURFACE_ID	0.1	0.1	0	0	0	1	0
61: patella	CONTACT_AUTOMATIC_SURFACE_TO_SURFACE_ID	0.1	0.1	0	0	0	1	0
62: knee ligament	CONTACT_AUTOMATIC_SINGLE_SURFACE_ID	0.1	0.1	0	0	0	-	-
63: knee ligament 2	CONTACT_AUTOMATIC_SINGLE_SURFACE_ID	0.1	0.1	0	0	0	-	-
64: MCL	CONTACT_SINGLE_EDGE_ID	0.1	0.1	0	0	0	-	-
65: ACL-PCL	CONTACT_SINGLE_EDGE_ID	0.1	0.1	0	0	0	-	-
66: femur-meniscus	CONTACT_SINGLE_EDGE_ID	0.1	0.1	0	0	0	-	-
69: hipbone upper-mid	CONTACT_TIED_NODES_TO_SURFACE_ID_OFFSET	0	0	0	0	0	-	-
70: hipbone mid-low	CONTACT_TIED_NODES_TO_SURFACE_ID_OFFSET	0	0	0	0	0	-	-
72: hipbone-pubic	CONTACT_TIED_NODES_TO_SURFACE_ID_OFFSET	0	0	0	0	0	1	0
74: hipbone-sacrum	CONTACT_TIED_NODES_TO_SURFACE_ID_OFFSET	0	0	0	0	0	1	0
76: femur-acetabulum	CONTACT_AUTOMATIC_SURFACE_TO_SURFACE_ID	0.01	0.01	0	0	0	-	-

**Appendix C**  
**Shoe Crush Simulation Contact Algorithm and Original and Modified Shoe Material Models**

**\*CONTACT\_SURFACE\_TO\_SURFACE Algorithm**

Variable	Coefficient
Static coefficient of friction	0.401355
Dynamic coefficient of friction	0.401355
Exponential decay coefficient (s <sup>-1</sup> )	0
Coefficient for viscous friction	0
Viscous damping coefficient (% of critical)	20.0
Scale factor on default slave penalty stiffness	1.0
Scale factor on default master penalty stiffness	1.0
Soft constraint option	2.0
Scale factor for constraint forces of soft constraint option	0.2

**Original Shoe Material Properties**

**\*MAT\_LOW\_DENSITY\_FOAM Coefficients**

Variable	Coefficient
Mass density (RO) (kg/m <sup>3</sup> )	999.9999 kg/m <sup>3</sup>
Young's modulus (E) (Pa)	8.9000E+06
Tension cut-off stress (TC) (Pa)	-9.5000E+06
Hysteretic unloading factor (HU)	0.0000
Decay constant (BETA) (s <sup>-1</sup> )	0.0000
Viscous coefficient (DAMP) (Ns/m)	0.0500
Shape factor (SHAPE)	0.0000
Failure option (FAIL)	Default
Bulk viscosity activation flag (BVFLAG)	Default
Optional Young's relaxation modulus (ED) (Pa)	Default
Optional decay constant (BETA1) (s <sup>-1</sup> )	Default
Stiffness coefficient for contact interface stiffness (KCON) (N/m)	Default
Reference geometry (REF)	Default

***Stress-Strain Loading Curve***

Strain	Stress (Pa)
0.000	0.00
0.075	3.34E+06
0.150	4.00E+06
0.250	4.47E+06
0.300	4.94E+06
0.375	6.00E+06
0.450	8.00E+06
0.525	1.40E+07
0.600	3.47E+07
0.700	1.00E+08

***Modified Shoe Material Properties***

***\*MAT\_LOW\_DENSITY\_FOAM Coefficients***

Variable	Coefficient
Mass density (RO) (kg/m <sup>3</sup> )	999.9999
Young's modulus (E) (Pa)	4.7429E+05
Tension cut-off stress (TC) (Pa)	1.0000E+20
Hysteretic unloading factor (HU)	0.0100
Decay constant (BETA) (s <sup>-1</sup> )	0.0000
Viscous coefficient (DAMP) (Ns/m)	0.3000
Shape factor (SHAPE)	8.0000
Failure option (FAIL)	Default
Bulk viscosity activation flag (BVFLAG)	Default
Optional Young's relaxation modulus (ED) (Pa)	Default
Optional decay constant (BETA1) (s <sup>-1</sup> )	Default
Stiffness coefficient for contact interface stiffness (KCON) (N/m)	Default
Reference geometry (REF)	Default

***Stress-Strain Loading Curve***

Strain	Stress (Pa)
0.00	0.00
0.40	1.98E+05
0.50	3.00E+05
0.55	3.80E+05
0.60	4.90E+05
0.65	6.20E+05
0.70	7.60E+05
0.75	9.10E+05
0.80	1.10E+06
0.85	1.30E+06
0.90	1.60E+06

## Appendix D

### Contact Algorithm Modifications for Full Body Impact Simulations

Version #	Modification
1	<ul style="list-style-type: none"><li>– *HOURGLASS; hourglass control type and hourglass coefficient set as 1 and 0.1</li><li>– Soft constraint option and scale factor for constraint forces of soft constraint option changed to 2.0 (segment-based contact) and 0.2 for contact algorithms 8000077, -78, -79, -80, -81, -82, -83, -128, -131, -133, -143, -171</li><li>– Scale factors for default slave and master penalty stiffnesses changed to 0.01 and 0.01 for contact algorithms 8000083, -126, -129, -157, 8100173, -175 Penalty scale factor, activation factor, and formulation for interior contact in *CONTACT_INTERIOR changed to 0.01, 0.9, and 2.0 (combined shear and compression) for parts 8400120, 8400210, 8580200, 8580300</li><li>– Element formulation changed to 3 for part 8921000</li></ul>
2	<ul style="list-style-type: none"><li>– *HOURGLASS; hourglass control type and hourglass coefficient set as 1 and 0.1</li><li>– Soft constraint option and scale factor for constraint forces of soft constraint option changed to 2.0 (segment-based contact) and 0.2 for contact algorithms 8000077, -78, -79, -80, -81, -82, -83, -128, -131, -133, -143, -171</li><li>– Scale factors for default slave and master penalty stiffnesses changed to 0.1 and 0.1 for contact algorithms 8000083, -126, -129, -157, 8100173, -175</li><li>– Penalty scale factor, activation factor, and formulation for interior contact in *CONTACT_INTERIOR changed to 0.01, 0.9, and 2.0 (combined shear and compression) for parts 8400120 and 8580200</li><li>– Penalty scale factor, activation factor, and formulation for interior contact in *CONTACT_INTERIOR changed to 0.005, 0.95, and 2.0 (combined shear and compression) for part 8720310</li></ul>
3	<ul style="list-style-type: none"><li>– *HOURGLASS; hourglass control type and hourglass coefficient set as 1 and 0.1</li><li>– Soft constraint option and scale factor for constraint forces of soft constraint option changed to 2.0 (segment-based contact) and 0.2 for contact algorithms 8000077, -78, -79, -80, -81, -82, -83, -128, -131, -133, -143, -171</li><li>– Scale factors for default slave and master penalty stiffnesses changed to 0.1 and 0.1 for contact algorithms 8000083, -126, -129, -157, 8100173, -175</li><li>– Penalty scale factor, activation factor, and formulation for interior contact in *CONTACT_INTERIOR changed to 0.01, 0.9, and 2.0 (combined shear and compression) for parts 8400120 and 8580200</li></ul>

## References

- Aerts, P. & De Clercq, D. (1993). Deformation characteristics of the heel region of the shod foot during a simulated heel strike: The effect of varying midsole hardness. *Journal of Sports Sciences*, 11, 449-461.
- Aerts, P., Ker, R.F., De Clercq, D., Ilesley, D.W., & Alexander, R.M. (1995). The mechanical properties of the human heel pad: A paradox resolved. *Journal of Biomechanics*, 28(11), 1299-1308.
- Andrews, D.M. & Dowling, J.J. (2000). Mechanical modeling of tibial axial accelerations following impulsive heel impact. *Journal of Applied Biomechanics*, 16, 276-288.
- Bandak, F.A., Tannous, R.E., & Toridis, T. (2001). On the development of an osseoligamentous finite element model of the human ankle joint. *International Journal of Solids and Structures*, 38, 1681-1697.
- Becker, A.A. (2004). *An introductory guide to finite element analysis*. New York: ASME Press.
- Behr, M., Arnoux, P.J., Serre, T., Thollon, L., & Brunet, C. (2006). Tonic finite element model of the lower limb. *Journal of Biomechanical Engineering*, 128, 223-228.
- Beillas, P., Papaioannou, G., Tashman, S., & Yang, K.H. (2004). A new method to investigate in vivo knee behaviour using a finite element model of the lower limb. *Journal of Biomechanics*, 37, 1019-1030.
- Bennett, M.B., & Ker, R.F. (1990). The mechanical properties of the human subcalcaneal fat pad in compression. *Journal of Anatomy*, 171, 131-138.
- Bevill, G., Eswaran, S.K., Gupta, A., Papadopoulos, P., & Keaveny, T.M. (2006). Influence of bone volume fraction and architecture on computed large-deformation failure mechanisms in human trabecular bone. *Bone*, 39, 1218-1225.
- Bobbert, M.F., Yeadon, M.R., & Nigg, B.M. (1992). Mechanical analysis of the landing phase in heel-toe running. *Journal of Biomechanics*, 25, 223-234.
- Boyer, K.A. & Nigg, B.M. (2004). Muscle activity in the leg is tuned in response to impact force characteristics. *Journal of Biomechanics*, 37, 1583-1588.
- Boyer, K.A. & Nigg, B.M. (2006). Muscle tuning during running: Implications of an un-tuned landing. *Journal of Biomechanical Engineering*, 128, 815-822.
- Brown, T.D. (2004). Finite element modeling in musculoskeletal biomechanics. *Journal of Applied Biomechanics*, 20, 336-366.

- Burkhart, T.A., Arthurs, K.L., & Andrews, D.M. (2008). Reliability of upper and lower extremity anthropometric measurements and the effect on tissue mass predictions. *Journal of Biomechanics*, 41, 1604-1610.
- Burr, D.B., Martin, R.B., Schaffler, M.B., & Radin, E.L. (1985). Bone remodelling in response to in vivo fatigue microdamage. *Journal of Biomechanics*, 18(3), 189-200.
- Butler, R.J., Crowell III, H.P., & Davis, I.M. (2003). Lower extremity stiffness: Implications for performance and injury. *Clinical Biomechanics*, 18, 511-517.
- Cardinale, M. & Pope, M.H. (2003). The effects of whole body vibration on humans: Dangerous or advantageous? *Acta Physiologica Hungarica*, 90(3), 195-206.
- Cavanagh, P.R. & Lafortune, M.A. (1980). Ground reaction forces in distance running. *Journal of Biomechanics*, 13, 397-406.
- Cavanagh, P.R., Valiant, G.A., & Misevich, K.W. (1984). *Biological aspects of modelling shoe/foot interacting during running* (E.C. Fredericks, Ed.). Champaign, IL: Human Kinetics Publishers, 24-46.
- Challis, J.H. & Pain, M.T.G. (2008). Soft tissue motion influences skeletal loads during impacts. *Exercise and Sport Sciences Reviews*, 36(2), 71-75.
- Chang, W.R., Chang, C.C., Matz, S., & Lesch, M.F. (2008). A methodology to quantify the stochastic distribution of friction coefficient required for level walking. *Applied Ergonomics*, 39, 766-771.
- Chavet, P., Lafortune, M.A., & Gray, J.R. (1997). Asymmetry of lower extremity responses to external impact loading. *Human Movement Science*, 16, 391-406.
- Chawla, A., Mukherjee, S., & Karthikeyan, B. (2009). Characterization of human passive muscles for impact loads using genetic algorithm and inverse finite element models. *Biomechanics and Modeling in Mechanobiology*, 8, 67-76.
- Chen, W.P., Tang, F.T., & Ju, C.W. (2001). Stress distribution of the foot during mid-stance to push-off in barefoot gait: A 3-D finite element analysis. *Clinical Biomechanics*, 16, 614-630.
- Cheung, J.T.M., Zhang, M., Leung, A.K.L., & Fan, Y.B. (2005). Three-dimensional finite element analysis of the foot during standing – A material sensitivity study. *Journal of Biomechanics*, 38, 1045-1054.
- Chu, M.L., Yazdani-Ardakani, S., Gradisar, I.A., & Askew, M.J. (1986). An in vitro simulation study of impulsive force transmission along the lower skeletal extremity. *Journal of Biomechanics*, 19(12), 979-987.

- Clarys, J.P. & Marfell-Jones, M.J. (1986). Anthropometric prediction of component tissue masses in the minor limb segments of the human body. *Human Biology*, 58(5), 761-769.
- Clavert, P., Zerah, M., Krier, J., Mille, P., Kempf, J.F., & Kahn, J.L. (2006). Finite element analysis of the strain distribution in the humeral head tubercles during abduction: comparison of young and osteoporotic bone. *Surgical and Radiologic Anatomy*, 28, 581-587.
- Cole, G.K., Nigg, B.M., van den Bogert, A.J., & Gerritsen, K.G.M. (1996). Lower extremity joint loading during impact in running. *Clinical Biomechanics*, 11(4), 181-193.
- Cook, R.D., Malkus, D.S., Plesha, M.E., & Witt, R.J. (2002). *Concepts and applications of finite element analysis* (4<sup>th</sup> ed.). New York: John Wiley & Sons.
- Dagan, D., Be'ery, M., & Gefen, A. (2004). Single-trabecula building block for large-scale finite element models of cancellous bone. *Medical and Biological Engineering and Computing*, 42, 549-556.
- Dar, F.H., Meakin, J.R., & Aspden, R.M. (2002). Statistical methods in finite element analysis. *Journal of Biomechanics*, 35, 1155-1161.
- Dawson, J.M., Khmelniker, B.V., & McAndrew, M.P. (1999). Analysis of the structural behaviour of the pelvis during lateral impact using the finite element method. *Accident Analysis and Prevention*, 31, 109-119.
- De Clercq, D., Aerts, P., & Kunnen, M. (1994). The mechanical characteristics of the human heel pad during foot strike in running: An in vivo cineradiographic study. *Journal of Biomechanics*, 27(10), 1213-1222.
- Derrick, T.R., Caldwell, G.E., & Hamill, J. (2000). Modeling the stiffness characteristics of the human body while running with various stride lengths. *Journal of Applied Biomechanics*, 16, 36-51.
- Derrick, T.R., Hamill, J., & Caldwell, G.E. (1998). Energy absorption of impacts during running at various stride lengths. *Medicine & Science in Sports & Exercise*, 30(1), 128-135.
- Dickinson, J.A., Cook, S.D., & Leinhardt, T.M. (1985). The measurement of shock waves following heel strike while running. *Journal of Biomechanics*, 18(6), 415-422.
- Dufek, J.S. & Bates, B.T. (1991). Biomechanical factors associated with injury during landing in jump sports. *Sports Medicine*, 12(5), 326-337.
- Dufek, J.S., Mercer, J.A., & Griffin, F.R. (2009). The effects of speed and surface compliance on shock attenuation characteristics for male and female runners. *Journal of Applied Biomechanics*, 25, 219-228.

- Dumont, E.R., Grosse, I.E., & Slater, G.J. (2009). Requirements for comparing the performance of finite element models of biological structures. *Journal of Theoretical Biology*, 256, 96-103.
- Duquette, A.M. & Andrews, D.M. (2010a). Comparing methods of quantifying tibial acceleration slope. *Journal of Applied Biomechanics*, 2, 229-233.
- Duquette, A.M. & Andrews, D.M. (2010b). Tibialis anterior muscle fatigue leads to changes in tibial axial acceleration after impact when ankle dorsiflexion angles are visually controlled. *Human Movement Science*, 29, 567-577.
- Ferris, D.P. & Farley, C.T. (1997). Interaction of leg stiffness and surface stiffness during human hopping. *Journal of Applied Physiology*, 82(1), 15-22.
- Flynn, J.M., Holmes, J.D., & Andrews, D.M. (2004). The effect of localized leg muscle fatigue on tibial impact acceleration. *Clinical Biomechanics*, 19, 726-732.
- Fukuda, Y., Takai, S., Yohino, N., Murase, K., Tsutsumi, S., Ikeuchi, K., et al. (2000). Impact load transmission of the knee joint-influence of leg alignment and the role of meniscus and articular cartilage. *Clinical Biomechanics*, 15, 516-521.
- Gefen, A., Megido-Ravid, M., & Itzchak, Y. (2001). In vivo biomechanical behaviour of the human heel pad during the stance phase of gait. *Journal of Biomechanics*, 34, 1661-1665.
- Gefen, A., Megido-Ravid, M., Itzchak, Y., & Arcan, M. (2000). Biomechanical analysis of the three-dimensional foot structure during gait: A basic tool for clinical applications. *Journal of Biomechanical Engineering*, 122, 630-639.
- Gerritsen, K.G.M., van den Bogert, A.J., & Nigg, B.M. (1995). Direct dynamics simulation of the impact phase in heel-toe running. *Journal of Biomechanics*, 28(6), 661-668.
- Gittoes, M.J.R., Brewin, M.A., & Kerwin, D.G. (2006). Soft tissue contributions to impact forces simulated using a four-segment wobbling mass model of forefoot-heel landings. *Human Movement Science*, 25, 775-787.
- Gittoes, M.J.R. & Kerwin, D.G. (2009). Interactive effects of mass proportions and coupling properties on external loading in simulated forefoot impact landings. *Journal of Applied Biomechanics*, 25, 238-246.
- Goh, J.C.H., Lee, P.V.S., Toh, S.L., & Ooi, C.K. (2005). Development of an integrated CAD-FEA process for below-knee prosthetic sockets. *Clinical Biomechanics*, 20, 623-629.
- Granata, K.P., Padua, D.A., & Wilson, S.E. (2002). Gender differences in active musculoskeletal stiffness. Part II. Quantification of leg stiffness during functional hopping tasks. *Journal of Electromyography and Kinesiology*, 12, 127-135.

- Gray, H.A., Taddei, F., Zavatsky, A.B., Cristofolini, L., & Gill, H.S. (2008). Experimental validation of a finite element model of a human cadaveric tibia. *Journal of Biomechanical Engineering*, 130, 031016-1 – 9.
- Grimal, Q., Gama, B.A., Naili, S., Watzky, A., & Gillespie Jr., J.W. (2004). Finite element study of high-speed blunt impact on thorax: Linear elastic considerations. *International Journal of Impact Engineering*, 30, 665-683.
- Grimston, S.K., Engsberg, J.R., Kloiber, R., & Hanley, D.A. (1991). Bone mass, external loads, and stress fracture in female runners. *International Journal of Sport Biomechanics*, 7, 293-302.
- Gruber, K., Ruder, H., Denoth, J., & Schneider, K. (1998). A comparative study of impact dynamics: Wobbling mass model versus rigid body models. *Journal of Biomechanics*, 31, 439-444.
- Hamill, J., Derrick, T.R., & Holt, K.G. (1995). Shock attenuation and stride frequency during running. *Human Movement Science*, 14, 45-60.
- Helgason, B., Taddei, F., Palsson, H., Schileo, E., Cristofolini, L., Viceconti, M., et al. (2008). A modified method for assigning material properties to FE models of bones. *Medical Engineering & Physics*, 30, 444-453.
- Hernandez, C.J. & Keaveny, T.M. (2006). A biomechanical perspective on bone quality. *Bone*, 39, 1173-1181.
- Hill, A.V. (1938). The heat of shortening and the dynamic constants of muscle. *Proceedings of the Royal Society of London B*, 126(843), 136-195.
- Holmes, A.M. & Andrews, D.M. (2006). The effect of leg muscle activation state and localized muscle fatigue on tibial response during impact. *Journal of Applied Biomechanics*, 22, 275-284.
- Humphrey, J.D. (2002). Continuum biomechanics of soft biological tissues. *Royal Society of London Proceedings Series A*, 175, 1-44.
- Interactive Functional Anatomy. Primal Pictures, Inc., London, U.K., version 3.21.
- Iwamoto, M., Nakahira, Y., Tamura, A., Kimpara, H., Watanabe, I., & Miki, K. (2007). Development of advanced human models in THUMS. *6<sup>th</sup> European LS-DYNA Users' Conference*.
- Iwamoto, M., Omori, K., Kimpara, H., Nakahira, Y., Tamura, A., Watanabe, I., et al. (2003). Recent advances in THUMS: development of individual internal organs, brain, small female, and pedestrian model. *4<sup>th</sup> European LS-DYNA Users' Conference*.

- Jin, S.Y., Majumder, A., Altenhof, W., & Green, D. (2010). Axial cutting of AA6061-T6 circular extrusions under impact using single- and dual-cutter configurations. *International Journal of Impact Engineering*, 37, 735-753.
- Johansson, T., Meier, P., & Blickhan, R. (2000). A finite-element model for the mechanical analysis of skeletal muscles. *Journal of Theoretical Biology*, 206, 131-149.
- Jones, B.H., Bovee, M.W., Harris III, J.M., & Cowan, D.N. (1993). Intrinsic risk factors for exercise-related injuries among male and female army trainees. *American Journal of Sports Medicine*, 21(5), 705-710.
- Jorgensen, U. & Bojsen-Moller, F. (1989). Shock absorbency of factors in the shoe/heel interaction – with special focus on the role of the heel pad. *Foot Ankle*, 9(11), 294-299.
- Kang, Y.B., Jung, D.Y., Tanaka, M., Yshino, N., Tsutsumi, S., & Ikeuchi, D. (2005). Numerical analysis of three-dimensional cervical behaviours in posterior-oblique car collisions using 3-D human whole body finite element model. *JSME International Journal*, 48(4), 598-606.
- Keaveny, T.M., Morgan, E.F., Niebur, G.L., & Yeh, O.C. (2001). Biomechanics of trabecular bone. *Annual Review of Biomedical Engineering*, 3, 307-333.
- Kim, N.H. & Sankar, B.V. (2009). *Introduction to finite element analysis and design*. New York: Wiley.
- Kinoshita, H., Ogawa, T., Kuzuhara, K., & Ikuta, K. (1993). In vivo examination of the dynamic properties of the human heel pad. *International Journal of Sports Medicine*, 14(6), 312-319.
- Kitagawa, Y., Yasuki, T., & Hasegawa, J. (2008). Research study on neck injury lessening with active head restraint using human body FE model. *Traffic Injury Prevention*, 9(6), 574-582.
- Kumaresan, S., Yoganandan, N., & Pintar, F.A. (1999). Finite element analysis of the cervical spine: A material property sensitivity study. *Clinical Biomechanics*, 14, 41-53.
- Lafortune, M.A. (1991). Three-dimensional acceleration of the tibia during walking and running. *Journal of Biomechanics*, 24(10), 877-886.
- Lafortune, M.A., Hennig, E.M., & Lake, M.J. (1996a). Dominant role of interface over knee angle for cushioning impact loading and regulating initial leg stiffness. *Journal of Biomechanics*, 29(12), 1523-1529.
- Lafortune, M.A., & Lake, M.J. (1995). Human pendulum approach to simulate and quantify locomotor impact loading. *Journal of Biomechanics*, 28(9), 1111-1114.

- Lafortune, M.A., Lake, M.J., & Hennig, E.M. (1995). Transfer function between tibial acceleration and ground reaction force. *Journal of Biomechanics*, 28(1), 113-117.
- Lafortune, M.A., Lake, M.J., & Hennig, E.M. (1996b). Differential shock transmission response of the human body to impact severity and lower limb posture. *Journal of Biomechanics*, 12, 1531-1537.
- Latash, M.L. & Zatsiorsky, V.M. (1993). Joint stiffness: Myth or reality? *Human Movement Science*, 12, 653-692.
- Liacouras, P.C. & Wayne, J.S. (2007). Computational modeling to predict mechanical function of joints: Application to the lower leg with simulation of two cadaver studies. *Journal of Biomechanical Engineering*, 129, 811-817.
- Light, L.H., McLellan, G.E., & Klenerman, L. (1980). Skeletal transients on heel strike in normal walking with different footwear. *Journal of Biomechanics*, 13, 477-480.
- Limbert, G., Taylor, M., & Middleton, J. (2004). Three-dimensional finite element modelling of the human ACL: Simulation of passive knee flexion with a stressed and stress-free ACL. *Journal of Biomechanics*, 37, 1723-1731.
- Liu, W. & Nigg, B.M. (2000). A mechanical model to determine the influence of masses and mass distribution on the impact force during running. *Journal of Biomechanics*, 33, 219-224.
- Lotz, J.C., Cheal, E.J., & Hayes, W.C. (1991). Fracture prediction for the proximal femur using finite element models: Part I – Linear analysis. *Journal of Biomechanical Engineering*, 113, 353-360.
- LS-DYNA keyword user's manual, version 971. (2007). Livermore Software Technology Corporation.
- Lu, X.L. & Mow, V.C. (2008). Biomechanics of articular cartilage and determination of material properties. *Medicine & Science in Sports & Exercise*, 40(2), 193-199.
- Maeno, T. & Hasegawa, J. (2001). Development of a finite element model of the Total Human Model for Safety (THUMS) and application to car-pedestrian impacts. *17th International Technical Conference on the Enhanced Safety of Vehicles*.
- McGill, S.M., Thorstensson, A., & Norman, R.W. (1989). Non-rigid response of the trunk to dynamic axial loading: An evaluation of current modelling assumptions. *Clinical Biomechanics*, 4, 45-50.
- McKeag, D.B. & Dolan, C. (1989). Overuse syndromes of the lower extremity. *The Physician and Sports Medicine*, 17(7), 108-123.
- McMahon, T.A., Valiant, G., & Frederick, E.C. (1987). Groucho running. *Journal of Applied Physiology*, 62(6), 2326-2337.

- Mercer, J.A., Bates, B.T., Dufek, J.S., & Hreljac, A. (2003a). Characteristics of shock attenuation during fatigued running. *Journal of Sports Sciences*, 21, 911-919.
- Mercer, J.A., Devita, P., Derrick, T.R., & Bates, B.T. (2003b). Individual effects of stride length and frequency on shock attenuation during running. *Medicine & Science in Sports & Exercise*, 35(2), 307-313.
- Mercer, J.A., Vance, J., Hreljac, A., & Hamill, J. (2002). Relationship between shock attenuation and stride length during running at different velocities. *European Journal of Applied Physiology*, 87, 403-408.
- Merz, B., Niederer, P., Muller, R., & Ruegsegger, P. (1996). Automated finite element analysis of excised human femora based on precision-QCT. *Journal of Biomechanical Engineering*, 118, 387-390.
- Messina, D.F., Farney, W.C., & DeLee, J.C. (1999). The incidence of injury in Texas high school basketball. *American Journal of Sports Medicine*, 27(3), 294-299.
- Miller, R.H. & Hamill, J. (2009). Computer simulation of the effects of shoe cushioning on internal and external loading during running impacts. *Computer Methods in Biomechanics and Biomedical Engineering*, 12(4), 481-490.
- Miller-Young, J.E., Duncan, N.A., & Baroud, G. (2002). Material properties of the human calcaneal fat pad in compression: Experiment and theory. *Journal of Biomechanics*, 35, 1523-1531.
- Milner, C.E., Ferber, R., Pollard, C.D., Hamill, J., & Davis, I.S. (2006). Biomechanical factors associated with tibial stress fracture in female runners. *Medicine and Science in Sports and Exercise*, 38(2), 323-328.
- Milner, C.E., Hamill, J., & Davis, I. (2007). Are knee mechanics during early stance related to tibial stress fracture in runners? *Clinical Biomechanics*, 22, 697-703.
- Mizrahi, J., Verbitsky, O., & Isakov, E. (2000). Fatigue-related loading imbalance on the shank in running: A possible factor in stress fractures. *Annals of Biomedical Engineering*, 28, 463-469.
- Mizrahi, J., Voloshin, A., Russek, D., Verbitsky, O., & Isakov, E. (1997). The influence of fatigue on EMG and impact acceleration in running. *Basic and Applied Myology*, 7(2), 111-118.
- Mukherjee, S., Chawla, A., Karthikeyan, B., & Soni, A. (2007). Finite element crash simulations of the human body: Passive and active muscle modelling. *Sadhana*, 32(4), 409-426.
- Nagasaka, K., Mizuno, K., Tanaka, E., Yamamoto, S., Iwamoto, M., Miki, K., et al. (2003). Finite element analysis of knee injury risks in car-to-pedestrian impacts. *Traffic Injury Prevention*, 4(4), 345-354.

- Nambu, S.N. & Lewis, G. (2004). Influences of the temporal nature of the applied load and the tibial baseplate material on the stress distribution in a three-dimensional model of the human knee joint containing a prosthetic replacement. *Bio-Medical Materials and Engineering*, 14, 203-217.
- Nigg, B.M., Bahlsen, H.A., Luethi, S.M., & Stokes, S. (1987). The influence of running velocity and midsole hardness on external impact forces in heel-toe running. *Journal of Biomechanics*, 20, 951-959.
- Nigg, B.M., Cole, G.K., & Bruggeman, G.P. (1995). Impact forces during heel-toe running. *Journal of Applied Biomechanics*, 11, 407-432.
- Nigg, B.M. & Liu, W. (1999). The effect of muscle stiffness and damping on simulated impact force peaks during running. *Journal of Biomechanics*, 32, 849-856.
- Nigg, B.M., Stefanyshyn, D., Cole, G., Stergiou, P., & Miller, J. (2003). The effect of material characteristics of shoe soles on muscle activation and energy aspects during running. *Journal of Biomechanics*, 36, 569-575.
- Oberkampf, W.L. & Trucano, T.G. (2002). Verification and validation in computational fluid dynamics. *Progress in Aerospace Sciences*, 38, 209-272.
- Oshita, F., Omori, K., Nakashira, Y., & Miki, K. (2002). Development of a finite element model of the human body. *7<sup>th</sup> International LS-DYNA Users Conference*.
- Pain, M.T.G. & Challis, J.H. (2001). The role of the heel pad and shank soft tissue during impacts: A further resolution of a paradox. *Journal of Biomechanics*, 34, 327-333.
- Pain, M.T.G. & Challis, J.H. (2002). Soft tissue motion during impacts: Their potential contributions to energy dissipation. *Journal of Applied Biomechanics*, 18, 231-242.
- Pain, M.T.G. & Challis, J.H. (2004). Wobbling mass influence on impact ground reaction forces: A simulation model sensitivity analysis. *Journal of Applied Biomechanics*, 20, 309-316.
- Pain, M.G.T. & Challis, J.H. (2006). The influence of soft tissue movement on ground reaction forces, joint torques and joint reaction forces in drop landings. *Journal of Biomechanics*, 39, 119-124.
- Papaioannou, G., Nianios, G., Mitrogiannis, C., Fyhrie, D., Tashman, S., & Yang, K.H. (2008). Patient-specific knee joint finite element model validation with high-accuracy kinematics from biplane dynamic Roentgen stereogrammetric analysis. *Journal of Biomechanics*, 41, 2633-2638.
- Peasgood, M., Kubica, E., & McPhee, J. (2007). Stabilization of a dynamic walking gait simulation. *Journal of Computational and Nonlinear Dynamics*, 2, 65-72.

- Pelker, R.P. & Saha, S. (1983). Stress wave propagation in bone. *Journal of Biomechanics*, 16(7), 481-489.
- Pope, M.H., Johnson, R.J., Brown, D.W., & Tighe, C. (1979). The role of musculature in injuries to the medial collateral ligament. *Journal of Bone & Joint Surgery*, 61(3), 398-402.
- Portnoy, S., Yarnitzky, G., Yizhar, Z., Kristal, A., Oppenheim, U., Siev-Ner, I., et al. (2006). Real-time patient-specific finite element analysis of internal stresses in the soft tissues of a residual limb: A new tool for prosthetic fitting. *Annals of Biomedical Engineering*, 35(1), 120-135.
- Puso, M.A. & Weiss, J.A. (1998). Finite element implementation of anisotropic quasi-linear viscoelasticity using a discrete spectrum approximation. *Journal of Biomechanical Engineering*, 120, 62-70.
- Radin, E.L., Parker, H.G., Pugh, J.W., Steinberg, R.S., Paul, I.L., & Rose, R.M. (1973). Response of joints to impact loading – III. *Journal of Biomechanics*, 6, 51-57.
- Rome, K., Campbell, R.S.D., Flint, A.A., & Haslock, I. (1998). Ultrasonic heel pad thickness measurements: A preliminary study. *The British Journal of Radiology*, 71, 1149-1152.
- SAE J211/1 Instrumentation for Impact Test. Part I. Electronic Instrumentation. (2003). Society of Automotive Engineers, Warrendale, PA.
- Schinkel-Ivy, A., Burkhart, T.A., & Andrews, D.M. (2010, in press). Leg tissue mass composition affects tibial acceleration response following impact. *Journal of Applied Biomechanics*.
- Serink, M.T., Nachemson, A., & Hansson, G. (1977). The effect of impact loading on rabbit knee joints. *Acta Orthopaedica Scandinavica*, 48, 250-262.
- Shen, W., Niu, Y., Mattrey, R.F., Fournier, A., Corbeil, J., Kono, Y., et al. (2008). Development and validation of subject-specific finite element models for blunt trauma study. *Journal of Biomechanical Engineering*, 130, 021022-1 – 13.
- Song, Y., Debski, R.E., Musahl, V., Thomas, M., & Woo, S.L.Y. (2004). A three-dimensional finite element model of the human anterior cruciate ligament: A computational analysis with experimental validation. *Journal of Biomechanics*, 37, 383-390.
- Soni, A., Chawla, A., Mukherjee, S., & Malhotra, R. (2009). Response of lower limb in full-scale car-pedestrian low-speed lateral impact – influence of muscle contraction. *International Journal of Crashworthiness*, 14(4), 339-348.

- Spears, I.R. & Miller-Young, J.E. (2006). The effect of heel-pad thickness and loading protocol on measured heel-pad stiffness and a standardized protocol for inter-subject comparability. *Clinical Biomechanics*, 21, 204-212.
- Spears, I.R., Miller-Young, J.E., Waters, M., & Rome, K. (2005). The effect of loading conditions on stress in the barefooted heel pad. *Medicine & Science in Sports & Exercise*, 37(6), 1030-1036.
- Stefanyshyn, D.J. & Nigg, B.M. (1998). Dynamic angular stiffness of the ankle joint during running and sprinting. *Journal of Applied Biomechanics*, 14, 292-299.
- Taddei, F., Pancanti, A., & Viceconti, M. (2004). An improved method for the automatic mapping of computed tomography numbers onto finite element models. *Medical Engineering & Physics*, 26, 61-69.
- Taylor, M., Tanner, K.E., & Freeman, M.A.R. (1998). Finite element analysis of the implanted proximal tibia: A relationship between the initial cancellous bone stresses and implant migration. *Journal of Biomechanics*, 31, 303-310.
- Teng, T.L., Chang, D.C., & Wu, C.H. (2007). Development and validation of side-impact crash and sled testing finite-element models. *Vehicle System Dynamics*, 45(10), 925-937.
- Teoh, S.H. & Chui, C.K. (2008). Bone material properties and fracture analysis: Needle insertion for spinal surgery. *Journal of the Mechanical Behaviour of Biomedical Materials*, 1, 115-139.
- Thomas, J.M. & Derrick, T.R. (2003). Effects of step uncertainty on impact peaks, shock attenuation, and knee/subtalar synchrony in treadmill running. *Journal of Applied Biomechanics*, 19, 60-70.
- Tortora, G.J. (2005). *Principles of human anatomy* (10<sup>th</sup> ed.). New York: John Wiley & Sons.
- Toyota Central R & D Labs, Inc. (n.d.). Total HUMAN Model for Safety Briefing Sheet – Pedestrian Model: Version 1.4 β-040526.
- Tsui, C.P., Tang, C.Y., Leung, C.P., Cheng, K.W., Ng, Y.F., Chow, D.H.K., et al. (2004). Active finite element analysis of skeletal muscle-tendon complex during isometric, shortening and lengthening contraction. *Bio-Medical Materials and Engineering*, 14, 271-279.
- Turchi, R., Altenhof, W., Kapoor, T., & Howard, A. (2004). An investigation into the head and neck injury potential of three-year-old children in forward and rearward facing child safety seats. *International Journal of Crashworthiness*, 9(4), 419-431.

- Van Eijden, T.M.G.J., Turkawski, S.J.J., Van Ruijven, L.J., & Brugman, P. (2002). Passive force characteristics of an architecturally complex muscle. *Journal of Biomechanics*, 35, 1183-1189.
- Verbitsky, O., Mizrahi, J., Voloshin, A., Treiger, J., & Isakov, E. (1998). Shock transmission and fatigue in human running. *Journal of Applied Biomechanics*, 14, 300-311.
- Voloshin, A.S., Mizrahi, J., Verbitsky, O., & Isakov, E. (1998). Dynamic loading on the human musculoskeletal system – effect of fatigue. *Clinical Biomechanics*, 13, 515-520.
- Voloshin, A. & Wosk, J. (1982). An in vivo study of low back pain and shock absorption in the human locomotor system. *Journal of Biomechanics*, 15(1), 21-27.
- Voloshin, A., Wosk, J., & Brull, M. (1981). Force wave transmission through the human locomotor system. *Journal of Biomechanical Engineering*, 103(1), 48-50.
- Voo, L., Kumaresan, S., Pintar, F.A., Yoganandan, N., & Sances Jr., A. (1996). Finite-element models of the human head. *Medical & Biological Engineering & Computing*, 34, 375-381.
- Wakeling, J.M., Liphardt, A.M., & Nigg, B.M. (2003). Muscle activity reduces soft-tissue resonance at heel-strike during walking. *Journal of Biomechanics*, 36, 1761-1769.
- Wakeling, J.M. & Nigg, B.M. (2001). Modification of soft tissue vibrations in the leg by muscular activity. *Journal of Applied Physiology*, 90, 412-420.
- Wakeling, J.M., Pascual, S.A., & Nigg, B.M. (2002). Altering muscle activity in the lower extremities by running with different shoes. *Medicine & Science in Sports & Exercise*, 34(9), 1529-1532.
- Wakeling, J.M., von Tscherner, V., Nigg, B.M., & Stergiou, P. (2001). Muscle activity in the leg is tuned in response to ground reaction forces. *Journal of Applied Physiology*, 91, 1307-1317.
- Wearing, S.C., Smeathers, J.E., Yates, B., Urry, S.R., & Dubois, P. (2009). Bulk compressive properties of the heel fat pad during walking: A pilot investigation in plantar heel pain. *Clinical Biomechanics*, 24, 397-402.
- Whiting, W.C. & Zernicke, R.F. (2008). *Biomechanics of musculoskeletal injury* (2<sup>nd</sup> ed.). Champaign, Illinois: Human Kinetics.
- Whittle, M.W. (1999). Generation and attenuation of transient impulsive forces beneath the foot: A review. *Gait and Posture*, 10, 264-275.
- Williams, D.S., McClay, I.S., & Hamill, J. (2001a). Arch structure and injury patterns in runners. *Clinical Biomechanics*, 16, 341-347.

- Williams, D.S., McClay, I.S., Hamill, J., & Buchanan, T.S. (2001b). Lower extremity kinematic and kinetic differences in runners with high and low arches. *Journal of Applied Biomechanics*, 17, 153-163.
- Williams, D.S., McClay Davis, I., Scholz, J.P., Hamill, J., & Buchanan, T.S. (2004). High-arched runners exhibit increased leg stiffness compared to low-arched runners. *Gait and Posture*, 19, 263-269.
- Winter, D.A. (2005). *Biomechanics and motor control of human movement* (3<sup>rd</sup> ed.). Hoboken, New Jersey: John Wiley & Sons, Inc.
- Wosk, J. & Voloshin, A. (1981). Wave attenuation in skeletons of young healthy persons. *Journal of Biomechanics*, 14(4), 261-267.
- Wright, I.C., Neptune, R.R., van den Bogert, A.J., & Nigg, B.M. (1998). Passive regulation of impact forces in heel-toe running. *Clinical Biomechanics*, 13, 521-531.
- Yamada, H. (1970). *Strength of biological materials*. Baltimore: Williams & Wilkins.
- Yasuki, T. (2007). Mechanism analysis of pedestrian knee-bending angle by SUV type vehicles using human FE model. *International Journal of Crashworthiness*, 12(6), 645-651.
- Yosibash, Z., Padan, R., Joskowicz, L., & Milgrom, C. (2007). A CT-based high-order finite element analysis of the human proximal femur compared to in-vitro experiments. *Journal of Biomechanical Engineering*, 129, 297-309.
- Zachariah, S.G. & Sanders, J.E. (2000). Finite element estimates of interface stress in the trans-tibial prosthesis using gap elements are different from those using automated contact. *Journal of Biomechanics*, 33, 895-899.
- Zhang, M., Mak, A.F.T., & Roberts, V.C. (1998). Finite element modelling of a residual lower-limb in a prosthetic socket: A survey of the development in the first decade. *Medical Engineering & Physics*, 20, 360-373.

*Vita Auctoris*

NAME: Alison Nicole Schinkel-Ivy

PLACE OF BIRTH Oakville, Ontario

YEAR OF BIRTH 1986

EDUCATION Iroquois Ridge High School, Oakville, Ontario  
2000 – 2004

University of Windsor, Windsor, Ontario  
2004 – 2008 B.H.K.

University of Windsor, Windsor, Ontario  
2008 – 2010 M.H.K.